Cell

Sustained deep-tissue voltage recording using a fast indicator evolved for two-photon microscopy

Graphical abstract

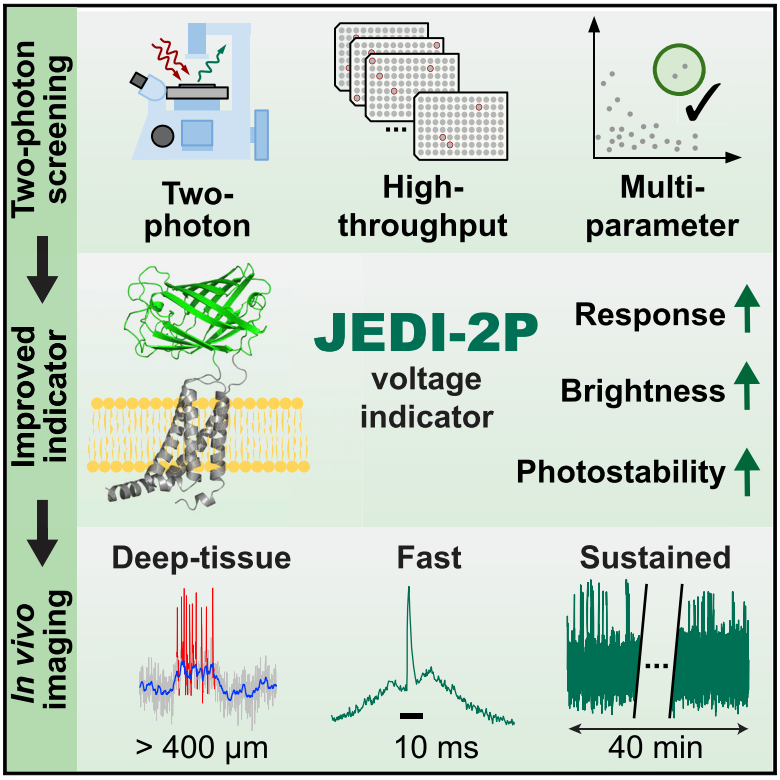

Highlights

- JEDI-2P is a faster, brighter, more sensitive, and photostable voltage indicator
- JEDI-2P was engineered using a two-photon multiparameter screening platform
- JEDI-2P enabled two-photon voltage recordings in retinal explants, flies, and mice
- JEDI-2P produced deep (cortical layer 5) and long (>40 min) recordings in mice

Authors

Zhuohe Liu, Xiaoyu Lu, Vincent Villette, ..., Jacob Reimer, Stéphane Dieudonné, François St-Pierre

Correspondence

stpierre@bcm.edu

In brief

Engineering of a fast, sensitive, bright and photostable genetically encoded voltage indicator optimized for two-photon microscopy enables deep-tissue optical recording of rapid voltage dynamics over tens of minutes.

Liu et al., 2022, Cell *185*, 3408–3425
September 1, 2022
https://doi.org/10.1016/j.cell.2022.07.013

CellPress

CellPress
OPEN ACCESS

Cell

Resource

Sustained deep-tissue voltage recording using a fast indicator evolved for two-photon microscopy

Zhuohe Liu,[1,15] Xiaoyu Lu,[2,15] Vincent Villette,[3,15] Yueyang Gou,[4,15] Kevin L. Colbert,[4,16] Shujuan Lai,[4] Sihui Guan,[4,17] Michelle A. Land,[4] Jihwan Lee,[2,4] Tensae Assefa,[5,18] Daniel R. Zollinger,[4,19] Maria M. Korympidou,[6,7,8] Anna L. Vlasits,[6,7,20] Michelle M. Pang,[9] Sharon Su,[9,21] Changjia Cai,[10] Emmanouil Froudarakis,[4,11] Na Zhou,[4] Saumil S. Patel,[4] Cameron L. Smith,[4,13] Annick Ayon,[3] Pierre Bizouard,[3] Jonathan Bradley,[3] Katrin Franke,[6,7,8] Thomas R. Clandinin,[9] Andrea Giovannucci,[10,12] Andreas S. Tolias,[1,4,13] Jacob Reimer,[4,13] Stéphane Dieudonné,[3] and François St-Pierre[1,2,4,14,22,*]

[1]Department of Electrical and Computer Engineering, Rice University, Houston, TX 77005, USA
[2]Systems, Synthetic, and Physical Biology Program, Rice University, Houston, TX 77005, USA
[3]Institut de Biologie de l'École Normale Supérieure (IBENS), École Normale Supérieure, CNRS, INSERM, PSL Research University, Paris 75005, France
[4]Department of Neuroscience, Baylor College of Medicine, Houston, TX 77030, USA
[5]Department of Bioengineering, Rice University, Houston, TX 77005, USA
[6]Institute for Ophthalmic Research, University of Tübingen, Tübingen, Baden-Württemberg 72076, Germany
[7]Center for Integrative Neuroscience, University of Tübingen, Tübingen, Baden-Württemberg 72076, Germany
[8]Bernstein Center for Computational Neuroscience, University of Tübingen, Tübingen, Baden-Württemberg, 72076, Germany
[9]Department of Neurobiology, Stanford University, Stanford, CA 94305, USA
[10]Joint Department of Biomedical Engineering, University of North Carolina at Chapel Hill and North Carolina State University, Chapel Hill, NC 27599, USA
[11]Institute of Molecular Biology and Biotechnology, Foundation for Research and Technology Hellas, Heraklion 70013, Greece
[12]UNC Neuroscience Center, Chapel Hill, NC 27599, USA
[13]Center for Neuroscience and Artificial Intelligence, Baylor College of Medicine, Houston, TX 77030, USA
[14]Department of Biochemistry and Molecular Biology, Baylor College of Medicine, Houston, TX 77030, USA
[15]These authors contributed equally
[16]Present address: Texas A&M School of Engineering Medicine, Houston, TX 77840, USA
[17]Present address: Overland Pharmaceuticals Inc., Shanghai 200070, China
[18]Present address: NYU Grossman School of Medicine, New York, NY 10010, USA
[19]Present address: Foundation Medicine Incorporated, San Diego, CA 92121-1103, USA
[20]Present address: Department of Neurobiology, Northwestern University, Evanston, IL 60208, USA
[21]Present address: Department of Neuroscience, Columbia University, New York, NY 10027, USA
[22]Lead contact
*Correspondence: stpierre@bcm.edu
https://doi.org/10.1016/j.cell.2022.07.013

SUMMARY

Genetically encoded voltage indicators are emerging tools for monitoring voltage dynamics with cell-type specificity. However, current indicators enable a narrow range of applications due to poor performance under two-photon microscopy, a method of choice for deep-tissue recording. To improve indicators, we developed a multi-parameter high-throughput platform to optimize voltage indicators for two-photon microscopy. Using this system, we identified JEDI-2P, an indicator that is faster, brighter, and more sensitive and photostable than its predecessors. We demonstrate that JEDI-2P can report light-evoked responses in axonal termini of *Drosophila* interneurons and the dendrites and somata of amacrine cells of isolated mouse retina. JEDI-2P can also optically record the voltage dynamics of individual cortical neurons in awake behaving mice for more than 30 min using both resonant-scanning and ULoVE random-access microscopy. Finally, ULoVE recording of JEDI-2P can robustly detect spikes at depths exceeding 400 μm and report voltage correlations in pairs of neurons.

INTRODUCTION

Genetically encoded voltage indicators (GEVIs)—protein-based biosensors whose brightness is modulated by voltage—are promising tools for reporting neuronal voltage dynamics with subcellular resolution, millisecond-timescale dynamics, and cell-type specificity (Yang and St-Pierre, 2016). Particularly coveted for *in vivo* applications are GEVIs that can be

CellPress
OPEN ACCESS

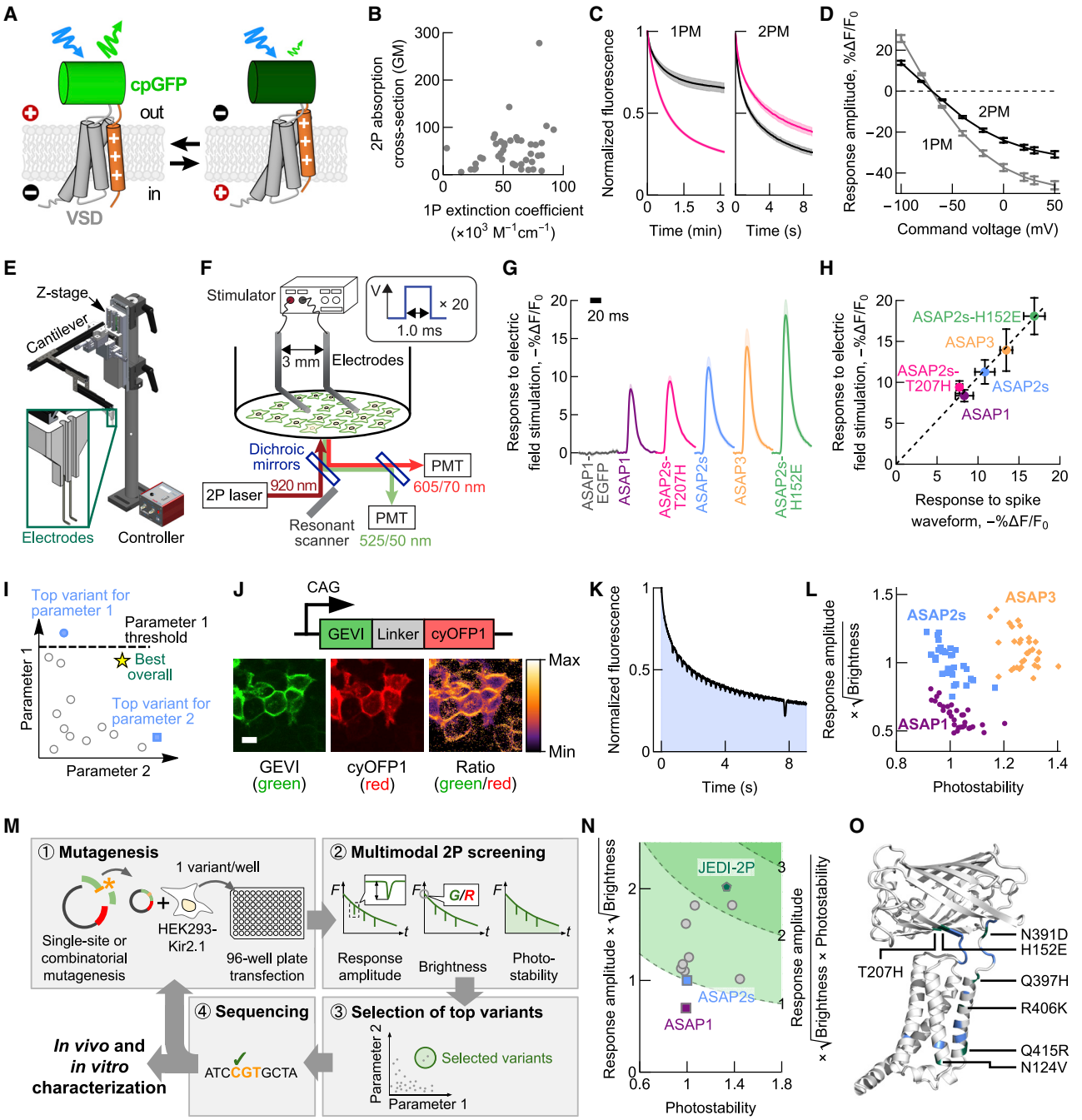

Figure 1. Significance, design, and deployment of a multiparametric two-photon voltage indicator screening platform

(A) We optimized indicators in which a circularly permuted green fluorescent protein (cpGFP, green) is inserted into a voltage-sensing domain (VSD, gray/red). Depolarization (*right*) results in conformational changes that reduce cpGFP brightness.

(B–D) 1PM properties of fluorescent proteins and sensors do not always predict their performance under 2PM. (B) Fluorescent protein absorption under 1PM and 2PM are poorly correlated. Pearson's r = 0.28. Data are from Drobizhev et al. (2011). (C) Relative mean photobleaching rates under widefield 1PM (*left*) are not always predictive of those under laser-scanning 2PM (*right*). Gray, ASAP1-N124V-R406K. Pink, ASAP2s-T207H. Shaded areas denote the 95% CI. n = 6/condition. (D) ASAP3 produces different mean response amplitudes to 1-s voltage steps under our 1PM and 2PM imaging conditions. Error bars, 95% CI. n = 9 (1PM) or 7 (2PM) HEK293A cells. $p < 0.0001$ for all comparisons (t test with Holm-Šídák correction).

(E) Rendering of the motorized electrode assembly.

(F) Schematic of the automated 2PM GEVI screening system. The boxed area shows the stimulation protocol.

(G) Mean responses to 1-ms electric field stimulations. The response of each GEVI was measured in a separate experiment. ASAP1-EGFP is a control with no sensitivity to voltage. Shaded areas denote the 95% CI. n = 6/GEVI.

(legend continued on next page)

visualized with two-photon microscopy (2PM), a method of choice for noninvasive deep-tissue recording. Because opsin-based GEVIs have poor responses under 2PM, indicators built by coupling fluorescent proteins to domains from voltage-sensitive phosphatases are preferred for two-photon voltage recording (Brinks et al., 2015; Chamberland et al., 2017). For example, indicators of the accelerated sensors of action potentials (ASAP) family have been deployed for reporting voltage in flies, fish, and mice under 2PM (St-Pierre et al., 2014; Yang et al., 2016; Villette et al., 2019; Wu et al., 2020; Yoshimatsu et al., 2021).

Many experimental paradigms—such as monitoring changes in synaptic plasticity or behavioral representations during learning—require neural recordings of 30 min or longer (Huber et al., 2012). However, the poor photostability and low response amplitude of current ASAP indicators limit spike detection over extended durations. For example, voltage recording in the mouse cortex with the indicator ASAP3 was limited to 80 s and ~1–5 min using the kilohertz-rate 2PM optical methods free-space angular-chirp-enhanced delay (FACED) and ultrafast local volume excitation (ULoVE), respectively (Wu et al., 2020; Villette et al., 2019). With both techniques, response amplitudes to spikes from cortical neurons were modest (mean of ~9%–10%), and spikes could not be robustly detected in deeper cortical areas including layer 5. Therefore, improved indicators are needed for deeper and longer recording of voltage dynamics *in vivo*.

We sought to develop a 2PM-optimized GEVI that would address the shortcomings of existing indicators. We first developed an automated high-throughput screening platform to directly screen indicators under 2PM. Critically, this system can simultaneously screen multiple key performance metrics—response amplitude to short voltage pulses, brightness, and photostability. Using this platform, we identified JEDI-2P, a variant that is improved across all metrics compared with its predecessors. We demonstrate the utility of this 2P-optimized sensor for extended voltage recordings across multiple preparations, animal models, cell types, subcellular locations, and optical recording techniques. Finally, we show that JEDI-2P enables single-cell recording of voltage dynamics in cortical layer 5 and high-fidelity measurements of pairwise voltage correlations in layer 2/3 of awake behaving rodents.

RESULTS

GEVIs can perform differently under one- and two-photon excitation

We sought to develop indicators optimized for voltage recording under 2PM. We selected to improve ASAP-family GEVIs (Figure 1A) because they produce the largest responses to spikes under 2PM (Chamberland et al., 2017; Villette et al., 2019; Yang and St-Pierre, 2016; St-Pierre et al., 2015). Current screening platforms evaluate GEVIs under one-photon microscopy (1PM), and only the best-performing variants are fully characterized under 2PM (Abdelfattah et al., 2016; Piatkevich et al., 2018; Villette et al., 2019; Platisa et al., 2017). However, fluorescent protein (FP) excitation under 1P and 2P illuminations is governed by different photophysical mechanisms, with 2P absorption being more sensitive to variations in the local electric field around the chromophore (Drobizhev et al., 2011). FP absorption under 1P and 2P excitation are thus poorly correlated (Figure 1B; Data S1) (Adhikari et al., 2021). 2PM is usually conducted by point-by-point scanning with a high-power laser. Since the relationship between photobleaching rate and illumination power can vary between fluorescent proteins (Cranfill et al., 2016), we hypothesized that improved photostability under 1PM widefield illumination would not always predict greater photostability when imaging with a high-power 2P scanning laser. Supporting this hypothesis, we found GEVI variants in our libraries with higher photostability under widefield 1PM but faster photobleaching rates under laser-scanning 2PM (Figure 1C). Changes in the membrane potential are thought to perturb the chemical environment of the FP chromophore in ASAP indicators. We surmised that these modulations could produce brightness changes of different amplitudes under 2PM compared with 1PM. Consistent with our prediction, we observed that the responses of the indicator ASAP3 to 1-s voltage steps were dramatically lower under 2PM compared with 1PM using our standard illumination conditions (Figure 1D and Table S1). Taken together, these observations motivated us to develop and apply a platform to screen GEVIs directly under laser-scanning 2PM.

Screening for rapid GEVIs using 1-ms electric field stimulations

Because of the millisecond timescale of important neuronal signals such as spikes and postsynaptic potentials, we sought to

(H) GEVI responses to 1-ms field stimulation pulses are highly correlated with their responses to neuronal-like spike waveforms at room temperature (100-mV height, 2-ms width). Pearson's $r^2 = 0.998$. Dashed line is the intercept-free linear fit. Error bars are the 95% CI. n = 6/independent transfections per GEVI (electric field stimulation) or 4–7 HEK293A cells (spike waveforms).

(I) Schematic showing that single-parameter or hierarchical screening of GEVIs can miss variants with overall better performance across multiple metrics (yellow star) and variants that did not meet the threshold for the first parameter but display high performance in other properties (blue square).

(J) GEVIs were fused to a red-emitting reference FP (cyOFP1) to measure brightness independently of variations in expression level. *Top*, screening cassette schematic. *Bottom*, similar green/red ratios were observed for cells with different expression levels. Scale bar, 10 μm.

(K) Photostability was quantified as the area under the curve (blue), as shown in this representative screening time course.

(L) Three GEVIs form distinct clusters. Data were normalized to the mean values of ASAP2s. n = 32/GEVI.

(M) GEVI screening workflow.

(N) Multiparametric evaluation of new GEVIs. Gray circles are screening intermediates. Data were normalized to the mean values of ASAP2s. n = 6/GEVI.

(O) *In silico* model of ASAP2s showing the locations of the 6 mutations in JEDI-2P compared with ASAP2s (green). 16 other residues were also screened (blue). In all panels, unless otherwise noted, the sample size (n) represents independent transfections and shaded areas and error bars denote the 95% CI.

See also Figures S1, S2, and S3 and Table S1.

develop a platform to screen indicators that produce larger responses to rapid voltage transients. We custom-designed motorized platinum electrodes that could be automatically positioned in wells of standard 96-well plates and deliver electric field stimulation (EFS) pulses (Figures 1E, 1F, and S1A–S1D). We conducted EFS in HEK293 cells with a resting membrane potential of ~ -77 mV, similar to that of cortical neurons, due to the stable expression of the inward-rectifying channel Kir2.1 (Chamberland et al., 2017; Zhang et al., 2009). EFS of these cells results in a net depolarization (Tsutsui et al., 2014), presumably because Kir2.1 produces an inward current across the hyperpolarized side of the cell that exceeds its outward current across the depolarized side.

We stimulated cells with 1-ms EFS pulses—two orders of magnitude faster than previous efforts with HEK293-Kir2.1 cells (Tsutsui et al., 2014)—to screen for GEVIs with fast kinetics. During the stimulation, GEVIs were imaged at a frame rate of 0.44 kHz using a 2P inverted microscope equipped with a resonant scanner (Figure 1F, *bottom*). We observed that 1-ms EFS pulses induced robust and reproducible GEVI responses (Figure S1E). The fast indicator ASAP1, which has ~2-ms depolarization and repolarization kinetics at room temperature (St-Pierre et al., 2014), produced EFS-induced fluorescence responses with a width of ~13 ms (Figure S1F). The duration of EFS-induced fluorescence transients thus likely reflects both indicator kinetics and the timescale of Kir2.1-driven repolarization. We validated the utility of this assay by demonstrating that a GEVI's response amplitude to 1-ms EFS pulses is highly predictive of its peak response amplitude to simulated action potentials (APs) (Figures 1G and 1H).

Enabling multiparametric two-photon GEVI screening

We surmised that a holistic evaluation of all performance metrics would be optimal for identifying promising variants. For example, a variant may be the "overall best" even if it is not the top performer in any performance metric. Moreover, a mutation that produces a considerable improvement in one metric, but impairments in others, may still be valuable in combination with compensatory mutations of other residues. However, such variants would often be discarded in screens that look for only one performance metric or in hierarchical screening in which a candidate's performance on the first metric determines whether it will be chosen for further evaluation based on a second metric (Figure 1I). Therefore, a final design criterion for our platform was the ability to screen for responsivity, speed, brightness, and photostability in the same experiment.

To quantify the brightness of GEVIs independently of their expression level, we fused GEVIs to the orange-red FP cyOFP1 (Chu et al., 2016) and measured the green-to-red fluorescence ratio (Figure 1J). We chose cyOFP1 because of its significant Stokes shift, enabling GEVIs and cyOFP1 to be excited at the same wavelength (920 nm). To enable rapid quantification of photostability, we set the laser power to produce substantial photobleaching during the short duration of the EFS assay (Figure 1K). We defined photostability as the cumulative GEVI fluorescence normalized by the initial fluorescence. We developed compound metrics to simplify the ranking of indicators while considering multiple performance criteria (method details) and confirmed that three published ASAP variants could be distinguished by considering several metrics (Figure 1L).

Multiparametric 2P screening identifies JEDI-2P, a GEVI that is fast, sensitive, bright, and photostable

We deployed our 2P screening platform for high-throughput GEVI optimization (Figure 1M). Specifically, 2PM videos were taken while the cells were subjected to EFS, and the data were analyzed by a custom pipeline (Figures S1G–S1I). We used ASAP1 and ASAP2s as starting templates (Chamberland et al., 2017; St-Pierre et al., 2014) since we started this project before ASAP3 was reported. We generated libraries where single residues were randomized between all 20 amino acids. Each variant was transfected in a separate well of a 96-well plate. We sequenced variants that performed well based on compound or individual metrics.

We screened 21 positions in ASAP1 and ASAP2s in saturation mutagenesis libraries, including 13 in the voltage-sensing domain and 8 in the GFP (Figure S2A). Ten of the screened residues were within three amino acids of the two voltage-sensing domain (VSD)-cpGFP junctions (Figure S2B), since mutating residues near the FP insertion point can increase indicator response amplitude (Nasu et al., 2021). Eight of the targeted VSD residues were prioritized based on their high evolutionary conservation (Palovcak et al., 2014) (Figure S2C). Several conserved residues were also chosen because they correspond to charged amino acids that drive or facilitate the response to changes in the electric field (Bezanilla, 2008). Of the three targeted residues remaining, two interact with the chromophore (T207 and H152), and one (Q397) modulates the $V_{1/2}$ of the response-voltage relationship of an orthologous GEVI (Dimitrov et al., 2007). We identified many mutations that increased one or multiple performance metrics (Figures 1N, S2D, and S2E). We then created and screened libraries that combined these advantageous mutations to find additive and synergistic interactions. Our best candidate differs from ASAP2s in 7 positions (Figures 1O, S2D, and S3). We call this new sensor jellyfish-derived electricity-reporting designer indicator for 2-photon, or JEDI-2P.

JEDI-2P is brighter, faster, and more photostable and responsive than existing GEVIs under two-photon illumination *in vitro*

We quantified JEDI-2P's response amplitude *in vitro* using combined imaging and whole-cell voltage clamp in individual human cells (HEK293A). Experiments described in the remainder of the article were conducted under 2PM, unless otherwise noted, and GEVIs without a covalently attached cyOFP1 were used. Detailed information on the optical recording conditions for the main figures of this paper can be found in Table S1. Following a common procedure in voltage imaging, fluorescence changes are plotted in the same orientation as electrical changes unless otherwise noted. Because JEDI-2P is a bright-to-dim indicator (Figure 1A), optical responses to voltage are reported as negative changes in fluorescence ($-\%\Delta F/F_0$, with F_0 representing the baseline fluorescence).

JEDI-2P's fluorescence-versus-voltage curve was sigmoidal (Figures 2A and 2B), consistent with the properties of voltage-sensitive domains (Murata et al., 2005) and homologous GEVIs

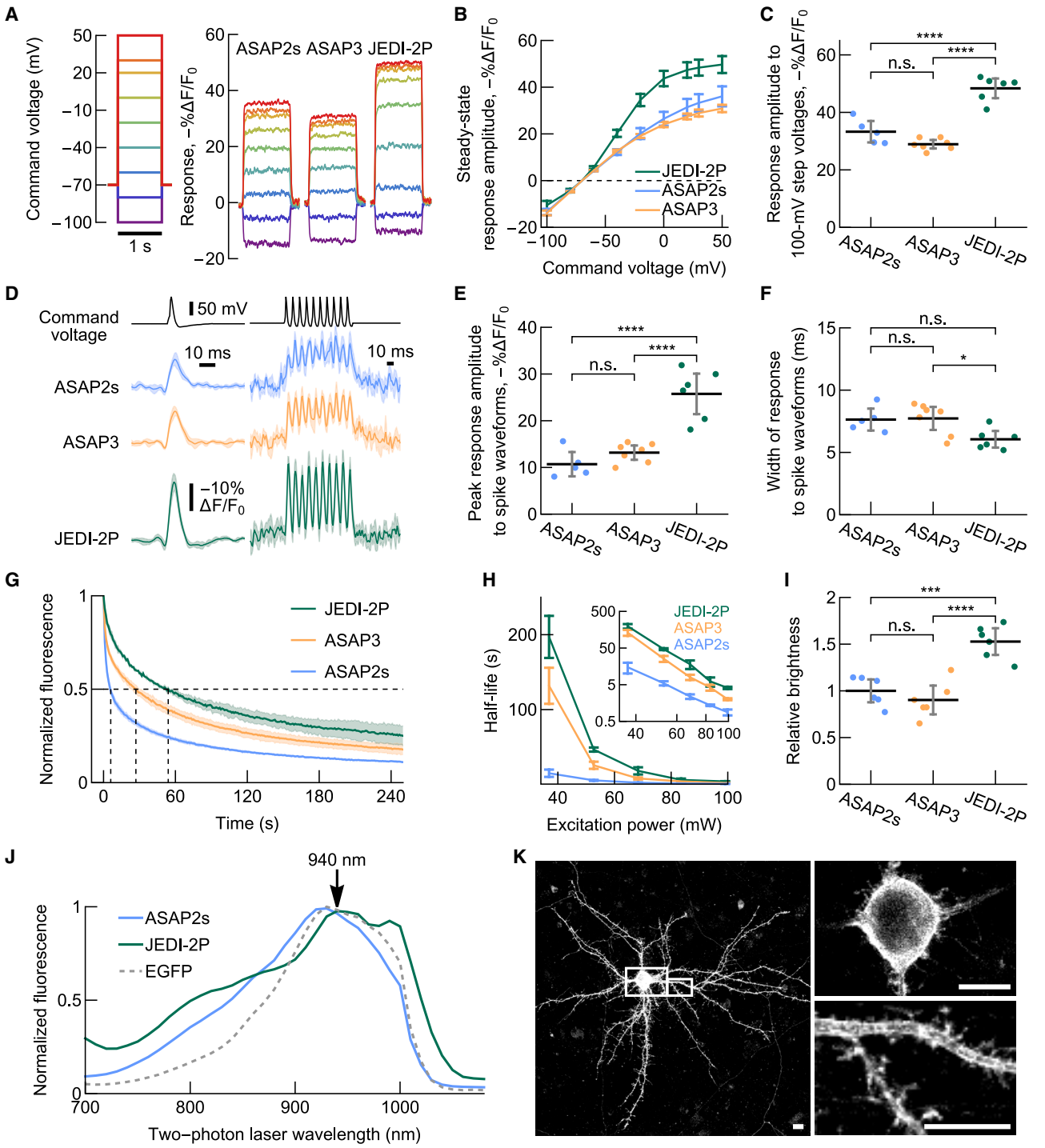

Figure 2. JEDI-2P displays improved sensitivity, off-kinetics, brightness, and photostability under 2PM *in vitro*

(A–C) JEDI-2P produces larger steady-state responses to step depolarizations under 2PM than ASAP3 and ASAP2s. Voltage was modulated by whole-cell voltage clamp. n = 5 (ASAP2s), 7 (ASAP3), and 6 (JEDI-2P) HEK293A cells. (A) Mean fluorescence responses to voltage steps. Traces were smoothed by a 24-ms moving average. (B) Quantification of (A). For statistics, see Data S2. (C) JEDI-2P produces larger peak steady-state responses to 100-mV voltage steps from a resting potential of −70 mV. $p < 0.0001$ (ANOVA).

(D–F) JEDI-2P produces larger and faster responses to a spike waveform under 2PM than ASAP3 and ASAP2s. n = 5 (ASAP2s) and 7 (ASAP3 & JEDI-2P) HEK293A cells. To mimic the properties of layer 2/3 cortical neurons at room temperature, the waveform had a 2-ms full width at half maximum (Hedrick and Waters, 2012). (D) Mean responses to a single spike waveform (*left*) and a 100-Hz spike train (*right*). (E and F) Quantification of the peak response amplitude (E) and full width at half maximum (F) of the GEVI responses to single spike waveforms. Black lines indicate means. ANOVA $p < 0.0001$ (E) and $p < 0.01$ (F).

(legend continued on next page)

(Villette et al., 2019). JEDI-2P produced larger steady-state responses to 1-s depolarization voltage steps than ASAP2s and ASAP3 (Figure 2C; Data S2). JEDI-2P's response amplitude per unit voltage was largest between approximately −80 and 0 mV.

JEDI-2P showed faster depolarization and repolarization kinetics than ASAP2s and ASAP3 under 1PM (Table S2). We could not quantify kinetics under 2PM because optical traces acquired under 15.9-kHz 2P single-line scanning were too noisy to determine kinetics with sub-millisecond resolution (method details). At ∼33°C, JEDI-2P's depolarization kinetics were best described by a bi-exponential curve dominated (89%) by a fast component with a time constant ($\tau = 0.54$ ms) that is well matched to the ∼0.8-ms AP width of regular-spiking cortical neurons (Kawaguchi, 1995; McCormick et al., 1985). JEDI-2P's repolarization kinetics at ∼33°C were well fit with a mono-exponential decay curve with a time constant of 1.2 ms, more than three times faster than ASAP3. Rapid repolarization kinetics are essential, given that inter-spike intervals can be as short as 2–6 ms in fast-spiking cells (Wang et al., 2016) and during bursting (Harris et al., 2001). Kinetics were faster at higher temperatures, as previously reported with ASAP indicators and GEVIs based on orthologous voltage-sensing domains (Lundby et al., 2010; Villette et al., 2019).

JEDI-2P produced more than two-fold larger responses to AP waveforms than ASAP2s and ASAP3 (Figures 2D and 2E), as expected, given JEDI-2P's faster depolarization kinetics and larger maximal response amplitude to step voltages. The faster kinetics of JEDI-2P more accurately tracked individual spikes within trains of AP waveforms (Figure 2D, *right*) and produced narrower optical responses than ASAP3 (Figure 2F). Brightness and photostability were evaluated in HEK293-Kir2.1 cells because they maintain a resting membrane potential of ∼ −77 mV, similar to cortical neurons (Zhang et al., 2009). JEDI-2P displayed higher photostability and brightness than ASAP2s and ASAP3 (Figures 2G–2I).

Given our previous observations that indicators' performance can depend on illumination conditions (Figures 1C and 1D), we repeated our analyses under widefield 1PM (Figure S4). JEDI-2P responses under 1PM were similar to those under 2PM (Figures S4A–S4F). However, ASAP3's response amplitudes were strikingly larger (∼2-fold) under 1PM than 2PM, reaching similar values to those reported in its original characterization under 1PM (Villette et al., 2019; Kim et al., 2022). Although JEDI-2P was slightly more photostable than ASAP3 under 2PM, it was slightly more photolabile under 1PM (Figures S4G and S4H). However, the higher brightness of JEDI-2P compared with ASAP3 and ASAP2s was maintained under 1PM (Figure S4I). Taken together, these results strengthen our contention that indicators should be optimized for the illumination conditions of prime interest.

JEDI-2P's 2PM excitation spectrum peaked at 940 nm, a ∼10-nm redshift compared with ASAP2s (Figure 2J). Redshifts in JEDI-2Ps excitation and emission spectra were also observed under 1PM (Figures S4J and S4K). These spectral changes are likely caused by the T207H (GFP T203H) mutation, which has redshifted the excitation and emission spectra of photoactivated PA-GFP compared with wild-type GFP (Patterson and Lippincott-Schwartz, 2002). The redshifted spectra of JEDI-2P should enable voltage recording with powerful Ytterbium-doped lasers at 1,030–1,040 nm, albeit at about ∼20%–35% of the excitation efficiency obtained when using 940 nm light. Overall, the broad peak of JEDI-2P means that it can be excited with a wide range of wavelengths, with illumination between 920 and 1,000 nm, producing >85% of the peak fluorescence. Finally, we sought to determine whether JEDI-2P could be efficiently expressed in neurons. We transfected JEDI-2P in dissociated mouse cortical neurons and observed high fluorescence at the presumed plasma membrane in the soma and dendrites (Figure 2K).

The excellent performance of JEDI-2P *in vitro* motivated us to evaluate its utility in slices and *in vivo* across several preparations that differ based on cell type, model system, and optical technique. These applications of JEDI-2P, described in the following sections, were conducted with slightly off-peak excitation light (920–927 nm) because they started before the 2PM excitation spectrum was determined.

JEDI-2P reports dendritic responses to fluctuating visual stimuli in isolated mouse retina

In the mammalian retina, dendrites of inhibitory cells are thought to perform critical computations that shape visual signals before they are sent to the brain (Diamond, 2017). For example, studies on distinct amacrine cell types suggest that they provide dendro-dendritic inhibition to their postsynaptic partners, with individual dendrites or sections of dendrites performing isolated computations (Grimes et al., 2010; Hausselt et al., 2007; Tukker et al., 2004; Vlasits et al., 2016). However, because it is challenging to access dendrites by electrophysiological methods, dendritic voltage transformations are poorly understood. Tools that can easily and noninvasively report dendritic voltage are thus

(G–I) JEDI-2P is more photostable and brighter than ASAP3 and ASAP2s under 2PM. Assays were conducted at a polarized potential (∼ −77 mV) by expressing GEVIs in HEK293-Kir2.1 cells. (G) Normalized mean fluorescence as a function of time. Dashed lines highlight mark half-lives. n = 3 independent transfections per GEVI. (H) Relation of photobleaching half-life versus excitation power both shown in a linear scale or logarithmic scale (inset). n = 3 independent transfections per condition. For statistics, see Data S2. (I) Brightness JEDI-2P is brighter than ASAP3 and ASAP2s under 2P at 920 nm. Black bars denote the means of n = 6 independent transfections per GEVI. $p < 0.0001$ ANOVA.

(J) 2PM excitation spectra in HEK293-Kir2.1 cells. JEDI-2P has a red-shifted peak (940 nm) compared with ASAP2s (930 nm) and EGFP (930 nm) spectra were normalized to their respective peaks. Laser pulses were not pre-compensated for dispersion in the microscope optical path. Lines show the mean of n = 18 (ASAP2s), 13 (EGFP), and 38 (JEDI-2P) fields of view, each with >100 cells.

(K) JEDI-2P targets efficiently to the plasma membrane in the soma and dendrites, as shown in this confocal image of a representative DIV13 cortical neuron dissociated from an E18 rat brain and imaged by confocal microscopy. The overall image and dendrite zoom-in are from the maximal projection of the z stack, whereas the soma image is a single slice. Scale bars, 10 μm. All panels: **** $p < 0.0001$; *** $p < 0.001$; ** $p < 0.01$; * $p < 0.05$; n.s. $p > 0.05$, Tukey's HSD multiple comparison test. Error bars or shaded areas denote the 95% CI. All tests were conducted at room temperature. For statistics for (B) and (H), see Data S2. For (C), (E), (F), and (I), black lines indicate means.

See also Figure S4; Table S1, Table S2, and Data S2.

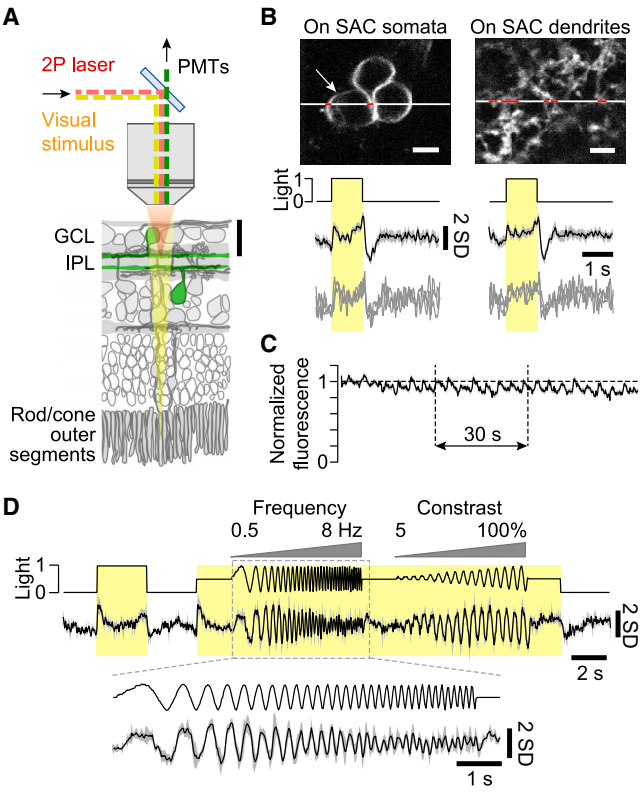

Figure 3. JEDI-2P captures voltage responses to changes in visual stimuli frequency and contrast in isolated mouse retina

(A) Experimental setup schematic. JEDI-2P was expressed in starburst amacrine cells (SAC, green). GCL, ganglion cell layer and IPL, inner plexiform layer. Visual stimuli were presented to the photoreceptors in the retina. Scale bar, 20 μm.

(B) *Top*, representative images of "on" SACs expressing JEDI-2P. Scale bars, 5 μm. The optical traces are the mean voltage responses to n = 20 trials (black line) and 3 representative single trials (gray, *bottom* traces) recorded from somata (*left*) and dendrites (*right*). Shaded areas are the 95% CI. Fluorescence was recorded at 1 kHz with line scans (white lines) and resampled at 40 Hz. The pixels used for analysis are shown in red. The white arrow indicates the cell analyzed in somatic recordings. s.d. is the standard deviation of the baseline variation across all trials.

(C) JEDI-2P reports membrane voltage with high photostability. Laser power, 9–12 mW (measured after the objective). The black line denotes the mean fluorescence normalized using the mean fluorescence of the first 2 s of each recording. Shaded areas are the 95% CI and may be too small to see. n = 4 independent fields of view from 2 mice.

(D) JEDI-2P captures dendritic voltage responses to visual stimuli frequency and contrast. The optical trace is the mean dendritic voltage response, and shaded areas are the 95% CI. Fluorescence was recorded at up to 1 kHz and resampled to 40 Hz. A stimulus frequency of 2 Hz was used when changing contrast. *Bottom*, zoomed-in sections of the stimulus and responses. 2 SD is equivalent to 34% $\Delta F/F_0$. n = 3 independent fields of view from 2 mice. For all panels except for (C), fluorescence traces were baseline corrected.

See also Table S1.

urgently needed for understanding visual information processing in the retina.

Given its high performance *in vitro*, we hypothesized that JEDI-2P could report voltage signals in the dendrites of retinal neurons. We chose to express JEDI-2P in starburst amacrine cells (SAC), non-spiking inhibitory interneurons that play an essential role in transforming visual signals (Mauss et al., 2017). SAC dendrites act as both input and output structures: they receive graded excitatory input from bipolar cells and deliver inhibitory signals to ganglion cells (Wei, 2018). SAC dendrites are thus excellent sites to evaluate the ability of JEDI-2P to report subcellular voltage dynamics. We imaged JEDI-2P fluorescence while presenting visual stimuli onto photoreceptors of isolated mouse retinas through the same objective (Figure 3A). 2P imaging was necessary to minimize activation of photoreceptors: the infrared wavelengths used for 2P excitation are nearly invisible to mouse photoreceptors, enabling the monitoring of light-evoked neural responses (Euler et al., 2019). Activation of photoreceptors by photons emitted from indicators is low compared with their responses to light stimuli (Euler et al., 2009; Euler et al., 2019).

Intravitreal injection of adeno-associated viruses (AAVs) encoding JEDI-2P produced robust expression in SAC somata and dendrites (Figure 3B). We imaged "on" SACs—which depolarize as light intensity increases—and observed strong voltage responses to 1-s light flashes from their somas in the ganglion cell layer and their dendrites in the inner plexiform layer (Figure 3B). Although our scanning method only imaged a small number of membrane pixels (somata: 15 pixels, dendrites: 38 pixels), the signal-to-noise ratio was sufficiently high to observe light responses in single trials (Figure 3B, *bottom*). We observed minimal indicator photobleaching over the 1.5 min duration of each experiment, with indicators retaining 91.8% ± 2.7% (mean ± 95% CI) of their original fluorescence (Figure 3C). The response time course matched previous electrophysiological observations at the soma, including the peak depolarization followed by a plateau after light onset, and the transient hyperpolarization, followed by the rebound depolarization after light offset (Ankri et al., 2020; Peters and Masland, 1996; Vlasits et al., 2014).

Finally, we evaluated the ability of JEDI-2P to report neuronal frequency and contrast preference, as these can be used to characterize visual stimuli processing (Derrington and Lennie, 1982; Enroth-Cugell and Robson, 1966) and to functionally classify cell types (Baden et al., 2016; Franke et al., 2017). We imaged SAC dendrites expressing JEDI-2P while presenting a complex visual stimulus we reported previously (Baden et al., 2016) (Figure 3D). JEDI-2P tracked all frequencies (0.5–8 Hz) and contrast changes as low as 11%. The reduced amplitudes in response to higher frequencies can also be observed at the level of presynaptic glutamate release (Franke et al., 2017), suggesting that they represent the underlying response and are not an artifact produced by the indicator. Taken together, our results in isolated mice retina demonstrate that JEDI-2P can be deployed to report stimuli-driven responses in intact neuronal tissue with subcellular resolution and excellent photostability under 2PM.

JEDI-2P reports rapid voltage transients in *Drosophila* axon terminals with improved response amplitude and excellent photostability

Next, we sought to deploy JEDI-2P to report voltage transients *in vivo* and over extended durations. We first evaluated JEDI-2P's ability to monitor the light-evoked responses of the *Drosophila* L2 lamina neurons—non-spiking visual interneurons postsynaptic to the photoreceptors R1–R6 (Figure 4A)—given

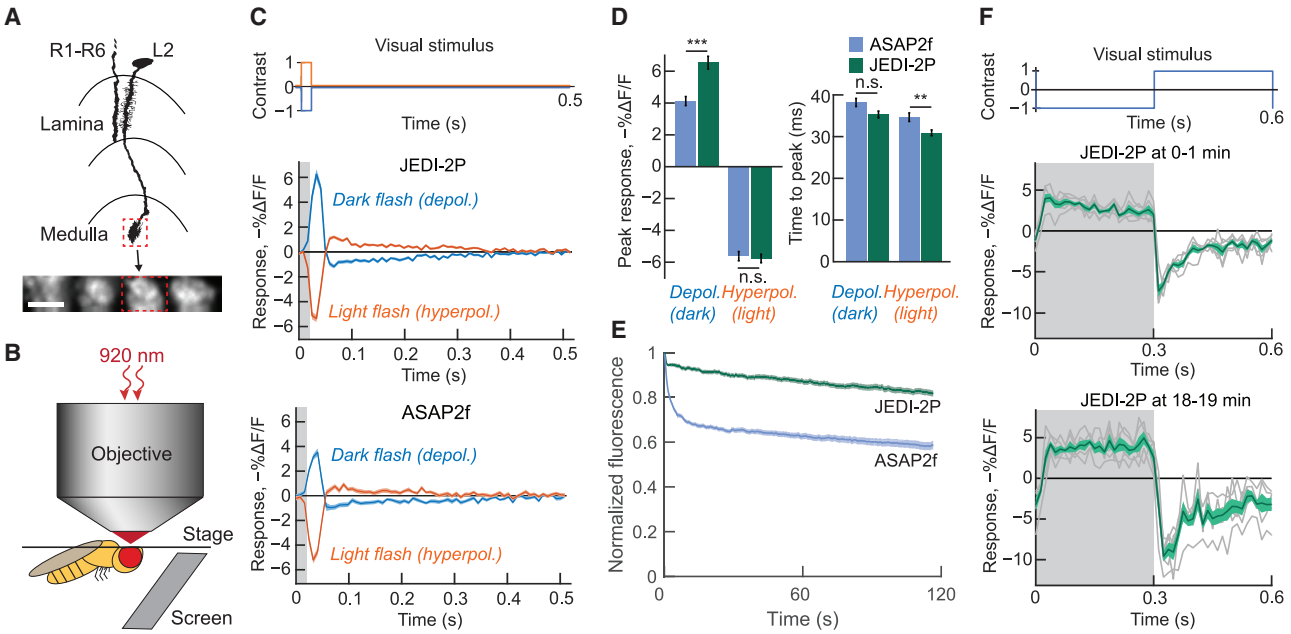

Figure 4. JEDI-2P reports light-evoked axonal voltage transients with large response amplitude, rapid kinetics, and high photostability

(A) We imaged the axonal projections of L2 cells, non-spiking neuron postsynaptic to photoreceptors (R1–R6). *Bottom*, representative field of view showing groups of axonal termini of four neighboring cells expressing JEDI-2P. Scale bar, 5 μm.

(B) Schematic of our experimental setup.

(C) We presented 20-ms light and dark flashes from a mean gray background (top graph and light gray shading in graphs below) and measured light-evoked fluorescence responses. Colored lines are the mean of n = 47 cells from 4 flies (JEDI-2P) and 40 cells from 4 flies (ASAP2f).

(D) Quantification of the responses in (C). JEDI-2P reported depolarizations with a larger response amplitude than ASAP2f (*left*) and with similar or faster response kinetics (*right*). Mean values are shown. *** p = 0.000015; ** p = 0.0054; n.s. not significant (t test with Bonferroni correction).

(E) JEDI-2P is more photostable than ASAP2f. Laser power, 16 mW (measured after the objective). Mean fluorescence values are shown, normalized to the fluorescence at t = 0. To better visualize the photobleaching time course, light-evoked responses were minimized using a 520-ms rolling average. n = 43 cells (JEDI-2P) and 29 cells (ASAP2f), each from 4 flies.

(F) JEDI-2P robustly reports voltage responses over the course of 20 min. We displayed alternating 300 ms light (unshaded areas) and dark flashes (gray shaded areas) throughout the entire recording. Mean JEDI-2P responses (dark green traces) during the first minute of recording (*middle*) and during the 19th minute of recording (*bottom*) were comparable. Gray traces show stimulus-evoked averages of the response over 1 min for each of the n = 6 cells from the same fly. Traces in all panels except (E) were baseline corrected. All shaded areas and error bars denote the SEM.

See also Figure S5 and Table S1.

that previous GEVIs were benchmarked in this cell type (Chamberland et al., 2017; Yang and St-Pierre, 2016). L2 cells depolarize to dark flashes and hyperpolarize to light flashes (Nikolaev et al., 2009). Awake transgenic flies selectively expressing JEDI-2P in L2 cells were positioned in front of a screen displaying brief light or dark flashes from a mean gray background (Figure 4B). The responses of axon termini from individual cells were monitored by galvanometric scanning of a 2P laser through a window cut in the cuticle at the back of the head. For comparison, we used transgenic flies expressing ASAP2f, a GEVI that reports L2 responses with a time course comparable with electrophysiological measurements (Yang et al., 2016). JEDI-2P produced ~60% larger responses than ASAP2f to depolarizing (dark) flashes with similarly fast response kinetics (Figures 4C and 4D). The response amplitude and kinetics to hyperpolarizing (light) flashes were similar between JEDI-2P and ASAP2f. Because the performance of ASAP3 for imaging in flies had not been reported, we evaluated this indicator in the same assay. Consistent with its reduced performance under 2PM *in vitro* (Figure 2), ASAP3 did not produce larger response amplitudes to either dark or light flashes than ASAP2f, and its response kinetics were slower (Figure S5).

Because behavioral and physiological assays in flies can last for several minutes, we evaluated JEDI-2P's suitability for reporting voltage over extended durations. JEDI-2P was more photostable than ASAP2f: at the end of the 2-min experiments, JEDI-2P retained 81.6% ± 1.4% (mean ± SEM) of its initial fluorescence compared with 58.4% ± 2.0% for ASAP2f. (Figure 4E). We also confirmed that JEDI-2P can report voltage dynamics with similar response amplitudes over nearly 20 min of continuous illumination (Figure 4F). Minor changes in the response waveform were observed, likely due to stimulus adaptation. These results demonstrate that JEDI-2P enables the imaging of short light-evoked voltage transients in *Drosophila* with large response amplitude, rapid kinetics, and excellent photostability.

Extended 2P imaging of voltage dynamics in mice with resonant-scanning microscopy

Having demonstrated improved performance of JEDI-2P in flies, we next deployed this indicator for reporting voltage dynamics in

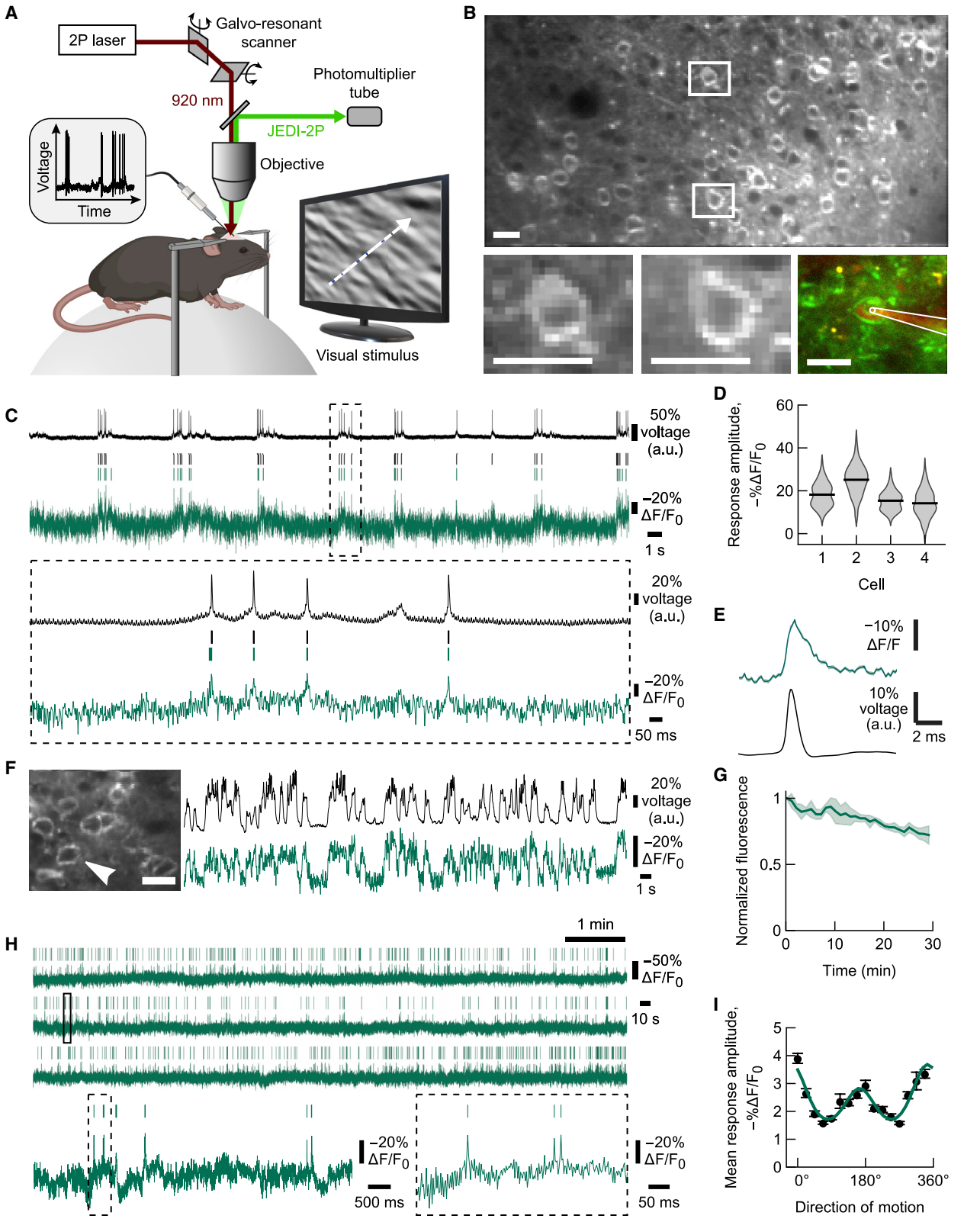

(legend on next page)

mice. Although resonant-scanning 2PM is broadly available in the neuroscience community, its application to robustly detect spikes in mice has not yet been demonstrated. We thus set out to evaluate the ability of JEDI-2P to monitor voltage changes using a standard resonant-scan microscope typically used for calcium imaging (Figure 5A) (Reimer et al., 2016).

We first optimized expression conditions to minimize background fluorescence from the neuropil. We restricted the indicator to the soma and proximal dendrites by appending a short peptide motif from the potassium channel Kv2.1, as previously reported (Daigle et al., 2018). We injected AAVs encoding JEDI-2P under the control of the Cre recombinase in transgenic mice expressing Cre in excitatory cells. Under these conditions, we obtained moderately dense populations of bright JEDI-2P-expressing neurons throughout the injection site in layer 2/3 of the visual cortex (Figure 5B). JEDI-2P was expressed in ring-like patterns, consistent with localization at the plasma membrane and enrichment in somata.

To quantify the ability of JEDI-2P to report spikes, we conducted simultaneous fluorescence imaging at 440 Hz and loose-patch juxtacellular recordings in anesthetized mice (Figures 5B–5G). We ensured our preparations were stable and performed basic XY motion correction using image registration against a template. We observed that JEDI-2P could report spikes with a $-18.2\% \pm 4.8\%$ change in fluorescence ($\Delta F/F_0$); numbers reported as mean ± 95% CI here and henceforth in this section (Figures 5C, 5D, and S6A–S6C).

To quantify our ability to infer spikes from the optical data, we used *VolPy*, an automated pipeline for spike detection from voltage imaging datasets (Cai et al., 2021). We compared the actual and predicted spike rates in 40-ms bins, the primary bin size used in a spike-inference competition using data from calcium indicators (Berens et al., 2018). The correlation (Pearson's r^2) between spikes predicted by *VolPy* and those identified by juxtacellular recordings was 0.64 ± 0.18 (range: 0.43–0.84 across individual neurons). *VolPy*'s default parameters were used, and optimizing these parameters would likely improve correlations. For context, the spike-inference competition using calcium imaging data produced correlations between 0.25 and 0.44, depending on the algorithm. However, we note that a direct comparison of spike inference using JEDI-2P and calcium dyes or indicators would require datasets where both calcium and voltage were monitored simultaneously. Given the faster temporal resolution of voltage imaging, we also evaluated spike inference under conditions where electrical and optical spikes were matched within narrower time spans. Because quantifying the correlation coefficient with narrow time bins can produce boundary artifacts (method details), we used the F_1 score to represent the accuracy of spike detection. We obtained F_1 scores of 0.58 ± 0.16 and 0.62 ± 0.15 for time spans of 5 and 10 ms, respectively (Figure S6D). These results show that JEDI-2P is a valuable (albeit not perfect) indicator for spike-rate prediction with resonant-scanning microscopy.

To compare spike waveforms obtained optically and electrophysiologically, we first quantified the changes in JEDI-2P fluorescence with 1,358 spontaneous spikes from the same neuron. We then performed a spike-triggered analysis at the level of individual pixels. Since the acquisition time of each pixel was recorded and the optical trace was synchronized with the electrical trace, we could determine the time at which each pixel was recorded relative to each AP peak. (Figures S6E and S6F). We also calculated the response amplitude from each of these pixels. The resulting datapoints were averaged with a time resolution of 0.23 ms, producing a spike waveform with a 4.4-kHz effective sampling rate (Figure 5E, *top*). The resulting optical trace showed a time-to-peak of 1.7 ms and a full width at half maximum (FWHM) of 2.1 ms, slightly larger than the values obtained from electrophysiological measurements (1.3 and 1.1 ms for the time-to-peak and FWHM, respectively) (Figure 5D). These measurements are consistent with JEDI-2P's kinetics *in vitro* (Table S2) and demonstrate that our indicator can track APs with exquisite temporal resolution.

Subthreshold activity is of high interest for understanding information processing in single and groups of neurons. Synchronized brain states of increased firing (UP states) and relative

Figure 5. JEDI-2P enables long-lasting 2P imaging of voltage dynamics in mice using resonant-scanning microscopy

(A) Experimental setup schematic. Data were collected while the mouse was presented with visual stimuli consisting of Gaussian noise with coherent orientation and motion. Mice were head fixed and free to behave on a non-motorized circular treadmill. Recordings were acquired in layer 2/3 cells of the visual cortex. Imaging was conducted at 440 Hz unless otherwise noted.

(B) All experiments used JEDI-2P with a soma-localization tag. *Top*, representative image of soma-targeted JEDI-2P in the visual cortex. *Bottom left and middle*, zoomed-in images of the cells highlighted in the white boxes. *Bottom right*, fluorescence image of a neuron being simultaneously patched and imaged. The position of the pipette is outlined in white. Green fluorescence is from JEDI-2P, and red is from the dye Alexa Fluor 594 present in the pipette. Scale bars, 20 μm.

(C–F) Simultaneous optical and loose-patch juxtacellular recordings in anesthetized animals. (C) Example recording. Vertical lines indicate spikes identified in the electrophysiological recording (black) or predicted from the optical trace using *VolPy* (green). The dashed box shows a zoomed-in section. (D) Distribution of the optical responses to spikes. Data are shown as violin plots with the black bars denoting the mean. n = 4 cells from 2 mice. (E) JEDI-2P's optical response to spikes (*top*) closely tracked the underlying electrical waveform (*bottom*). Waveforms were averaged from 1,358 spikes (identified from the electrophysiological trace) from the same cell. The shaded area (small) denotes the SEM. (F) Global UP-DOWN states can be monitored by voltage imaging. *Top*, electrophysiological recording. *Bottom*, JEDI-2P responses from a single cell (arrow) were recorded at 150 Hz. JEDI-2P recordings at 150 Hz (green) tracked the electrophysiological changes monitored 1 mm from the site of optical recording. The optical trace was recorded from a single cell (arrow). Scale bar, 20 μm.

(G–I) Optical-only recordings in awake behaving mice. Cells were between 170 and 225 μm from the surface of the brain. (G) JEDI-2P is photostable under resonant-scan 2PM. Laser power was 34 mW (measured after the objective). Fluorescence was normalized to values at t = 0. The thick line denotes the mean, and shaded areas are the 95% CI. n = 4 cells from the same animal. (H) Example of a 30-min optical recording in an awake behaving mouse at a depth of 170 μm. Vertical lines are *VolPy*-predicted spikes. (I) JEDI-2P can report directional tuning of individual neurons. For each direction of motion, fluorescence responses were averaged over the entire trace and thus include spikes, subthreshold potentials, and periods with no voltage changes. Acquisition frequency was 233 Hz to capture a larger field of view than at 440 Hz. Green lines indicate the data fitted by a von Mises function (Reimer et al., 2014). Error bars are the 95% CI. n = 20 trials. Traces in all panels except (G) were baseline corrected and a.u. denotes arbitrary units.

See also Figures S6 and S7 and Table S1.

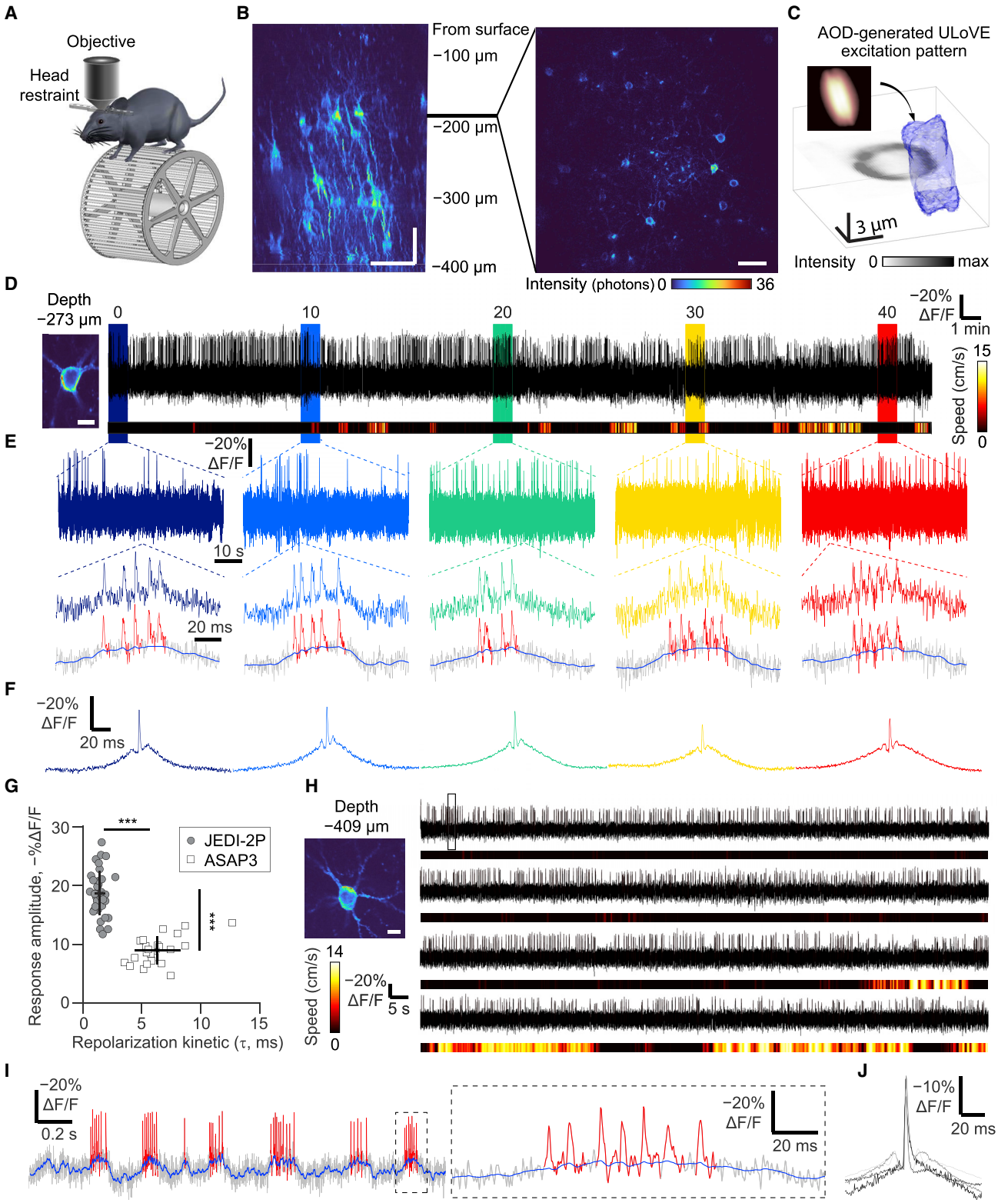

Figure 6. Sustained high-fidelity 2P voltage recordings in cortical layers 2/3 and 5 using JEDI-2P and ULoVE microscopy

(A) During voltage recording, the head-fixed mouse is free to behave on a non-motorized wheel.

(B) Representative YZ projection (*left*) and single XY plane (*right*) showing sparsely expressed JEDI-2P in the visual cortex. Images were acquired by 2P point scanning. The XY plane shows ring-like patterns of expression because all ULoVE experiments used GEVIs appended with a soma-localization tag. Scale bars, 50 µm.

(legend continued on next page)

quiescence (DOWN states) have been observed during sleep, under anesthesia, and during perceptual tasks (Jercog et al., 2017). Shifts in the subthreshold membrane potential underlie these states, with APs preferentially arising during the UP states (Stern et al., 1997). To determine whether global UP and DOWN states could be detected by voltage imaging, we recorded fluorescence with a frame rate of 150 Hz at a site about 1 mm away from a cell recorded using intracellular patch clamping. We observed global UP-DOWN states, as expected under isoflurane anesthesia, and the optical signals qualitatively tracked these subthreshold variations (Figure 5F). These results suggest that JEDI-2P can report subthreshold signals of functional relevance to cortical information processing. However, we note that rapid or small subthreshold depolarizations remain difficult to detect accurately (Figures 5C and S6C).

To evaluate JEDI-2P's photostability, we deployed JEDI-2P for voltage imaging sessions in awake behaving mice without simultaneous electrophysiological measurements. JEDI-2P's photostability was excellent, retaining 72.4% ± 0.1% of its fluorescence over 30 min of imaging with 34 mW of power (measured after the objective) (Figure 5G). Recordings were typically stopped at 30 min, as this duration was sufficient to demonstrate extended voltage imaging. We observed robust responses to presumed spikes and subthreshold depolarization throughout the recordings (Figures 5H, S7A, and S7B). We did not observe changes in the amplitude and rate of the detected spikes, suggesting that continuous illumination did not overtly impact neuronal excitability and indicator properties (Figures S7C–S7E).

We next demonstrated that JEDI-2P could be used to characterize the functional properties of individual visual cortical neurons in response to a visual stimulus. We recorded voltage dynamics, including spiking activity and subthreshold depolarizations, in response to Gaussian noise stimulus with coherent orientation and motion. We observed multiple neurons whose activity depended on the direction of motion (Figures 5I, S7F), as is common in V1 neurons (Fahey et al., 2019). Together, these results demonstrate that imaging JEDI-2P with standard resonant-scanning 2PM can report voltage dynamics at high temporal resolution in awake behaving mice.

JEDI-2P enables long-lasting deep-layer voltage recording and reveals pairwise voltage correlations in awake behaving mice

Having demonstrated 2PM voltage imaging with resonant-scanning microscopy, we sought to evaluate JEDI-2P under alternative recording modalities that are advantageous for monitoring rapid voltage transients. We have previously reported ULoVE multiphoton microscopy, a random-access technique that samples a local volume around a target point (Villette et al., 2019). ULoVE excitation volumes can be shaped so that a greater fraction of the cellular volume is sampled than with resonant-scanning microscopy, enabling fast recordings with high signal-to-noise ratio and low photobleaching rates. Finally, because the excitation volume can be larger than the imaged structure (e.g., a cell soma or a dendrite), ULoVE can insulate the signal from motion artifacts in awake behaving mice (Villette et al., 2019).

We performed ULoVE voltage recordings in head-fixed mice that were free to run on a non-motorized wheel and were not presented with visual stimuli (Figure 6A). We reduced contaminating neuropil signal using similar strategies as our resonant-scanning experiments, including the use of the soma-localized variant of JEDI-2P. We further increased the sparsity of fluorescent cells by expressing Cre from an AAV and co-injecting an optimized amount of this virus (Figure 6B). Single somas were illuminated with two sequential excitation patterns using 15 mW of power (Figures 6C and S8A). Collected photons were integrated into a single readout (number) per time point, akin to a soma being represented by one large pixel rather than a two-dimensional image. Recordings were conducted at 2.5–5 kHz, corresponding to a ~5- to 11-fold increase in temporal resolution compared with our resonant-scanning experiments.

We sequentially recorded 36 layer 2/3 neurons across five awake behaving mice, with recording time reaching 42 min (13.2 ± 5 min; numbers reported as mean ± SD here and henceforth; Figures 6D, 6E, and S8B). The signal-to-noise ratio at the end of the recordings was excellent; except for long sessions performed to demonstrate the indicator's photostability, recordings were stopped when they were of sufficient duration for the analyses discussed below. We used the MLspike method (Deneux et al., 2016) to infer the timing and amplitude of spikes and subthreshold fluctuations (Figure 6E, *bottom*). JEDI-2P responded to spikes with a −18.4% ± 3.5% change in fluorescence (Figures 6F and 6G), similar to what we observed under resonant-scanning microscopy. Spikes were elicited during UP states, as observed previously (Villette et al., 2019). JEDI-2P's mean response to UP states was −15.5% ± 3.1% (range: −10.3% to −22%) (Figures S8F–S8H). We quantified the characteristics of the optical signal over 25 min of continuous recording. The firing rate, response amplitude to APs, and optical spike

(C) A ULoVE excitation pattern overlaid onto a slice of a single cell. To cover both halves of a cell, we rapidly alternated between two patterns (Figure S8A).
(D–F) Representative optical recording of a layer 2/3 neuron. (D) *Left*, point-scanning 2PM image of the neuron acquired before ULoVE recording. Scale bar, 10 μm. *Right*, Fluorescence from more than >40 min of continuous ULoVE optical recording. Heatmap below indicates the wheel speed. (E) Zoomed-in traces of the fluorescence signal from (D). The last row shows the fluorescence signal (gray) overlaid with MLspike-extracted spikes (red) and slow voltage changes (blue). (F) Average optical spike waveforms from the 1-min time windows indicated in (D).
(G) Amplitude versus repolarization kinetic (τ) of the optical response to APs from n = 23 (ASAP3) (Villette et al., 2019) and 36 (JEDI-2P) neurons in layer 2/3 of the visual cortex. The crosshair marks indicate mean ± SD. *** p = 3.8E−11 (response amplitude) and 4.4E−13 (τ), two-sample Kolmogorov-Smirnov test.
(H–J) Representative optical recording of a layer 5 pyramidal neuron. (H) *Top left*, Point-scanning 2PM image of the neuron acquired before ULoVE recording. Scale bar, 10 μm. *Right*, fluorescence signal during behavior. Heatmap below indicates the wheel speed. (I) Zoomed-in trace from (H) (dashed box), with the fluorescence signal shown in gray. MLspike-extracted spikes (red) and slow voltage changes (blue) are overlaid. The dashed boxed (*right*) shows a zoomed-in view of a spike burst. (J) Average optical spikes from the four cells recorded in layer 5; different shades of gray indicate different cells. Traces in all panels were baseline corrected.
See also Figures S8 and S9 and Table S1.

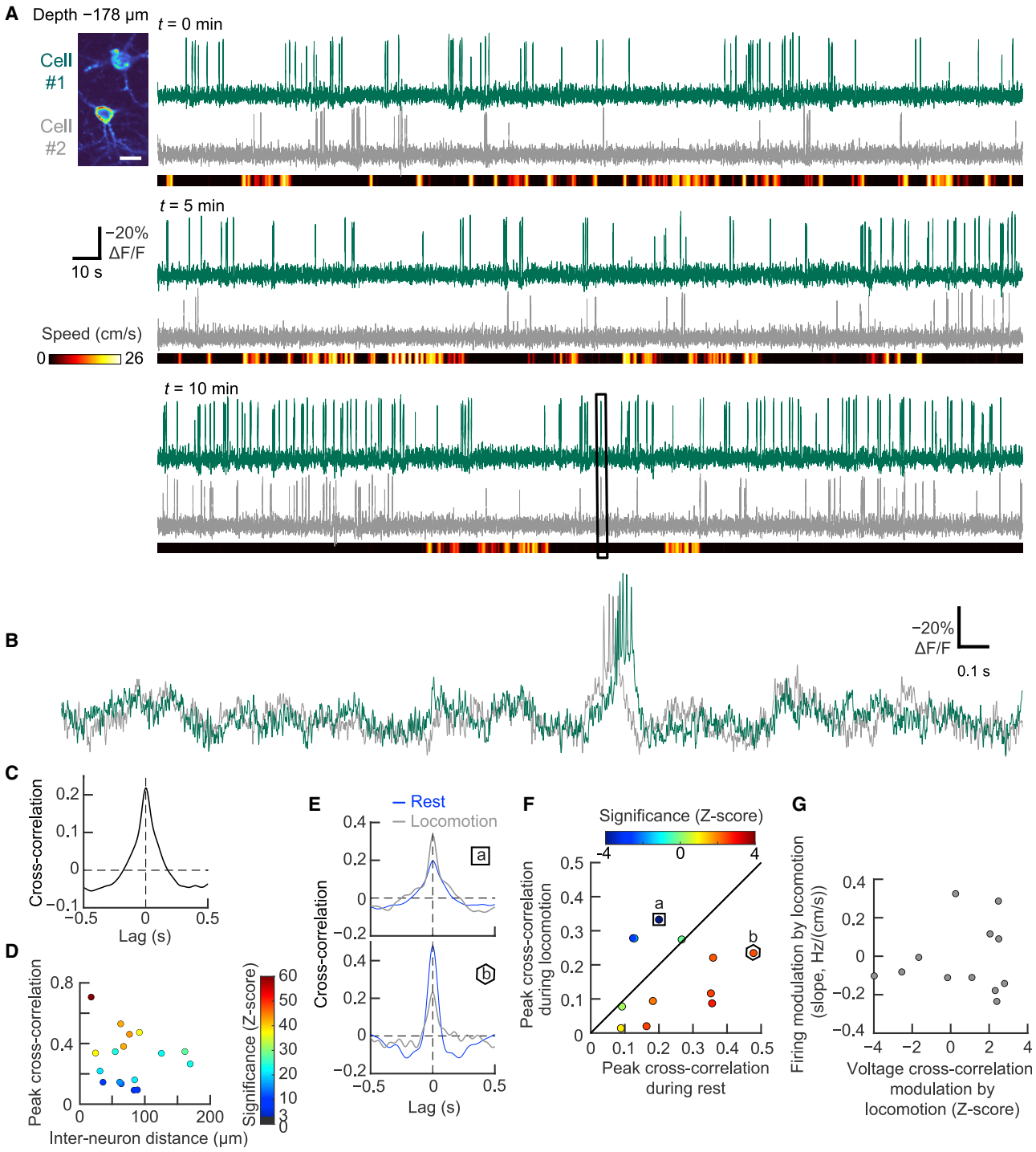

Figure 7. ULoVE optical recording of JEDI-2P enables long-lasting recording of pairwise voltage correlations during behavior

(A) Baseline-corrected fluorescence signals from two neurons of layer 2/3 recorded simultaneously for 15.4 min. Heatmap below indicates the wheel speed. Traces were smoothed with a 1-ms Gaussian kernel for display only. *Top left*, point-scanning 2PM image of the neurons acquired before ULoVE recording. Scale bar, 10 µm.

(B) Zoomed-in traces of the fluorescence signal in (A) (box) but overlaying the two cell traces. Note the subthreshold co-modulation.

(C) Voltage cross-correlation of the cell pair from (A) calculated over the entire recording.

(D) The pairwise voltage cross-correlation is highly variable but not significantly affected by the distance between the neurons. Pearson's r = −0.22, p = 0.41 (linear regression t test). The color code represents the significance (*Z* score) of the cross-correlation, as obtained from a bootstrap evaluation. n = 17 cell pairs.

(legend continued on next page)

width remained unchanged, suggesting that continuous illumination did not appreciably affect neuronal excitability, indicator properties, and the underlying (electrical) spike waveform (Figures S8C–S8E).

We sought to compare JEDI-2P with ASAP3, which we previously imaged with ULoVE (Villette et al., 2019). Consistent with *in vitro* measurements (Figure 2E), JEDI-2P produced >2-fold larger responses to spikes than ASAP3 (Figure 6G). JEDI-2P's repolarization kinetics were 1.43 ± 0.44 ms (range: 0.6–2.8 ms), >4-fold faster than ASAP3's decay time constant (6.34 ± 1.94 ms; Figure 6G). JEDI-2P's rapid kinetics were critical to identifying closely spaced spikes (e.g., Figure 6E), thereby enabling the quantification of spike correlations. Fast indicator kinetics are essential because although average firing rates were modest (range: 0.09–18.2 Hz), 38% ± 23.3% of spikes were in bursts, and the intra-burst firing rate was 261 ± 112 Hz. Finally, JEDI-2P had greater photostability than ASAP3, with a reduced fast-bleaching component amplitude and an overall increase in the time integral of the normalized photon flux (Figures S8I and S8J). Overall, JEDI-2P provided critical advantages for spike detection over ASAP3 due to its 2-fold larger responses to spikes, faster depolarization and repolarization kinetics, and enhanced photostability.

We next sought to determine whether the improved performance of JEDI-2P enabled voltage recordings across a broader range of conditions than previously possible. Specifically, we evaluated its ability to report voltage dynamics beyond 400 μm in cells that we presume were layer 5 pyramidal neurons based on their large diameters (MICrONs Consortium et al., 2021) (Figure S9A). We could not achieve robust spike recording in layer 5 somas using ASAP3 (Villette et al., 2019). Layer 5 recordings are challenging because increased depth decreases the efficiency of indicator excitation and photon collection: JEDI-2P-expressing neurons in layer 5 (430.2 ± 19.8 μm) produced a ~7-fold lower photon flux than neurons in layer 2/3 (170 ± 45.9 μm; Figures S9B and S9C). Despite the reduced rate of photon collection, JEDI-2P reported individual spikes with a high signal-to-noise ratio in continuous recordings of 12 ± 5 min (Figures 6H–6J and S8B). Responses to APs were −20.3% ± 5.32% (range: −17.5% to −28%), similar in amplitude to those observed in layer 2/3 (Figures S9D and S9E). Having recorded neurons in layers 2/3 and 5 enabled a quantitative comparison of their spontaneous activity. We did not observe significant differences in spiking frequency, AP width, and UP-state magnitude between our recordings in the two layers (Figures 6J and S9F–S9H). Taken together, our data constitute the first robust voltage recordings of layer 5 somas under 2PM.

We hypothesized that the improved properties of JEDI-2P would enable recording pairs of neurons, which would pave the way for optically investigating voltage correlations in cortical networks. To monitor two cells without decreasing the dwell time per cell, we reduced our acquisition rate from 5 to 2.5 kHz (Figure S8A). Because the acquisition rate remained faster than the spike width, APs were easily detectable throughout the pairwise recordings (Figure 7A). We monitored a total of 17 pairs of layer 2/3 neurons (cell separation: 77 ± 43 μm, range 18–169 μm; depth range: 111–248 μm). We observed that the overall voltage traces were positively correlated in all pairs (Figures 7B, 7C, and S10A). The amplitudes of the correlations were highly variable between cell pairs, and this variability was not explained by the distance between cells within a pair (Figure 7D). Spike-triggered averages of the membrane potential of neurons within a pair were positively correlated with a timespan (SD of Gaussian fits) of 48.9 ± 25.5 ms (Figure S10B). Although we did not observe a significant correlation in spiking activity on a timescale of 1 ms, 7 of 17 pairs displayed correlations on a 15-ms timescale (Figures S10C and S10D). The spike-train cross-correlation amplitudes were not significantly correlated with the cross-correlation amplitudes of the overall voltage traces (Figure S10E). Overall, these results suggest that subthreshold correlations in the visual cortex can reveal information on brain states distinct from that reported by spike trains.

Finally, we took advantage of the stability of our optical recordings to examine the influence of locomotor behavior on subthreshold voltage correlations between neurons, a feat that would otherwise require challenging paired whole-cell electrical recordings in awake animals. In 9 of the 12 recordings that displayed sufficiently long locomotion epochs to enable analysis, we observed that voltage cross-correlation was modulated by locomotion. Six pairs displayed a significant decrease in correlation during locomotion epochs (−62.7% ± 19.4%), whereas three pairs showed a significant increase in their cross-correlation (+106.4% ± 34.3%; Figures 7E, 7F, S10F, and S10G). Locomotion was not associated with a mean increase in the variance of the spike-free trace, as we would have expected if these results were due to motion artifacts (Figure S10H). The modulation of voltage cross-correlation by locomotion was neither correlated with a cell pair's spike-rate modulation by locomotion (Figure 7G) nor with changes in traces' coefficient of variation by locomotion (Figure S10I).

Dual intracellular recordings in the barrel cortex have shown that subthreshold activity is highly correlated during quiet wakefulness and that this correlation is reduced upon active whisking (Poulet and Petersen, 2008). It was suggested that the decorrelation of membrane potential during active states augments

(E–F) Locomotion increased or decreased voltage cross-correlation in different cell pairs. (E) Representative cell pairs showing opposite modulation of their voltage cross-correlation by locomotion. Cell pair (a) is the pair shown in (A)–(C). (F) Normalized peak voltage cross-correlation during locomotion and rest epochs for the n = 12 cell pairs analyzed. Color code represents the significance (*Z* score) of the difference between rest and locomotion cross-correlations, relative to randomly chosen episodes of the same durations. (a) and (b) correspond to the two pairs of neurons shown in (E). The black diagonal line indicates identical cross-correlation values between rest and locomotion epochs.

(G) The modulation of voltage cross-correlation by locomotion was not correlated with the degree of spike-rate modulation by locomotion of the two cells of each pair. Pearson's r = 0.11, p = 0.73 (linear regression t test). Data points are the average of each pair. For all experiments, the soma-localized variant of JEDI-2P was used.

See also Figure S10 and Table S1.

cortical information processing capacity. Although our results in the visual cortex also show that active behavior (locomotion) is associated with an attenuation in the correlation between subthreshold voltage changes in some cell pairs, locomotion unexpectedly produced increased correlation in other neuron pairs. This observation motivates further research into how and why correlated subthreshold activity can be differentially modulated between cell pairs. More generally, the optical method demonstrated here enables *in vivo* monitoring of sub- and suprathreshold network dynamics more easily and less invasively than electrophysiological methods.

DISCUSSION

Implications for the adoption of GEVIs for *in vivo* voltage recordings

In this study, we report on JEDI-2P, a new voltage indicator that addresses a critical need in neuroscience: the noninvasive recording of rapid voltage transients for extended durations and in deep cortical layers. We evaluated JEDI-2P for reporting voltage dynamics in different cell types, subcellular locations, and animal models (also see Behrens et al., 2022). We also demonstrated that JEDI-2P could record voltage responses using distinct 2PM microscopy methods.

Negative-going indicators like JEDI-2P, which become dimmer upon depolarization, have several advantages compared with positive-going indicators. They are brighter at the resting membrane potential, enabling improved detection of hyperpolarizations and small subthreshold depolarizations—two signal types of enormous interest for understanding neuronal information processing. Silent cells with negative-going indicators are bright by default, thus avoiding the cell selection bias toward active neurons that can occur with positive-going indicators (e.g., GCaMP) when inactive cells are challenging to identify. However, positive-going indicators have the potential for increased spike detectability (Wilt et al., 2013), greater photostability, and lower background fluorescence. They would thus be desirable additions to the voltage recording toolbox.

Implications for indicator engineering

To empower *in vivo* voltage recordings, we sought to avoid pitfalls from previous engineering efforts where an improvement in one characteristic was often accompanied by an impairment in another. To build a "no compromise" indicator, we developed a multiparameter screening platform that simultaneously evaluates GEVIs based on multiple performance metrics. As a result, JEDI-2P has improved performance in *all* fundamental properties: it is faster, brighter, and more photostable and responsive than all previous GEVIs for 2PM, including its parental indicator (ASAP2s) and the last iteration of the ASAP family of sensors (ASAP3).

Our results illustrate the perils of screening indicators under different illumination conditions than the intended downstream applications. For example, ASAP3 produced larger response amplitudes under widefield 1PM—the illumination modality used during its development—than under laser-scanning 2PM. Further studies are needed to precisely determine what change in experimental conditions (e.g., 1P vs. 2P excitation, illumination power or wavelength) is primarily responsible for the observed difference in ASAP3's response amplitudes. We anticipate that our results will motivate using 2PM-based screening to develop a new generation of designer indicators for deep-tissue recording of calcium, neurotransmission, and other aspects of cellular activity.

Limitations of the study

Although JEDI-2P enables new voltage recording experiments, further improvements in response amplitude, kinetics, brightness, and photostability would be desirable when recording in challenging conditions: deeper structures, smaller voltage changes, narrower spikes, or smaller subcellular areas such as spines. Performance improvements can be achieved by mutating the many residues that were not targeted in this study and could be accelerated by new single-cell screening approaches such as SPOTlight (Lee et al., 2020). Improvements in optical techniques and spike inferencing algorithms would also be valuable to improve the reliability of voltage signal detection.

Overall, our results demonstrate the broad utility of JEDI-2P for high-fidelity and sustained recording of voltage dynamics *in vivo*. We anticipate that our report will encourage neuroscientists—including those more familiar with calcium imaging—to exploit the unique advantages of voltage indicators to decipher neuronal computations with millisecond-timescale resolution.

STAR★METHODS

Detailed methods are provided in the online version of this paper and include the following:

- KEY RESOURCES TABLE
- RESOURCE AVAILABILITY
  - Lead contact
  - Materials availability
  - Data and code availability
- EXPERIMENTAL MODEL AND SUBJECT DETAILS
  - Cell lines
  - Fly experiments
  - Retinal explants
  - Mice experiments with resonant scanning microscopy
  - Mice experiments with ULoVE microscopy
- METHOD DETAILS
  - Reagents for screening and *in vitro* benchmarking
  - High-throughput GEVI screening
  - ASAP2s *in silico* structure prediction
  - GEVI characterization *in vitro*
  - 2P voltage imaging in isolated mouse retina
  - Voltage imaging in *Drosophila* visual neurons using galvanometric point-scanning 2PM
  - Voltage imaging in the mouse cortex using resonant scanning 2PM
  - Voltage recording in the mouse cortex using ULoVE
- QUANTIFICATION AND STATISTICAL ANALYSIS

SUPPLEMENTAL INFORMATION

Supplemental information can be found online at https://doi.org/10.1016/j.cell.2022.07.013.

ACKNOWLEDGMENTS

We thank Dr. B. Arenkiel, J. Ortiz-Guzman, and Z. Chen at the TCH Neuroconnectivity Core for AAV packaging; this facility is supported by NIH grant P50HD103555 and the Charif Souki Fund. We thank J.M. Kirk, H. Johnson and the Imaging & Vital Microscopy Core (Baylor College of Medicine, BCM) for training on the confocal microscope and the plate reader. We thank F.A. Blanco, C.A. Cronkite, and Dr. J.G. Duman from Dr. K.R.F. Tolias lab (BCM) for preparing neurons. We acknowledge H. Yang and M. Xie (Clandinin lab) for developing the stimulus presentation and analysis code used in the fly imaging pipeline. We thank R. Kroeger (Reimer lab) for helping with 2P imaging. We thank B. Mathieu and the IBENS imaging facility (IMACHEM-IBiSA), member of the French National Research Infrastructure France-BioImaging (ANR-10-INBS-04), which received support from the "Fédération pour la Recherche sur le Cerveau—Rotary International France" (2011) and from the program «Investissements d'Avenir» ANR-10-LABX-54 MEMOLIFE. We thank A. Lombardini for helping with the multiphoton microscope, IBENS PFL2 platform, IBENS animal facility, and Y. Cabirou for custom mechanical production. The project was supported by the Klingenstein-Simons Fellowship Award in Neuroscience (F.S.-P.); the McNair Medical Foundation (F.S.-P.); Welch Foundation grant Q-2016-20190330 (F.S.-P.); an NDSEG fellowship (M.M.P.); NIH grants R01EB027145 (F.S.-P.), U01NS113294 (F.S.-P., A.T., J.R.), U01NS118288 (F.S.-P.), R01EY022638 and P30 EY026877 (T.R.C.), and U01NS103464 (S.D.); NSF NeuroNex grant 1707359 (F.S.-P., A.T., J.R.) and IdeasLab grant 1935265 (F.S.-P.); Beckman Young Investigator Fellowship (A.G.); startup funds from the Joint Biomedical Engineering Department of University of North Carolina at Chapel Hill and North Carolina State University (A.G.); German Federal Ministry of Education and Research 01GQ1002 (K.F.); Max Planck Society M.FE.A.KYBE0004 (K.F.); German Research Foundation focus program SPP2041 Computational connectomics (A.V.), the University of Tübingen Fortuene Fellowship (A.V.); the Christiane-Nuesslein-Volhard Stiftung (A.V.); INSERM (J.B. and S.D.); CNRS (V.V., and A.A.); and ENS (J.B., V.V., and S.D.).

AUTHOR CONTRIBUTIONS

F.S.-P. conceived the project. F.S.-P., coordinated the project with help from Z.L., X.L., and M.A.L. GEVI screening and *in vitro* characterization: Z.L. developed the screening platform hardware and data analysis code; Z.L., X.L., and K.L.C. developed the screening platform software; X.L., Y.G., and D.R.Z. developed screening protocols; X.L., Y.G., S.L., and T.A. screened GEVIs; X.L., S.G., and J.L. characterized GEVIs *in vitro*; X.L. and S.G. cloned viral vectors; Z.L., X.L., J.L., M.A.L., and F.S.-P. prepared figures and wrote the manuscript. Experiments in retinal explants: A.L.V. and K.F. designed the experiments; K.F. performed viral injections; M.K. performed imaging experiments with input from A.L.V.; A.L.V. and K.F. analyzed the data; Z.L., A.L.V., and K.F. prepared the figures and wrote the manuscript. Experiments in *Drosophila*: M.M.P., S.S., and T.R.C. designed the experiments and wrote the manuscript; M.M.P. and S.S. conducted the experiments and analyzed data. Experiments in mice with resonant scanning: A.S.T. and J.R. designed and oversaw the experiments; E.F., N.Z., and J.R. conducted the experiments; Z.L., E.F., S.S.P., C.L.S., C.C., A.G., and J.R. analyzed the data; Z.L., S.S.P., and J.R. prepared figures; and A.S.T. and J.R. wrote the manuscript. Experiments in mice with ULoVE: V.V. and S.D. designed the experiments; V.V. performed the experiments; P.B. and S.D. designed and built the ULoVE microscope; A.A. contributed to the viral expression strategy and viral production; J.B. managed and designed the genetic strategy; V.V. analyzed the data; V.V., J.B., and S.D. wrote the manuscript and prepared figures with figure assistance from Z.L.

DECLARATION OF INTERESTS

F.S.-P. holds a US patent for a voltage sensor design (patent #US9606100 B2). F.S.-P., Z.L., and J.L. have filed a US patent for the SPOTlight screening method. S.D. and P.B. have ownership shares in Karthala Systems, a commercial supplier of RAMP microscopes.

Received: September 8, 2021
Revised: April 13, 2022
Accepted: July 18, 2022
Published: August 18, 2022

REFERENCES

Abdelfattah, A.S., Farhi, S.L., Zhao, Y., Brinks, D., Zou, P., Ruangkittisakul, A., Platisa, J., Pieribone, V.A., Ballanyi, K., Cohen, A.E., and Campbell, R.E. (2016). A bright and fast red fluorescent protein voltage indicator that reports neuronal activity in organotypic brain slices. J. Neurosci. *36*, 2458–2472. https://doi.org/10.1523/JNEUROSCI.3484-15.2016.

Adhikari, D.P., Biener, G., Stoneman, M.R., Badu, D.N., Paprocki, J.D., Eis, A., Park, P.S.-H., Popa, I., and Raicu, V. (2021). Comparative photophysical properties of some widely used fluorescent proteins under two-photon excitation conditions. Spectrochim. Acta A Mol. Biomol. Spectrosc. *262*, 120133. https://doi.org/10.1016/j.saa.2021.120133.

Ankri, L., Ezra-Tsur, E., Maimon, S.R., Kaushansky, N., and Rivlin-Etzion, M. (2020). Antagonistic Center-surround mechanisms for direction selectivity in the retina. Cell Rep. *31*, 107608. https://doi.org/10.1016/j.celrep.2020.107608.

Baden, T., Berens, P., Franke, K., Román Rosón, M., Bethge, M., and Euler, T. (2016). The functional diversity of retinal ganglion cells in the mouse. Nature *529*, 345–350. https://doi.org/10.1038/nature16468.

Behrens, C., Yadav, S.C., Korympidou, M.M., Zhang, Y., Haverkamp, S., Irsen, S., Schaedler, A., Lu, X., Liu, Z., Lause, J., et al. (2022). Retinal horizontal cells use different synaptic sites for global feedforward and local feedback signaling. Curr. Biol. *32*, 545–558.e5. https://doi.org/10.1016/j.cub.2021.11.055.

Berens, P., Freeman, J., Deneux, T., Chenkov, N., McColgan, T., Speiser, A., Macke, J.H., Turaga, S.C., Mineault, P., Rupprecht, P., et al. (2018). Community-based benchmarking improves spike rate inference from two-photon calcium imaging data. PLoS Comput. Biol. *14*, e1006157. https://doi.org/10.1371/journal.pcbi.1006157.

Bezanilla, F. (2008). How membrane proteins sense voltage. Nat. Rev. Mol. Cell Biol. *9*, 323–332. https://doi.org/10.1038/nrm2376.

Brinks, D., Klein, A.J., and Cohen, A.E. (2015). Two-photon lifetime imaging of voltage indicating proteins as a probe of absolute membrane voltage. Biophys. J. *109*, 914–921. https://doi.org/10.1016/j.bpj.2015.07.038.

Cai, C., Friedrich, J., Singh, A., Eybposh, M.H., Pnevmatikakis, E.A., Podgorski, K., and Giovannucci, A. (2021). VolPy: automated and scalable analysis pipelines for voltage imaging datasets. PLoS Comput. Biol. *17*, e1008806. https://doi.org/10.1371/journal.pcbi.1008806.

Chamberland, S., Yang, H.H., Pan, M.M., Evans, S.W., Guan, S., Chavarha, M., Yang, Y., Salesse, C., Wu, H., Wu, J.C., et al. (2017). Fast two-photon imaging of subcellular voltage dynamics in neuronal tissue with genetically encoded indicators. eLife *6*, e25690. https://doi.org/10.7554/eLife.25690.

Choy, E., Chiu, V.K., Silletti, J., Feoktistov, M., Morimoto, T., Michaelson, D., Ivanov, I.E., and Philips, M.R. (1999). Endomembrane trafficking of ras: the CAAX motif targets proteins to the ER and Golgi. Cell *98*, 69–80. https://doi.org/10.1016/S0092-8674(00)80607-8.

Chu, J., Oh, Y., Sens, A., Ataie, N., Dana, H., Macklin, J.J., Laviv, T., Welf, E.S., Dean, K.M., Zhang, F., et al. (2016). A bright cyan-excitable orange fluorescent protein facilitates dual-emission microscopy and enhances bioluminescence imaging in vivo. Nat. Biotechnol. *34*, 760–767. https://doi.org/10.1038/nbt.3550.

Cranfill, P.J., Sell, B.R., Baird, M.A., Allen, J.R., Lavagnino, Z., de Gruiter, H.M., Kremers, G.J., Davidson, M.W., Ustione, A., and Piston, D.W. (2016). Quantitative assessment of fluorescent proteins. Nat Methods *13*, 557–562. https://doi.org/10.1038/nmeth.3891.

Daigle, T.L., Madisen, L., Hage, T.A., Valley, M.T., Knoblich, U., Larsen, R.S., Takeno, M.M., Huang, L., Gu, H., Larsen, R., et al. (2018). A suite of transgenic driver and reporter mouse lines with enhanced brain-cell-type targeting and functionality. Cell *174*, 465–480.e22. https://doi.org/10.1016/j.cell.2018.06.035.

Dana, H., Mohar, B., Sun, Y., Narayan, S., Gordus, A., Hasseman, J.P., Tsegaye, G., Holt, G.T., Hu, A., Walpita, D., et al. (2016). Sensitive red protein calcium indicators for imaging neural activity. eLife *5*, e12727. https://doi.org/10.7554/eLife.12727.

Deneux, T., Kaszas, A., Szalay, G., Katona, G., Lakner, T., Grinvald, A., Rózsa, B., and Vanzetta, I. (2016). Accurate spike estimation from noisy calcium signals for ultrafast three-dimensional imaging of large neuronal populations in vivo. Nat. Commun. *7*, 12190. https://doi.org/10.1038/ncomms12190.

Derrington, A.M., and Lennie, P. (1982). The influence of temporal frequency and adaptation level on receptive field organization of retinal ganglion cells in cat. J. Physiol. *333*, 343–366. https://doi.org/10.1113/jphysiol.1982.sp014457.

Diamond, J.S. (2017). Inhibitory interneurons in the retina: types, circuitry, and function. Annu. Rev. Vis. Sci. *3*, 1–24. https://doi.org/10.1146/annurev-vision-102016-061345.

Dimitrov, D., He, Y., Mutoh, H., Baker, B.J., Cohen, L., Akemann, W., and Knöpfel, T. (2007). Engineering and characterization of an enhanced fluorescent protein voltage sensor. PLoS One *2*, e440. https://doi.org/10.1371/journal.pone.0000440.

Drobizhev, M., Makarov, N.S., Tillo, S.E., Hughes, T.E., and Rebane, A. (2011). Two-photon absorption properties of fluorescent proteins. Nat. Methods *8*, 393–399. https://doi.org/10.1038/nmeth.1596.

Enroth-Cugell, C., and Robson, J.G. (1966). The contrast sensitivity of retinal ganglion cells of the cat. J. Physiol. *187*, 517–552. https://doi.org/10.1113/jphysiol.1966.sp008107.

Euler, T., Franke, K., and Baden, T. (2019). Studying a Light Sensor with Light: Multiphoton Imaging in the Retina. In Multiphoton Microscopy, E. Hartveit, ed. (Springer), pp. 225–250.

Euler, T., Hausselt, S.E., Margolis, D.J., Breuninger, T., Castell, X., Detwiler, P.B., and Denk, W. (2009). Eyecup scope–optical recordings of light stimulus-evoked fluorescence signals in the retina. Pflugers Arch. *457*, 1393–1414. https://doi.org/10.1007/s00424-008-0603-5.

Fahey, P.G., Muhammad, T., Smith, C., Froudarakis, E., Cobos, E., Fu, J., Walker, E.Y., Yatsenko, D., Sinz, F.H., Reimer, J., et al. (2019). A global map of orientation tuning in mouse visual cortex. Preprint at bioRxiv. https://doi.org/10.1101/745323.

Fiser, A., and Sali, A. (2003). ModLoop: automated modeling of loops in protein structures. Bioinformatics *19*, 2500–2501. https://doi.org/10.1093/bioinformatics/btg362.

Franke, K., Berens, P., Schubert, T., Bethge, M., Euler, T., and Baden, T. (2017). Inhibition decorrelates visual feature representations in the inner retina. Nature *542*, 439–444. https://doi.org/10.1038/nature21394.

Franke, K., Maia Chagas, A., Zhao, Z., Zimmermann, M.J., Bartel, P., Qiu, Y., Szatko, K.P., Baden, T., and Euler, T. (2019). An arbitrary-spectrum spatial visual stimulator for vision research. eLife *8*, e48779. https://doi.org/10.7554/eLife.48779.

Ghasemi, A., and Zahediasl, S. (2012). Normality tests for statistical analysis: a guide for non-statisticians. Int. J. Endocrinol. Metab. *10*, 486–489. https://doi.org/10.5812/ijem.3505.

Grimes, W.N., Zhang, J., Graydon, C.W., Kachar, B., and Diamond, J.S. (2010). Retinal parallel processors: more than 100 independent microcircuits operate within a single interneuron. Neuron *65*, 873–885. https://doi.org/10.1016/j.neuron.2010.02.028.

Harris, K.D., Hirase, H., Leinekugel, X., Henze, D.A., and Buzsáki, G. (2001). Temporal interaction between single spikes and complex spike bursts in hippocampal pyramidal cells. Neuron *32*, 141–149. https://doi.org/10.1016/s0896-6273(01)00447-0.

Hausselt, S.E., Euler, T., Detwiler, P.B., and Denk, W. (2007). A dendrite-autonomous mechanism for direction selectivity in retinal starburst amacrine cells. PLoS Biol *5*, e185. https://doi.org/10.1371/journal.pbio.0050185.

Häusser, M., and Margrie, T.W. (2014). Two-photon targeted patching and electroporation in vivo. Cold Spring Harb. Protoc. *2014*, 78–85. https://doi.org/10.1101/pdb.prot080143.

Hedrick, T., and Waters, J. (2012). Effect of temperature on spiking patterns of neocortical layer 2/3 and layer 6 pyramidal neurons. Front. Neural Circuits *6*, 28. https://doi.org/10.3389/fncir.2012.00028.

Huber, D., Gutnisky, D.A., Peron, S., O'Connor, D.H., Wiegert, J.S., Tian, L., Oertner, T.G., Looger, L.L., and Svoboda, K. (2012). Multiple dynamic representations in the motor cortex during sensorimotor learning. Nature *484*, 473–478. https://doi.org/10.1038/nature11039.

Jercog, D., Roxin, A., Barthó, P., Luczak, A., Compte, A., and de la Rocha, J. (2017). Up-down cortical dynamics reflect state transitions in a bistable network. eLife *6*, e22425. https://doi.org/10.7554/eLife.22425.

Kannan, M., Vasan, G., Huang, C., Haziza, S., Li, J.Z., Inan, H., Schnitzer, M.J., and Pieribone, V.A. (2018). Fast, in vivo voltage imaging using a red fluorescent indicator. Nat. Methods *15*, 1108–1116. https://doi.org/10.1038/s41592-018-0188-7.

Kawaguchi, Y. (1995). Physiological subgroups of nonpyramidal cells with specific morphological characteristics in layer II/III of rat frontal cortex. J. Neurosci. *15*, 2638–2655.

Kim, B.B., Wu, H., Hao, Y.A., Pan, M., Chavarha, M., Zhao, Y., Westberg, M., St-Pierre, F., Wu, J.C., and Lin, M.Z. (2022). A red fluorescent protein with improved monomericity enables ratiometric voltage imaging with ASAP3. Sci. Rep. *12*, 3678. https://doi.org/10.1038/s41598-022-07313-1.

Lee, J., Liu, Z., Suzuki, P.H., Ahrens, J.F., Lai, S., Lu, X., Guan, S., and St-Pierre, F. (2020). Versatile phenotype-activated cell sorting. Sci. Adv. *6*, eabb7438. https://doi.org/10.1126/sciadv.abb7438.

Lim, S.T., Antonucci, D.E., Scannevin, R.H., and Trimmer, J.S. (2000). A novel targeting signal for proximal clustering of the Kv2.1 K+ channel in hippocampal neurons. Neuron *25*, 385–397. https://doi.org/10.1016/S0896-6273(00)80902-2.

Linkert, M., Rueden, C.T., Allan, C., Burel, J.M., Moore, W., Patterson, A., Loranger, B., Moore, J., Neves, C., Macdonald, D., et al. (2010). Metadata matters: access to image data in the real world. J. Cell Biol. *189*, 777–782. https://doi.org/10.1083/jcb.201004104.

Lundby, A., Akemann, W., and Knöpfel, T. (2010). Biophysical characterization of the fluorescent protein voltage probe VSFP2.3 based on the voltage-sensing domain of Ci-VSP. Eur. Biophys. J. *39*, 1625–1635. https://doi.org/10.1007/s00249-010-0620-0.

Madeira, F., Park, Y.M., Lee, J., Buso, N., Gur, T., Madhusoodanan, N., Basutkar, P., Tivey, A.R.N., Potter, S.C., Finn, R.D., and Lopez, R. (2019). The EMBL-EBI search and sequence analysis tools APIs in 2019. Nucleic Acids Res *47*, W636–W641. https://doi.org/10.1093/nar/gkz268.

Mauss, A.S., Vlasits, A., Borst, A., and Feller, M. (2017). Visual circuits for direction selectivity. Annu. Rev. Neurosci. *40*, 211–230. https://doi.org/10.1146/annurev-neuro-072116-031335.

McCormick, D.A., Connors, B.W., Lighthall, J.W., and Prince, D.A. (1985). Comparative electrophysiology of pyramidal and sparsely spiny stellate neurons of the neocortex. J. Neurophysiol. *54*, 782–806. https://doi.org/10.1152/jn.1985.54.4.782.

MICrONsConsortium, Bodor, A.L., Halageri, A., Sterling, A., Tolias, A.S., Ramos, A., Nehoran, B., Silverman, B., Celii, B., Smith, C.L., et al. (2021). Functional connectomics spanning multiple areas of mouse visual cortex. Preprint at bioRxiv. https://doi.org/10.1101/2021.07.28.454025.

Murata, Y., Iwasaki, H., Sasaki, M., Inaba, K., and Okamura, Y. (2005). Phosphoinositide phosphatase activity coupled to an intrinsic voltage sensor. Nature *435*, 1239–1243. https://doi.org/10.1038/nature03650.

Nasu, Y., Shen, Y., Kramer, L., and Campbell, R.E. (2021). Structure- and mechanism-guided design of single fluorescent protein-based biosensors. Nat. Chem. Biol. *17*, 509–518. https://doi.org/10.1038/s41589-020-00718-x.

Nikolaev, A., Zheng, L., Wardill, T.J., O'Kane, C.J., de Polavieja, G.G., and Juusola, M. (2009). Network adaptation improves temporal representation of naturalistic stimuli in Drosophila eye: II mechanisms. PLoS One *4*, e4306. https://doi.org/10.1371/journal.pone.0004306.

Nov, Y. (2012). When second best is good enough: another probabilistic look at saturation mutagenesis. Appl Environ Microbiol *78*, 258–262. https://doi.org/10.1128/AEM.06265-11.

Palovcak, E., Delemotte, L., Klein, M.L., and Carnevale, V. (2014). Evolutionary imprint of activation: the design principles of VSDs. J. Gen. Physiol. *143*, 145–156. https://doi.org/10.1085/jgp.201311103.

Patterson, G.H., and Lippincott-Schwartz, J. (2002). A photoactivatable GFP for selective photolabeling of proteins and cells. Science *297*, 1873–1877. https://doi.org/10.1126/science.1074952.

Peters, B.N., and Masland, R.H. (1996). Responses to light of starburst amacrine cells. J. Neurophysiol. *75*, 469–480.

Pettersen, E.F., Goddard, T.D., Huang, C.C., Couch, G.S., Greenblatt, D.M., Meng, E.C., and Ferrin, T.E. (2004). UCSF Chimera—a visualization system for exploratory research and analysis. J. Comput. Chem. *25*, 1605–1612. https://doi.org/10.1002/jcc.20084.

Pfeiffer, B.D., Ngo, T.T., Hibbard, K.L., Murphy, C., Jenett, A., Truman, J.W., and Rubin, G.M. (2010). Refinement of tools for targeted gene expression in Drosophila. Genetics *186*, 735–755. https://doi.org/10.1534/genetics.110.119917.

Piatkevich, K.D., Jung, E.E., Straub, C., Linghu, C., Park, D., Suk, H.J., Hochbaum, D.R., Goodwin, D., Pnevmatikakis, E., Pak, N., et al. (2018). A robotic multidimensional directed evolution approach applied to fluorescent voltage reporters. Nat. Chem. Biol. *14*, 352–360. https://doi.org/10.1038/s41589-018-0004-9.

Platisa, J., Vasan, G., Yang, A., and Pieribone, V.A. (2017). Directed evolution of key residues in fluorescent protein inverses the polarity of voltage sensitivity in the genetically encoded indicator arclight. ACS Chem. Neurosci. *8*, 513–523. https://doi.org/10.1021/acschemneuro.6b00234.

Pnevmatikakis, E.A., and Giovannucci, A. (2017). NoRMCorre: an online algorithm for piecewise rigid motion correction of calcium imaging data. J. Neurosci. Methods *291*, 83–94. https://doi.org/10.1016/j.jneumeth.2017.07.031.

Poulet, J.F.A., and Petersen, C.C.H. (2008). Internal brain state regulates membrane potential synchrony in barrel cortex of behaving mice. Nature *454*, 881–885. https://doi.org/10.1038/nature07150.

Reimer, J., Froudarakis, E., Cadwell, C.R., Yatsenko, D., Denfield, G.H., and Tolias, A.S. (2014). Pupil Fluctuations Track Fast Switching of Cortical States during Quiet Wakefulness. Neuron *84*, 355–362. https://doi.org/10.1016/j.neuron.2014.09.033.

Reimer, J., McGinley, M.J., Liu, Y., Rodenkirch, C., Wang, Q., McCormick, D.A., and Tolias, A.S. (2016). Pupil fluctuations track rapid changes in adrenergic and cholinergic activity in cortex. Nat Commun *7*, 13289. https://doi.org/10.1038/ncomms13289.

Rister, J., Pauls, D., Schnell, B., Ting, C.Y., Lee, C.H., Sinakevitch, I., Morante, J., Strausfeld, N.J., Ito, K., and Heisenberg, M. (2007). Dissection of the peripheral motion channel in the visual system of Drosophila melanogaster. Neuron *56*, 155–170. https://doi.org/10.1016/j.neuron.2007.09.014.

Stern, E.A., Kincaid, A.E., and Wilson, C.J. (1997). Spontaneous subthreshold membrane potential fluctuations and action potential variability of rat corticostriatal and striatal neurons in vivo. J. Neurophysiol. *77*, 1697–1715. https://doi.org/10.1152/jn.1997.77.4.1697.

St-Pierre, F., Chavarha, M., and Lin, M.Z. (2015). Designs and sensing mechanisms of genetically encoded fluorescent voltage indicators. Curr. Opin. Chem. Biol. *27*, 31–38. https://doi.org/10.1016/j.cbpa.2015.05.003.

St-Pierre, F., Marshall, J.D., Yang, Y., Gong, Y., Schnitzer, M.J., and Lin, M.Z. (2014). High-fidelity optical reporting of neuronal electrical activity with an ultrafast fluorescent voltage sensor. Nat. Neurosci. *17*, 884–889. https://doi.org/10.1038/nn.3709.

Tsutsui, H., Jinno, Y., Tomita, A., and Okamura, Y. (2014). Rapid evaluation of a protein-based voltage probe using a field-induced membrane potential change. Biochim. Biophys. Acta *1838*, 1730–1737. https://doi.org/10.1016/j.bbamem.2014.03.002.

Tukker, J.J., Taylor, W.R., and Smith, R.G. (2004). Direction selectivity in a model of the starburst amacrine cell. Vis. Neurosci. *21*, 611–625. https://doi.org/10.1017/S0952523804214109.

van Rosmalen, M., Krom, M., and Merkx, M. (2017). Tuning the flexibility of glycine-serine linkers to allow rational design of multidomain proteins. Biochemistry *56*, 6565–6574. https://doi.org/10.1021/acs.biochem.7b00902.

Villette, V., Chavarha, M., Dimov, I.K., Bradley, J., Pradhan, L., Mathieu, B., Evans, S.W., Chamberland, S., Shi, D., Yang, R., et al. (2019). Ultrafast two-photon imaging of a high-gain voltage indicator in awake behaving mice. Cell *179*, 1590–1608.e23. https://doi.org/10.1016/j.cell.2019.11.004.

Villette, V., Levesque, M., Miled, A., Gosselin, B., and Topolnik, L. (2017). Simple platform for chronic imaging of hippocampal activity during spontaneous behaviour in an awake mouse. Sci. Rep. *7*, 43388. https://doi.org/10.1038/srep43388.

Vlasits, A.L., Bos, R., Morrie, R.D., Fortuny, C., Flannery, J.G., Feller, M.B., and Rivlin-Etzion, M. (2014). Visual stimulation switches the polarity of excitatory input to starburst amacrine cells. Neuron *83*, 1172–1184. https://doi.org/10.1016/j.neuron.2014.07.037.

Vlasits, A.L., Morrie, R.D., Tran-Van-Minh, A., Bleckert, A., Gainer, C.F., DiGregorio, D.A., and Feller, M.B. (2016). A role for synaptic input distribution in a dendritic computation of motion direction in the retina. Neuron *89*, 1317–1330. https://doi.org/10.1016/j.neuron.2016.02.020.

Wang, B., Ke, W., Guang, J., Chen, G., Yin, L., Deng, S., He, Q., Liu, Y., He, T., Zheng, R., et al. (2016). Firing frequency maxima of fast-spiking neurons in human, monkey, and mouse neocortex. Front. Cell. Neurosci. *10*, 239. https://doi.org/10.3389/fncel.2016.00239.

Waterhouse, A., Bertoni, M., Bienert, S., Studer, G., Tauriello, G., Gumienny, R., Heer, F.T., de Beer, T.A.P., Rempfer, C., Bordoli, L., et al. (2018). SWISS-MODEL: homology modelling of protein structures and complexes. Nucleic Acids Res *46*, W296–W303. https://doi.org/10.1093/nar/gky427.

Wei, W. (2018). Neural mechanisms of motion processing in the mammalian retina. Annu. Rev. Vis. Sci. *4*, 165–192. https://doi.org/10.1146/annurev-vision-091517-034048.

Wilson, R.I., Turner, G.C., and Laurent, G. (2004). Transformation of olfactory representations in the Drosophila antennal lobe. Science *303*, 366–370. https://doi.org/10.1126/science.1090782.

Wilt, B.A., Fitzgerald, J.E., and Schnitzer, M.J. (2013). Photon shot noise limits on optical detection of neuronal spikes and estimation of spike timing. Biophys. J. *104*, 51–62. https://doi.org/10.1016/j.bpj.2012.07.058.

Wu, J., Liang, Y., Chen, S., Hsu, C.L., Chavarha, M., Evans, S.W., Shi, D., Lin, M.Z., Tsia, K.K., and Ji, N. (2020). Kilohertz two-photon fluorescence microscopy imaging of neural activity in vivo. Nat. Methods *17*, 287–290. https://doi.org/10.1038/s41592-020-0762-7.

Yang, H.H., and St-Pierre, F. (2016). Genetically encoded voltage indicators: opportunities and challenges. J. Neurosci. *36*, 9977–9989. https://doi.org/10.1523/JNEUROSCI.1095-16.2016.

Yang, H.H., St-Pierre, F., Sun, X., Ding, X., Lin, M.Z., and Clandinin, T.R. (2016). Subcellular imaging of voltage and calcium signals reveals neural processing in vivo. Cell *166*, 245–257. https://doi.org/10.1016/j.cell.2016.05.031.

Yang, J., Yan, R., Roy, A., Xu, D., Poisson, J., and Zhang, Y. (2015). The I-TASSER Suite: protein structure and function prediction. Nat. Methods *12*, 7–8. https://doi.org/10.1038/nmeth.3213.

Yoshimatsu, T., Bartel, P., Schröder, C., Janiak, F.K., St-Pierre, F., Berens, P., and Baden, T. (2021). Ancestral circuits for vertebrate color vision emerge at the first retinal synapse. Sci. Adv. *7*, eabj6815. https://doi.org/10.1126/sciadv.abj6815.

Zhang, D.Y., Lau, C.P., and Li, G.R. (2009). Human Kir2.1 channel carries a transient outward potassium current with inward rectification. Pflugers Arch *457*, 1275–1285. https://doi.org/10.1007/s00424-008-0608-0.

Zou, P., Zhao, Y., Douglass, A.D., Hochbaum, D.R., Brinks, D., Werley, C.A., Harrison, D.J., Campbell, R.E., and Cohen, A.E. (2014). Bright and fast multicoloured voltage reporters via electrochromic FRET. Nat. Commun. *5*, 4625. https://doi.org/10.1038/ncomms5625.

STAR★METHODS

KEY RESOURCES TABLE

REAGENT or RESOURCE	SOURCE	IDENTIFIER
Bacterial and virus strains		
XL10-Gold Ultracompetent Cells	Agilent	Cat #200315
AAV2/1-EF1α-DIO-JEDI-2P	This paper	N/A
AAV2/1-EF1α-DIO-JEDI-2P-Kv	This paper	N/A
AAV1.hSyn.Cre	This paper	N/A
Deposited data		
JEDI-2P	This paper	GenBank: OL542830
Experimental models: Cell lines		
HEK293-Kir2.1	Zhang et al., 2009	N/A
HEK293A	Thermo Fisher Scientific	Cat #R705-07; RRID: CVCL_6910
Experimental models: Organisms/strains		
Drosophila melanogaster		
+; +; 21D-Gal4/TM6B (L2 Gal4)	Rister et al., 2007	N/A
w; UAS-ASAP2f{attP40}; +	Yang et al., 2016	RRID: BDSC_65414
w; UAS-ASAP3{attP40}; +	This paper	N/A
yw; UAS-JEDI-2P{attP40}; +	This paper	N/A
w; +; UAS-jRGECO1b{VK00005}	Dana et al., 2016	RRID: BDSC_65414
L2>>ASAP2f: +; UAS-ASAP2f/+; 21D-Gal4/+	This paper	N/A
L2>>JEDI-2P: yw/+; UAS-JEDI-2P/+; 21D-Gal4/+	This paper	N/A
L2>>ASAP2f: +; UAS-ASAP2f/+; 21D-Gal4, jRGECO1b/+	This paper	N/A
L2>>ASAP3: w/+; UAS-ASAP3/+; 21D-Gal4, jRGECO1b/+	This paper	N/A
Mus musculus		
B6;129S6-*Chat*$^{tm2(cre)Lowl}$/J	The Jackson Laboratory	RRID: IMSR_JAX:006410
B6;129S-*Slc17a7*$^{tm1.1(cre)Hze}$/J mice	The Jackson Laboratory	RRID: IMSR_JAX:023527
C57BL/6J (wild-type) mouse	Charles River	Cat #632C57BL/6J; RRID: IMSR_JAX:000664
Recombinant DNA		
pcDNA3.1/Puro-CAG-JEDI-2P	This paper	RRID: Addgene_179458
pcDNA3.1/Puro-CAG-ASAP2s	Chamberland et al., 2017	RRID: Addgene_101274
pcDNA3.1/Puro-CAG-ASAP3	Villette et al., 2019	N/A
pcDNA3.1/Puro-CAG-EGFP	This paper	N/A
pcDNA3.1/Puro-CAG-EGFP-CAAX	This paper	N/A
pcDNA3.1/Puro-CAG-JEDI-2P-GSS×3-cyOFP1	This paper	N/A
pcDNA3.1/Puro-CAG-ASAP1-GSS×3-cyOFP1	This paper	N/A
pcDNA3.1/Puro-CAG-ASAP2s-GSS×3-cyOFP1	This paper	N/A
pcDNA3.1/Puro-CAG-ASAP3-GSS×3-cyOFP1	This paper	N/A
pcDNA3.1/Puro-CAG-ASAP1-EGFP-GSS×3-cyOFP1	This paper	N/A
pcDNA3.1/Puro-CAG-ASAP2s-H152E-GSS×3-cyOFP1	This paper	N/A
pcDNA3.1/Puro-CAG-ASAP2s-T207H-GSS×3-cyOFP1	This paper	N/A
pAAV-hSyn-JEDI-2P-WPRE	This paper	RRID: Addgene_179464
pAAV-EF1a-DIO-JEDI-2P-WPRE	This paper	RRID: Addgene_179460
pAAV-EF1a-DIO-JEDI-2P-GSS×3-Kv-WPRE	This paper	RRID: Addgene_179459
pJFRC7-20XUAS-JEDI-2P	This paper	RRID: Addgene_179461
pJFRC7-20XUAS-ASAP3	This paper	N/A

(*Continued on next page*)

Continued

REAGENT or RESOURCE	SOURCE	IDENTIFIER
Software and algorithms		
NIS-Elements HC 4.60	Nikon Instruments	RRID: SCR_014329
LabVIEW NXG 5.0	National Instruments	RRID: SCR_014325
pClamp 11	Molecular Devices	RRID: SCR_011323
MATLAB R2019b (9.7)	MathWorks	RRID: SCR_001622
Wolfram Mathematica 13.0	Wolfram	RRID: SCR_014448
GraphPad Prism 9	GraphPad	RRID: SCR_002798
MLSpike	Deneux et al., 2016	MLspike
Volpy	Cai et al., 2021	Volpy

RESOURCE AVAILABILITY

Lead contact

Further information and requests for resources and reagents should be directed to and will be fulfilled by the lead contact, Prof. François St-Pierre (stpierre@bcm.edu or stpierre@alum.mit.edu).

Materials availability

The JEDI-2P sequence is available from GenBank (GenBank: OL542830). All JEDI-2P plasmids, AAV packaging vectors, and the plasmid used to make the transgenic JEDI-2P flies are available from Addgene (see key resources table).

Data and code availability

All data reported in this paper will be shared by the lead contact upon request. This paper does not report original code needed to reanalyze the data generated by this study. Any additional information required to reanalyze the data reported in this paper is available from the lead contact upon request.

EXPERIMENTAL MODEL AND SUBJECT DETAILS

Cell lines

HEK293A and HEK293-Kir2.1 cell lines (sex: female in both cases) were used in this study. Detailed growth conditions varied with the experiment and are reported in the method details section. These cell lines were free of mycoplasma contamination and were authenticated by STR profiling by the Cytogenetics and Cell Authentication core (MD Anderson).

Fly experiments

All flies used for imaging were raised on standard molasses food at 25°C on a 12/12-h light-dark cycle. Female flies of the appropriate genotypes were collected on CO_2 within 1 day of eclosion and imaged at room temperature (20°C) 6-8 days after eclosion.

The genotypes of the imaged flies in Figure 4 were:
L2>>ASAP2f: +; UAS-ASAP2f/+; 21D-Gal4/+
L2>>JEDI-2P: yw/+; UAS-JEDI-2P/+; 21D-Gal4/+
The genotypes of the imaged flies in Figure S5 were:
L2>>ASAP2f: +; UAS-ASAP2f/+; 21D-Gal4, jRGECO1b/+
L2>>ASAP3: w/+; UAS-ASAP3/+; 21D-Gal4, jRGECO1b/+

Retinal explants

Retinal explants were extracted from healthy 2-month-old *Chat-cre+* female mice of strain B6;129S6-*Chat*$^{tm2(cre)Lowl}$/J (RRID: IMSR_JAX:006410). Based on previous studies, we do not expect that gender would impact sensor expression or light responses in retinal explants. No previous procedures were performed prior to those described in the method details. Animals were group housed.

Mice experiments with resonant scanning microscopy

3 males and 1 female mice from 2-6 months (at the time of imaging) were used for these experiments. Same sex littermates were housed together in individual cages with 1-4 mice per cage. Mice were maintained on a regular diurnal lighting cycle (12:12 light:dark) with *ad libitum* access to food and water and nesting material for environmental enrichment. Mice were housed in the Taub Mouse Facility of Baylor College of Medicine, accredited by AAALAC (The Association for Assessment and Accreditation of Laboratory Animal Care International). The animals used for this experiment were healthy and not involved in any previous procedures or experiments.

Mice experiments with ULoVE microscopy

5 male wild-type C57BL/6J mice were housed in standard conditions (12-hour light/dark cycles, light on at 7 a.m., with water and food *ad libitum*). No previous procedures were performed prior to those described in the method details. Mice were housed one per cage after surgery.

METHOD DETAILS

Reagents for screening and *in vitro* benchmarking

Basic chemical reagents include: NaCl (S3014, Sigma-Aldrich), sucrose (S0389, Sigma-Aldrich), glucose (G8270, Sigma-Aldrich), HEPES (H3375, Sigma-Aldrich), KCl (P9541, Sigma-Aldrich), $MgSO_4$ (M2643, Sigma-Aldrich), K-gluconate (P1847, Sigma-Aldrich), EGTA (E3889, Sigma-Aldrich), $MgCl_2$ (M9272, Sigma-Aldrich), $CaCl_2$ (223506, Sigma-Aldrich), KOH (P250, Thermo Fisher) and NaOH (S5881, Sigma-Aldrich).

Cell culture reagents include: high-glucose Dulbecco's Modified Eagle Medium (D1145, Sigma-Aldrich), fetal bovine serum (F2442, Sigma-Aldrich), glutamine (G7513, Sigma-Aldrich), Penicillin/Streptomycin (P4333, Sigma-Aldrich), Geneticin (G418) Sulfate (30-234-CR, Corning), 30-70 kD poly-D-lysine (P7886, Sigma-Aldrich), 300 kD poly-D-lysine hydrobromide (P7405, Sigma-Aldrich) and phosphate-buffered saline (PBS, SH302560, HyClone, GE Healthcare).

Primary neuronal culture reagents include: phenol-red-free Neurobasal medium (12348017, Gibco), B-27 (17504044, Gibco), Glutamax (35050061, Gibco) and cytosine β-D-arabinofuranoside (C1768, Sigma-Aldrich).

Transfection and cloning reagents include: jetPRIME (114-15, Polyplus Transfection), FuGENE HD transfection reagent (E2311, Promega), lipofectamine 2000 (11668019, Thermo Fisher Scientific), FastDigest NheI (FD0974, Thermo Fisher Scientific) and FastDigest HindIII (FD0504, Thermo Fisher Scientific).

High-throughput GEVI screening

Plasmid construction

Plasmids were assembled by standard molecular biology techniques and all cloned constructs were confirmed by Sanger sequencing (Eurofins Genomics LLC). GEVIs were cloned in pcDNA3.1/Puro-CAG vector. Unless noted otherwise, the reference protein cyOFP1 was fused to the C-terminus of GEVIs via a GSSGSSGSS linker (van Rosmalen et al., 2017) (Figure 1J). ASAP1 and ASAP2s were subcloned from plasmids RRID: Addgene_52519 and RRID: Addgene_101274, respectively. ASAP3 was subcloned from a plasmid kindly provided by Dr. Michael Lin (Stanford). ASAP1-EGFP was cloned by replacing the circularly permuted GFP in ASAP1 (cpsfGFP-OPT) with EGFP (V2 – K239 (Chamberland et al., 2017)).

Library construction

Site-directed polymerase chain reaction (PCR) mutagenesis was used to construct saturation mutagenesis libraries, each targeting a single residue. Using single primers with the degenerate codon NNK results in the overrepresentation of some amino acids. To obtain a more uniform distribution of residues, we combined primers containing the NNT, VAA, ATG, or TGG codon (N = any base; V = A, G, or C) at a molar ratio of 16:3:1:1, respectively. The 20 μL PCR reaction mix contained 1 μL forward primer mix at 20 μM, 1 μL reverse primer at 20 μM, 50 ng template plasmid, and 10 μL 2× PCR master premix (PrimeSTAR HS DNA polymerase, Takara). DNA was amplified using the following protocol: an initial denaturation step at 98°C for 30 s; 35 amplification cycles of 98°C for 10 s, 57°C for 10 s, 72°C for 1 min/kb of fragment length; a final extension step at 72°C for 5 min. The pcDNA3.1/Puro-CAG backbone was linearized using the restriction enzymes NheI and HindIII. PCR products and linearized backbones were purified using gel electrophoresis and GeneJET Gel Extraction Kit (Thermo Fisher Scientific). PCR products were assembled in the vector backbone using the In-Fusion assembly system (In-fusion HD Cloning Plus, Takara) according to the manufacturer's instructions. The In-Fusion reaction mix was transformed into commercial chemically competent bacteria (XL10-Gold, Agilent) with a transformation efficiency exceeding 5×10^9 CFU per μg DNA. Liquid cultures were inoculated with manually picked colonies, and purified plasmids were prepared using a 96-well plasmid purification kit (PureLink Pro, Thermo Fisher Scientific) following the manufacturer's instructions.

Cell culture and transfection in 96-well plates

We used a modified HEK293 cell line that stably expressed human Kir2.1 channel (Zhang et al., 2009) to maintain a resting membrane potential at approximately −77 mV in our conditions. HEK293-Kir2.1 cells were cultured at 37°C with 5% CO_2 in growth medium #1, which contained high-glucose Dulbecco's Modified Eagle Medium supplemented with 10% fetal bovine serum (FBS), 2 mM glutamine, 100 unit/mL Penicillin, 100 μg/mL Streptomycin, and 750 μg/mL of the antibiotic G418 Sulfate (geneticin). G418 was added to maintain the expression of the Kir2.1 transgene, which was chromosomally integrated together with a G418 resistance gene.

For screening GEVIs, glass-bottom 96-well plates (P96-1.5H-N, Cellvis) were first coated with 30-70 kD poly-D-lysine to promote cell adherence to the glass. Coating was done for 1 h at 37°C and plates washed twice with PBS. HEK293-Kir2.1 cells were then plated to 60-80% confluency in growth medium #2, which contained high-glucose Dulbecco's Modified Eagle Medium supplemented with 5% FBS, 2 mM glutamine, 100 unit/mL Penicillin, and 100 μg/mL Streptomycin.

We generally selected 48 variants per library. According to a statistical model, our library generation and sampling strategy produced a ~91% theoretical probability that any given library included the best residue (Nov, 2012). Each well was transfected according to the jetPRIME protocol: we used a mixture of 130 ng DNA, 0.4 μL jetPRIME transfection reagent, and 20 μL jetPRIME buffer in 150 μL of growth medium #2. Independent transfections were defined as transfections of separate wells in which DNA was added

separately. Twenty-four hours post-transfection, 120 μL of the medium in each well was replaced with fresh growth medium #2 to minimize potential cytotoxicity from the transfection reagents. Forty-eight hours post-transfection the cells were washed twice with 200 μL of imaging solution (110 mM NaCl, 26 mM sucrose, 23 mM glucose, 5 mM HEPES, 5 mM KCl, 2.5 mM $CaCl_2$, 1.3 mM $MgSO_4$, adjusted to pH 7.4 with NaOH) at room temperature. Wells were filled with 100 μL of the imaging solution and screened with our 2PM high-throughput screening platform.

Two-photon screening system

An inverted microscope with multi-photon capability (A1R-MP, Nikon Instruments) was used for two-photon screening and *in vitro* characterization of GEVIs. The two-photon excitation light was generated by a titanium:sapphire femtosecond laser (Chameleon Ultra II, Coherent) with a repetition rate of 80 MHz and a tuning range between 680 nm and 1,080 nm. Laser power was tuned using an acousto-optic modulator and delivered to the sample plane through a 20× 0.75-NA objective (CFI Plan Apochromat Lambda, Nikon Instruments). The emission light from the sample was split using a 560-nm dichroic mirror and filtered by 525/50-nm (center wavelength/bandwidth) and 605/70-nm filters (Nikon Instruments) for green and red channels, respectively. Emitted photons were detected by gallium arsenide phosphide (GaAsP) photomultipliers tubes (PMTs). A motorized extended travel stage (H139E1, Prior) was used to control the position of the field of view and to hold 96-well plates and the electrophysiology perfusion chamber.

To support automation of the system, data acquisition and output broads (PCI-6229 and PCI-6723, National Instruments) were connected to the microscope computer through a PXI Chassis (PXI-1033, National Instruments). The computer was equipped with 2 Intel Xeon E5-2630 v3 processors (total of 16 cores), 128 GB of DDR4 RAM, and four 2 TB SSDs in RAID 0 to facilitate high-speed imaging. JOBs scripts in NIS-Elements HC (version 4.60, Nikon Instruments) were used to control the microscope system (e.g., stage position), manage the optical configurations (e.g., excitations), initiate image acquisition, and trigger the stimulator.

A digital isolated high-power stimulator (4100, A-M System) was used to provide electric field stimulation. Electric pulses were passed to a pair of electrodes made from 0.5 mm wide platinum wires (99.95% pure, AA10286BU, Fisher Scientific). The two L-shaped electrodes had a horizontal length of 2 mm and were 3 mm apart, and they were secured on a 3D-printed polylactic acid holder (Figure 1F). The holder was fixed to a motorized linear translation stage (MTS50-Z8, Thorlabs), which was used to move the electrodes in and out of individual wells. Two smaller manual linear translation stages (411-05S, Newport) were used to fine-tune the electrodes' lateral position (Figure 1E). During stimulation, the electrodes were submerged under the imaging solution, about 350 μm above the bottom (i.e., 600 μm if calculated from the center of the electrode) (Figures S1B and S1D). The design was validated using 3D finite element modeling using Mathematica (Wolfram, Figure S1D).

Two-photon GEVI screening

Four non-overlapping fields of view (FOV) of 512 × 32 pixels were imaged per well at 440 Hz using a resonant galvanometer scanner. The laser was set to 920 nm and tuned to 34-50 mW at the sample plane. The reference orange/red FP cyOFP1 was imaged first. 50 frames were captured so that noise could be reduced by averaging. Electric field stimulation was performed during continuous imaging of the green channel for 4000 frames or ~9 s. The stimulation protocol started with twenty monophasic square pulses with 1-ms width, 60-V amplitude, and an inter-pulse duration of 300-ms. This was followed by a 100-Hz train (10 monophasic square pulses with 2.5-ms width, 30-V amplitude, and an inter-pulse duration of 10 ms), although responses to this train were not used as a performance metric in the experiments described here.

Analysis of high-throughput screening data

Image analyses were performed by custom routines in MATLAB (version r2019b, MathWorks). Time-lapse images recorded in nd2 format were imported to MATLAB using the Bio-Formats toolbox (version 6.3.1) (Linkert et al., 2010). For each channel (red and green) of each FOV, saturated pixels (e.g., from over-expressing cells) were removed and images were background corrected. An initial foreground mask was computed from the first 20 frames of each channel by applying pre-defined intensity thresholds to distinguish GEVI fluorescence from autofluorescence. The mask was applied to each image of the corresponding channel. The values of all pixels of an FOV were summated to obtain the overall change in fluorescence over time. We noticed that the quantification of response amplitudes could be distorted by overexpressing cells, bright extracellular fluorescent puncta, and intracellular aggregates due to slight impairment of GEVI plasma membrane targeting caused by the fused cyOFP. These problematic pixels were removed by discarding non-responsive pixels. To do this, we first corrected the green (GEVI) fluorescence obtained above for photobleaching. We performed a three-term exponential fitting on the mean fluorescence using data outside stimulation durations. The time constants were then used to estimate the trend for each pixel using the least-squares fitting. The trend of each pixel was removed using division. Correlation scores were then computed between the fluorescence of each foreground pixel and the overall FOV-level photobleaching-corrected fluorescence time course. The foreground pixels were then ordered by their correlation scores and binned in batches of 200 pixels. The foreground mask of responsive pixels was obtained by adding pixel bins of decreasing correlation scores until we maximized the signal-to-noise ratio. As done with the original threshold-based mask, all pixels were summated to obtain a single time course per FOV. To quantify photobleaching, this time course was normalized by the fluorescence at t = 0 and the area under the curve was quantified (Figure 1K). To measure responsivity, the unnormalized trace was corrected for photobleaching, using the same method motioned above, the responses to the 20 electrical field stimulations were averaged, and the peak response amplitude was quantified. GEVI brightness was calculated using the averaged fluorescence intensity of the first 20 frames in the green channel normalized by the average fluorescence intensity of the first 20 frames in the red channel. Normalization using the red channel was performed to correct for FOV-to-FOV differences in the number of transfected cells, the number of selected pixels, and overall expression (e.g., due to pipetting errors or biological variation).

We developed compound metrics to simplify the ranking of indicators while considering multiple performance criteria. A theoretical framework suggested $d' = R\sqrt{B\tau_{OFF}}$ — where R is the response amplitude, B is the brightness, and τ_{OFF} is the off-kinetics time constant — as a valuable metric to evaluate an indicator's ability to detect isolated spikes (Wilt et al., 2013). However, while slower off-kinetics increase the d', they also impair the identification of individual APs within a burst or fast spike train. We, therefore, decided to consider off-kinetics separately and defined the detectability index $D_I = R\sqrt{B}$ by removing τ_{OFF} from the d' equation. We also sought to consider the impact of photobleaching on voltage recording and avoid variants that are bright but bleach rapidly. We thus evaluated indicators based on both D_I and photostability, and confirmed that three published ASAP variants could be distinguished using these metrics (Figure 1L). We also created a new metric — the detectability budget ($D_B = R\sqrt{\overline{B}} = R\sqrt{BP}$) — that combines all measured performance characteristics by replacing the initial brightness in the D_I equation with the average brightness measured during the screening experiment.

ASAP2s *in silico* structure prediction

To build the ASAP2s structure (Figures 1O and S2A), the structures of the voltage-sensing and the cpGFP domains were first predicted using I-TASSER (Yang et al., 2015) and SWISS-MODEL (Waterhouse et al., 2018), respectively. The two domains were then fused in UCSF Chimera (Pettersen et al., 2004). ModLoop (Fiser and Sali, 2003) was used to optimize the interface between the voltage-sensing domain and the cpGFP.

GEVI characterization *in vitro*

Preparation for voltage clamp

HEK293A cells (Thermo Fisher Scientific) were plated on 30-70 kD poly-D-lysine-coated circular cover glass (12 mm #0, 633009, Carolina) at 30% confluence in growth medium #2, two days before imaging. Chemical transfection was done on the same day of plating using 200 ng DNA and 0.6 μL FuGENE HD transfection reagent per well of a 24-well plate (P24-1.5H-N, Cellvis) following manufacturer's instructions. The cells were cultured at 37°C with 5% CO_2 before and after transfection. Twenty-four hours post transfection, the transfection media was replaced with fresh growth medium #2 to minimize potential cytotoxicity from the transfection reagent.

Glass micropipettes (TW150-4 or 1B150-F-4, World Precision Instruments) were prepared using a pipette puller (P-87 or P1000, Sutter) to achieve a tip resistance of 2-6 MΩ. Micropipettes were loaded with internal solution composed of 115 mM K-gluconate, 10 mM HEPES, 10 mM EGTA, 10 mM glucose, 8 mM KCl, 5 mM $MgCl_2$, 1 mM $CaCl_2$, adjusted to pH 7.4 with KOH. The micropipette was installed on a patch-clamp head-stage (CV-7B, Molecular Devices) and positioned by a micromanipulator (SMX series, Sensapex). The coverslip seeded with the transfected cells was placed in a custom glass-bottom chamber based on Chamlide EC (Live Cell Instrument) with glass bottom made with a 24 × 24 mm #1 coverslip, (D102424, Deltalab). Cells were continuously perfused with external solution (110 mM NaCl, 26 mM sucrose, 23 mM glucose, 5 mM HEPES, 5 mM KCl, 2.5 mM $CaCl_2$, 1.3 mM $MgSO_4$, titrated to pH 7.4 with NaOH, same as the imaging solution in High-throughput GEVI screening section) at ~ 4 mL/min with a peristaltic pump (505DU, Watson Marlow). Whole-cell voltage clamp was achieved using a MultiClamp 700B amplifier (Molecular Devices). Patch clamp data was recorded with an Axon Digidata 1550B1 Low Noise system with HumSilencer (Molecular Devices). Command voltage waveforms were compensated for the liquid junction potential. Recordings were considered satisfactory and were included in the final analysis only if the patched cell had an access resistance (Ra) smaller than 7 MΩ and a membrane resistance (Rm) larger than 10 times of Ra both before and after the recording.

Voltage clamp under one-photon illumination

GEVI characterization under 1PM was performed with the same microscope as for GEVI screening (above). Cells were illuminated with 470/24-nm light (SpectraX, Lumencor) and conditioned using the 477-503-nm band of a multi-band dichroic mirror (89100bs, Chroma). The irradiance at the sample plane was 4-8 mW/mm^2. Green emitted photons were reflected towards the camera or PMT using the 503-542-nm band of the multi-pass dichroic (above) and filtered at 509-532 nm using a multi-pass filter (89101m, Chroma).

Electrophysiological recordings were done at room temperature (~22°C), and cells were held at –70 mV, unless otherwise noted. Each patched cell expressing a GEVI variant was recorded using only one of the three voltage-clamp protocols. To predict GEVIs' responses to action potentials (APs) under controlled conditions, we clamped HEK293 cells to follow a typical AP waveform and the resulting changes in GEVI fluorescence were monitored. The overall AP waveform had been recorded from a representative hippocampal neuron and was modified to have an amplitude of 100 mV and a full width at half maximum of 2 ms to mimic the shape of layer 2/3 cortical neurons at room temperature (Hedrick and Waters, 2012). We performed experiments at room temperature because spikes are shorter at 37°C (0.7-0.8 ms, (Hedrick and Waters, 2012; Kawaguchi, 1995; McCormick et al., 1985)) and are thus suboptimally sampled with our imaging rate (1 kHz maximum under 1PM and 440 Hz under 2PM). Since GEVIs' response time constants decrease with temperature at about the same rate as the decrease in spike width, GEVI responses are often tested at room temperature *in vitro* (Chamberland et al., 2017; Kannan et al., 2018; Villette et al., 2019; Zou et al., 2014). Cells were stimulated with 5 AP waveforms at 2 Hz and 10 AP waveforms at 100 Hz. The excitation light was focused on the sample using a 20× NA-0.75 objective (CFI Plan Apochromat Lambda, Nikon Instruments). Time series recordings were captured at 1 kHz using the fast scan mode of a scientific complementary metal-oxide-semiconductor (sCMOS) camera (ORCA Flash 4.0 V2, Hamamatsu). Images were captured from a FOV with 2048 columns and 200 rows, which were binned by the camera after pixel readout, thus producing images of 512 × 50 pixels.

To characterize fluorescence changes at or near steady state, cells were submitted to 1-s voltage steps to −100, −80, −60, −40, −20, 0, 20, 30, and 50 mV, with 1.5 s at the holding potential (−70 mV) between steps. Fluorescence was captured using the same optical configuration and imaging protocol as in the previous paragraph. Traces (e.g., in Figure 2A) were smoothed by a 24-ms moving average.

To evaluate the sensors' kinetics, we conducted three 1-s 100-mV depolarization pulses from −70 to 30 mV. Between each pulse, cells were held at –70 mV for 1.4 s. Recordings were performed at 21-23°C (room temperature) or 32-35°C (closer to the 37°C temperature of mice brains) using a feedback-controlled inline heater system (inline heater SH-27B, controller TC-324C, cable with thermistor TA-29, Warner instruments) to maintain the temperature in the perfusion chamber. A diaphragm was used to reduce the diameter of the excitation spot so that during imaging only one cell at the center of the FOV was illuminated. To maximize photon collection, we used an objective with higher numerical aperture (NA) than above (40× NA-0.95, CFI Plan Fluor oil immersion, Nikon Instruments). To capture fluorescence changes at higher temporal resolution than achievable with our camera, a multialkali photomultiplier tube (PMT, PMM02, Thorlabs) was installed on one of the side ports of the microscope. A LabVIEW (version NXG 5.0, National Instruments) routine was used to control the PMT bias voltage and record the output voltage using the data acquisition and output boards. Data were collected at 80 kHz. The output voltage from the PMT was analyzed by a custom routine written in MATLAB to obtain fluorescence signal for each cell. The raw data was first downsampled to 20 kHz. Then, photobleaching correction was done by performing a three-term exponential fitting on the baseline (when the cell was held at −70 mV) and removing the trend from the entire signal using division. The corrected signal was cropped from 0.1-s before the estimated depolarization or the repolarization onset to 1-s after the estimated depolarization or repolarization onset. The exact onset timing was fitted together with other coefficients with either single-exponential ($F(t) = c + (k \times \exp((t - t_0) \times \lambda)) \times (t > t_0) + k \times (t \leq t0)$) or dual-exponential ($F(t) = c + (k \times \exp((t - t_0) \times \lambda) + k_2 \times \exp((t - t_0) \times \lambda_2)) \times (t > t_0) + (k + k_2) \times (t \leq t_0)$) model where the t is the independent variable, F is the dependent variable, and the rest are the coefficients to be fitted. Among these coefficients, c describes the mean plateau fluorescence, k or k_2 describe the relative ratio of each exponential component, λ or λ_2 describe (minus) inverse of the time constant(s), and t_0 is an offset indicating the exact event onset timing.

Voltage clamp under two-photon illumination

To evaluate sensors' performance under 2PM, we used one integrated protocol to characterize the fluorescence changes in response to AP waveforms and step voltages at ∼22°C. The same AP waveforms that were used under 1PM were used under 2PM, and each cell was stimulated with 20 AP waveforms at 2 Hz and 10 AP waveforms at 100 Hz, and then held for 1 s at −100, −80, −60, −40, −20, 0, 20, 30, and 50 mV from a holding potential of –70 mV. AP waveforms were as described above (1PM characterization). We used a ≥ 2-s interval before the AP waveform assay and the voltage steps and 1.5-s intervals between each voltage step. These intervals ensured that GEVI fluorescence had returned to its resting state. Cells were imaged using the same inverted microscope as 2P screening, under 40× magnification (NA-0.95, CFI Plan Fluor oil immersion, Nikon Instruments). The resonant galvanometer scanner was used to direct the 920-nm excitation laser at 15% of the full power or 31 mW at the sample plane with the detector photomultiplier tubes' gain set to 20. Videos were taken with a resolution of 512 × 32 pixels and a frame rate of 440 Hz.

Two-photon excitation spectra

To determine the two-photon excitation spectrum for JEDI-2P, we cloned JEDI-2P, ASAP2s and EGFP in pcDNA3.1/Puro-CAG plasmid between the NheI and HindIII sites with no reference protein attached. ASAP2s and EGFP were used as controls in this experiment. These constructs were then transfected into HEK293-Kir2.1 cells using jetPRIME. The cells were plated in wells of a 24-well plate (P24-1.5H-N, Cellvis) coated with 30-70 kD poly-D-lysine. Each well was transfected according to the jetPRIME protocol with a mixture of 650 ng DNA, 1.8 μL jetPRIME transfection reagent, and 65 μL jetPRIME buffer in 500 μL of culture medium. Independent transfections were defined as transfections of separate wells in which DNA was added separately. Four hours after transfection, the transfection media was replaced with fresh growth medium #2 to minimize the potential cytotoxicity from transfection reagents. Two days after transfection, cells were washed with and imaged in external solution (see GEVI characterization in vitro).

Images were acquired using the same microscope as used for screening (see Two-photon screening system) using a 20× NA-0.75 objective (CFI Plan Apochromat Lambda, Nikon). Laser pulses were not pre-compensated for dispersion in the microscope optical path. Excitation wavelengths from 700 to 1080 nm were used in 10-nm increments. At each wavelength, the laser was tuned to a power of 10-20 mW at the sample plane, as measured by a microscope slide power sensor (S170C or S175C, Thorlabs). Each FOV was scanned at all wavelengths by two galvanometer optical scanners with a pixel dwell time of 12.1 μs. Fluorescence values were corrected by subtracting the background. Small deviations in the actual power from the target power were corrected by assuming a quadratic dependence of fluorescence on illumination power at the sample plane. Power was kept unchanged for all fluorophores. Because there is no significant difference in the fluorescence at 920 nm acquired before and after the spectral scan, photobleaching correction was not needed and was not performed.

One-photon excitation and emission spectra

To determine the one-photon excitation and emission spectra for JEDI-2P, we first constructed the pcDNA3.1/Puro-CAG-EGFP-CAAX plasmid as a control by subcloning the CAAX membrane anchoring motif (Choy et al., 1999) to the C-terminal of EGFP. CAAX motif was added to achieve membrane localization like JEDI-2P. HEK293-Kir2.1 cells were plated on wells of a 6-well plate (3516, Corning) to reach a confluency of 60-80% on the day of transfection. Three micrograms of pcDNA3.1/Puro-CAG plasmids expressing JEDI-2P or EGFP-CAAX were transiently transfected using 9 μL jetPRIME transfection reagent, and 200 μL jetPRIME buffer per well. The transfection medium was replaced after 4 h with fresh growth medium #2 to minimize potential cytotoxicity

from the transfection reagent. Forty-eight hours after transfection and for each fluorophore, cells from two wells were detached, washed twice and diluted into in the same imaging solution used for 2PM screening, and pooled into a single well of a 96-well plate (P96-1.5H-N, Cellvis). Pooling the cells to a dense preparation was important to produce a strong signal that could be robustly detected by the plate reader. Untransfected cells were also prepared to determine the background autofluorescence levels. A hemocytometer was used to plate a similar number of cells between conditions.

Spectra were determined by using a plate reader (Cytation 5, BioTek) to quantify fluorescence from wells of the 96-well plates prepared above. Excitation spectra were acquired by scanning excitation wavelengths from 350 to 535 nm in increments of 1 nm and a bandwidth of 10 nm and collecting emission intensity at 560/10 nm. Emission spectra were acquired by exciting at 430/10 nm and measuring emitted photons from 460 to 650 nm in increments of 1 nm and with a bandwidth of 10 nm. Individual scans of excitation and emission spectra were corrected for autofluorescence by subtracting the values from untransfected cells at each wavelength, and then normalized to their respective peaks. The final excitation and emission spectra were determined by averaging the normalized spectra for each of the constructs. The peaks were determined by averaging the peaks from each individual scan.

GEVI one-photon photostability

To determine the one-photon photostability for JEDI-2P, we used the same vectors used for 2PM screening, i.e, pcDNA3.1/Puro-CAG expressing JEDI-2P/ASAP2s/ASAP3/ASAP1-N124V-R406K/ASAP2s-T207H with cyOFP1 attached to the C-terminal of the GEVIs through a GSSGSSGSS linker. These plasmids were transfected into HEK293-Kir2.1 cells in 96-well format using the same methods as described in the Cell culture and transfection in 96-well plates section. Twenty-four hours after transfection, 120 μL of the transfection media in each well was replaced with fresh growth medium #2 to minimize the potential cytotoxicity from transfection reagents. Two days after transfection, cells were washed twice and imaged in the same imaging solution used for 2PM screening.

Images were acquired using the same microscope as used for screening (see Two-photon screening system) using a 20× NA-0.75 objective (CFI Plan Apochromat Lambda, Nikon). For each FOV, one image for the cyOFP1 was taken first, followed by a time-lapse video for the GEVIs. The cyOFP1 image, i.e. the reference channel, was illuminated with 555/15-nm light (SpectraX, Lumencor) and conditioned using the 542-571-nm band of a multiband dichroic mirror (89100bs, Chroma), which has an irradiance of 18 mW/mm^2 at the sample plane. The GEVI video, i.e. the target channel, was illuminated with 470/24-nm light (SpectraX, Lumencor) and conditioned using a long-pass dichroic mirror (T495lpxr, Chroma), which has an irradiance of 15 mW/mm^2 at the sample plane. The emission light from the target channel was further filtered with a band-pass filter (ET525/50, Chroma) to minimize the bleed-through from cyOFP1 emission. Both channels were captured with 5-ms exposure time per frame using an sCMOS camera (ORCA Flash 4.0 V2, Hamamatsu). The target channel was sampled at 2 Hz for the first 20 frames (9.5-sec), and 1 Hz for another 180 (3 mins, Figure 1C) or 300 frames (5 mins, Figures S4G and S4H). Photobleaching traces were calculated from the foreground pixels selected by applying a brightness threshold on both background-corrected channels. The photostability of the sensors was quantified as the area-under-the-curve of the photobleaching trace normalized by the fluorescence at t = 0. The brightness of the sensors was quantified as the green channel fluorescence of the first frame in the video divided by the red channel fluorescence. For each of the GEVI, 6 (Figure 1C) or 4 (Figures S4G and S4H) wells of replicates were tested with n = 1 (Figure 1C) or 2 (Figures S4G and S4H) FOVs in each of the wells. Analysis was performed per FOV and averaged for each well, and the final statistics were drawn at the well level.

Confocal imaging of GEVIs in dissociated neurons

Primary rat cortical neurons were isolated from day 18 Long-Evans rat embryos. Cortices were dissected, dissociated with papain (Worthington Biochemical Corporation), washed with trypsin inhibitor (Sigma), and seeded at 5.0×10^5 cells/mL on 12 mm No. 0 coverslips (633009, Carolina Scientific), each placed in one well of a 24-well plate (3524, Corning). Each well was filled with 500 μL of Neurobasal medium (Invitrogen) supplemented with B-27 (Invitrogen), 2 mM Glutamax (Gibco), 10% FBS, 100 unit/mL Penicillin, and 100 μg/mL Streptomycin. The coverslips were pre-coated with 300 kD poly-D-lysine hydrobromide and washed twice with PBS before seeding. The plating day was considered as day *in vitro* (DIV) 0. The next day, 90% of the media was replaced with a culturing medium consisted of phenol-free Neurobasal medium (Gibco), B-27 (Gibco), 2 mM Glutamax (Gibco), 100 unit/mL Penicillin, and 100 μg/mL Streptomycin. Half of the media was henceforth replaced with fresh culturing medium every 3-4 days. Around DIV 6, further glia growth was limited by adding cytosine β-D-arabinofuranoside to the culturing media to a final concentration of 2 μM. All media were pre-equilibrated for at least 24 h at 37°C in air with 5% CO_2 before usage.

A neuronal expression vector was constructed by cloning JEDI-2P under the control of the neuron-specific hSyn promoter by replacing ASAP2s in pAAV-hSyn-ASAP2s (RRID: Addgene_101276) with JEDI-2P. mCherry was cloned into pcDNA3.1/Puro-CAG vector between the NheI and HindIII sites as a soluble marker of neuronal transfection. Neurons were transfected at DIV 9 using 1 μL lipofectamine 2000 and 800 ng total DNA, including 100 ng pAAV-hSyn-JEDI-2P, 50 ng pcDNA3.1/Puro-CAG-mCherry, and 650 ng pNCS bacterial expression vector as buffer/filler DNA.

Laser-scanning confocal images were obtained 3 days after transfection using a high-speed confocal microscope (LSM880 with Airyscan, Zeiss) driven by the Zen software (version 2.3 SP1, Zeiss). The microscope was equipped with a 40× 1.1-NA water immersion objective (LD C-Apochromat Korr M27, Zeiss), a 488-nm argon laser (LGK7812, Lasos) set to 20% power (~200 μW) and a per-pixel dwell time of 2 μs. Emission light was filtered using a multipass beamsplitter (MBS 488/561/633, Zeiss) and acquired with a 32 channel GaAsP detector (Airyscan, Zeiss) with a detector gain of 850, and a 1.28-Airy unit pinhole size. To increase the signal-to-noise ratio, 2 scans were performed and averaged for each image. Airyscan processing was applied to the images to

increase the resolution. Z stacks were made with 0.27 μm between images. Figure 2K corresponds to a maximum intensity projection from Z stack with 26 images. mCherry was not captured in the final image.

2P voltage imaging in isolated mouse retina

Virus construction and packaging

JEDI-2P was cloned into the pAAV vector (RRID: Addgene_20298) by replacing the hChR2(H134R)-EYFP sequence with JEDI-2P with In-Fusion method. The double-floxed inversed JEDI-2P under the control of EF-1α promoter was then packaged into Adeno-Associated Viruses serotype 1 (AAV2/1) at BCM Neuroconnectivity Core. The final AAV, referred below as AAV2/1-EF1α-DIO-JEDI-2P, had a final concentration of 3-4×10^{12} GC/mL.

Surgeries and GEVI expression

All animal procedures were approved by the governmental review board (Regierungspräsidium Tübingen, Baden-Württemberg, Konrad-Adenauer-Str. 20, 72072 Tübingen, Germany) and performed according to the laws governing animal experimentation issued by the German Government.

To express JEDI in starburst amacrine cells (SACs), we injected 1 μL of the viral construct AAV2/1-EF1α-DIO-JEDI-2P into the vitreous humor of each eye of anaesthetized 5-week-old $ChAT^{Cre}$ mice (n = 2, RRID: IMSR_JAX:006410, The Jackson Laboratory) as described recently (Franke et al., 2017). Imaging experiments were performed 4 weeks after injections. In brief, the retina was dissected from the eyecup, flat-mounted on a filter paper and moved to the recording chamber of the microscope.

Two-photon imaging

For visual stimulation, we used a DLP-based projector (Franke et al., 2019) with UV (390 nm) and green (576 nm) LEDs displaying either 1-s local light flashes (100 μm diameter) or a local chirp stimulus (74 μm diameter, 63 μm offset from the scan field center; for details on chirp stimulus, see (Baden et al., 2016). All visual stimuli were displayed using both UV and green LED, corresponding to an achromatic stimulus. To record light-evoked responses from SACs, we used a movable objective microscope (MOM)-type two-photon microscope (Euler et al., 2009) and acquired time-lapsed 128×1 (at 1.04 kHz), 128×4 (at 260.4 Hz) or 64×32 (at 15.6 Hz) scans for somatic and dendritic voltage imaging with the laser tuned to 927 nm at 9-12 mW laser intensity. The visual stimulus was presented during the retrace period of the laser scanning to prevent light artifacts in the imaging (Franke et al., 2019). The retrace period was ∼20% of the scan duration (e.g., 0.2 ms for a 1-ms line scan). The microscope setup was equipped with GaAsP photomultiplier tubes and a bandpass emission filter (HQ 510/84, AHF/Chroma).

Experimental design

Our experiments were replicated across fields of view and mice. Replicate numbers and definitions are listed in the Figure legends. As there were no comparisons, sample size estimation and blinding in data collection and analysis do not apply. Fields of view were excluded from analysis if the retina was not expressing the sensor or if there were no detectable changes in fluorescence in response to light stimulation.

Data analysis

Pixels of individual imaging scans were chosen for further analysis by measuring their standard deviation (SD) over time. The pixels with the 30% highest SD were analyzed. The voltage trace for each pixel was extracted. Changes in the baseline were corrected by high-pass filtering above 0.2 Hz for frame scans or 0.5 Hz for line scans. Traces were then mean-subtracted and normalized to the standard deviation for that pixel. For trial averaging, traces were aligned relative to trial onset and then resampled to 40 Hz for step and chirp responses. For the 64x32 (15.6 Hz) scans, resampling at higher temporal resolution than the original framerate is possible because the stimulus was presented at different times relative to the recordings for each trial. For SAC somata, selected pixels were split into individual soma by eye. Then, traces of all selected pixels in a field (or soma) were averaged into one region-of-interest (ROI) and filtered with a Savitzky-Golay filter (window of 125 ms and a polynomial order of 2) to remove high frequency noise. Finally, for each ROI we computed the mean activity across stimulus repetitions (n = 20 for flashes,n = 10 for chirp stimuli). To evaluate JEDI-2P photostability, we standardized pixel selection by analyzing the same number (38) of responsive pixels per field of view.

Voltage imaging in *Drosophila* visual neurons using galvanometric point-scanning 2PM

Fly husbandry, *in vivo* two-photon imaging of flies, visual stimulation, and data analysis were done as previously described (Chamberland et al., 2017; Yang et al., 2016) and as described below.

Transgenic flies

JEDI-2P and ASAP3 were cloned into the pJFRC7-20XUAS vector (Pfeiffer et al., 2010) using standard molecular cloning methods, with XbaI and XhoI as the restriction sites (GenScript Biotech for JEDI-2P). The UAS-JEDI-2P and UAS-ASAP3 transgenes were each inserted into the attP40 phiC31 landing site by injection of fertilized embryos (BestGene for JEDI-2P, Rainbow Transgenic for ASAP3). UAS-JEDI-2P was additionally inserted into the VK00005 phiC31 landing site though all experiments presented here used the attP40 insertion. The L2 Gal4 driver (21D-Gal4) was from Rister et al. (2007).

The genotypes of the imaged flies in Figure 4 were:
L2>>ASAP2f: +; UAS-ASAP2f/+; 21D-Gal4/+
L2>>JEDI-2P: yw/+; UAS-JEDI-2P/+; 21D-Gal4/+
The genotypes of the imaged flies in Figure S5 were:

L2>>ASAP2f: +; UAS-ASAP2f/+; 21D-Gal4, jRGECO1b/+
L2>>ASAP3: w/+; UAS-ASAP3/+; 21D-Gal4, jRGECO1b/+

Fly husbandry

All flies used for imaging were raised on standard molasses food at 25°C on a 12/12-h light-dark cycle. Female flies of the appropriate genotypes were collected on CO_2 within 1 day of eclosion and imaged at room temperature (20°C) 6-8 days after eclosion.

Fly surgery

Flies were cold anaesthetized, positioned in a fly-shaped hole cut in steel foil such that their heads were tilted forward approximately 90° to expose the back of the head capsule above the foil while leaving most of the retina below the foil, and then affixed in place with UV-cured glue (NOA 68T from Norland Products Inc.). The brain was exposed by removing the overlying cuticle and fat bodies with fine forceps, and an oxygenated saline-sugar solution (Wilson et al., 2004) was perfused over the fly. The saline composition was as follows: 103 mM NaCl, 3 mM KCl, 5 mM TES, 1 mM NaH_2PO_4, 4 mM $MgCl_2$, 1.5 mM $CaCl_2$, 10 mM trehalose, 10 mM glucose, 7 mM sucrose, and 26 mM $NaHCO_3$. The pH of the saline equilibrated near 7.3 when bubbled with 95% O_2/5% CO_2.

Two-photon imaging

Neurons were imaged with a Leica TCS SP5 II two-photon microscope with a 20×/1.0-NA water immersion objective (Leica HCX APO) and a pre-compensated femtosecond laser (Chameleon Vision II, Coherent). The excitation wavelength was 920 nm and 5-20 mW of power was applied to the sample. Emitted photons were filtered by a 525/50-nm filter and collected with a Hybrid Detector (HyD, Leica). The data were acquired at a constant frame rate of 82.4 Hz using a frame size of 200×20 pixels, 15× digital zoom, a line scan rate of 1,400 Hz, and bidirectional scanning. L2 cells were imaged at their arbor in medulla layer M2. Total imaging time per fly never exceeded 1 h.

Visual stimulation

Visual stimuli were generated with custom-written software using MATLAB (MathWorks) and presented using only the blue LED of a projector (DLP Lightcrafter 4500, Texas Instruments) in Pattern Sequence mode. The stimulus was refreshed at 300 Hz and utilized 6 bits/pixel, allowing for 64 distinct luminance values. The stimulus was projected directly onto a 9 cm × 9 cm rear-projection screen positioned approximately 8 cm anterior to the fly that spanned approximately 70° horizontally and 40° vertically of the fly's visual field. A small square of the stimulus was also simultaneously projected onto a photodiode (SM05PD1A, Thorlabs) configured in a reversed-biased circuit. The stimulus was filtered with a 482/18-nm bandpass filter so that it could not be detected by the microscope detectors. The radiance at 482 nm was approximately 78 $mW \cdot sr^{-1} \cdot m^{-2}$. The imaging and the visual stimulus presentation were synchronized using triggering functions provided by the LAS AF Live Data Mode software (Leica) as well as the signal from the photodiode directly capturing projector output. A data acquisition device (NI DAQ USB-6211, National Instruments) connected to the computer was used to acquire the photodiode signal, generate a trigger signal at the beginning of stimulus presentation, and acquire the trigger produced by the LAS software at the start of each imaging frame. This allowed the imaging and the stimulus presentation to initialize in a coordinated manner and ensured that stimulus presentation details were saved together with imaging frame timings (in MATLAB .mat files) to be used in subsequent processing. Data was acquired at 5 kHz.

The visual stimuli used were:

300-ms search stimulus: alternating full contrast light and dark flashes, each 300 ms in duration, were presented at the center of the otherwise dark screen. The stimulus was such that from the perspective of the fly, the flashing region was 8° from each edge of the screen. In subsequent analysis, the responses to this stimulus were used to select regions of interest (ROIs) with receptive fields located at the center of the screen instead of at the edges. This stimulus was presented for 5,000 imaging frames (61 s) per field of view.

20-ms light and dark flashes from gray (Figures 4C and 4D): single 20-ms light and dark flashes, with 500-ms of gray between the flashes, were presented over the entire screen. The light and dark flashes were randomly chosen at each presentation. The Weber contrast of the flashes relative to the gray was 1. This stimulus was presented for 10,000 imaging frames (122 s) per field of view.

300-ms full-field flash (Figure 4F): alternating full contrast light and dark flashes, each 300 ms in duration, were presented over the entire screen. This stimulus was presented for 100,000 imaging frames (20.3 mins) per field of view.

Experimental design

Our experiments were replicated across many cells and flies. Replicate numbers and definitions are listed in the Figure legends. Data collection and analysis were not done blinded. However, the data was analyzed using automated procedures applied identically for all datasets. Exclusion criteria for flies and regions-of-interest (ROIs) are described below. We estimated the sample size needed based on our previous work with similar assays.

Data analysis

The acquired time series were saved as .lif files and read into MATLAB using Bio-Formats (Open Microscopy Environment) (Linkert et al., 2010). Raw images in each time series were aligned in x and y coordinates by maximizing the cross-correlation in Fourier space of each image with a reference image (the average of the first 30 images in the time series). For each time series, ROIs around individual arbors were selected by thresholding the series-averaged image with a value that generates appropriate ROIs, and then splitting any thresholded ROIs consisting of merged cells and/or drawing any additional ROIs that were missed by the thresholding. For each imaging frame within the time series, intensity values for the pixels within each ROI were averaged and the mean background value (the average intensity in a region of the image without cells) was subtracted. To correct for photobleaching, the time series for each ROI was fit with the sum of two exponentials, and in the calculation of $\Delta F/F_0 = (F(t) - F_0)/F_0$, the fitted value at each time t was used as F_0. This is

mathematically equivalent to calculating $\Delta F/F_0$ from the trace obtained by dividing F(t) by the photobleaching fitted function. For the 300-ms full-field flash and the 300-ms search stimuli, all frames were used to compute the fit, thereby placing $\Delta F/F_0 = 0$ at the mean response after correction for bleaching. For the 20-ms light and dark flashes from gray stimuli, only frames that fell in the last 25% of the gray period were used to fit the bleaching curve; this places $\Delta F/F_0 = 0$ at the mean baseline the cell returns to after responding to the flash instead of at the mean of the entire trace. We did not place the $\Delta F/F_0 = 0$ at the mean baseline of the entire trace because responses to the light and dark flashes are not necessarily equal and opposite. Time series with uncorrected movement, which was apparent as irregular spikes or steps in the $\Delta F/F_0$ traces that were coordinated across ROIs, were discarded.

For the 300-ms full field flash, the 300-ms search, and the 20-ms light and dark flashes from gray stimuli, the stimulus-locked average response was computed for each ROI by reassigning the timing of each imaging frame to be relative to the stimulus transitions (dark to light or light to dark for the 300-ms full-field flash or search stimuli, gray to light or gray to dark for the light and dark flashes from gray) and then computing a simple moving average. The averaging window was 8.33 ms and the shift was 8.33 ms, which effectively resampled our data from 82.4 Hz to 120 Hz.

As the screen on which the stimulus was presented did not span the fly's entire visual field, only a subset of imaged ROIs experienced the stimulus across approximately the entire extent of their spatial receptive fields. These ROIs were identified based on having a response of the appropriate sign to the 300-ms search stimulus. ROIs lacking a response to these stimuli or having one of the opposite signs were not considered further.

The quantification metrics for each ROI (Figure 4D) were computed as follows:

The peak response to each flash was the $\Delta F/F_0$ value farthest from zero in the expected direction of the initial response (depolarization or hyperpolarization). The time to peak was the time at which this peak response occurred, relative to the start of the light or dark flash.

Voltage imaging in the mouse cortex using resonant scanning 2PM

All procedures were carried out in accordance with the ethical guidelines of the National Institutes of Health and were approved by the Institutional Animal Care and Use Committee (IACUC) of Baylor College of Medicine.

Viral construction and packaging

We created a soma-targeted version of JEDI-2P, which we abbreviate as JEDI-2P-Kv in the construct names below. JEDI-2P-Kv was cloned into the pAAV vector (RRID: Addgene_20298) by replacing the hChR2(H134R)-EYFP sequence with JEDI-2P-GSSGSSGSS-Kv with In-Fusion method, where Kv is the C-terminal motif of Kv2.1 potassium channel for soma localization (Lim et al., 2000). The double-floxed inversed JEDI-2P-Kv under the control of EF1α promoter was then packaged into Adeno-Associated Viruses serotype 1 (AAV2/1) at the Canadian Neurophotonics Platform (Université Laval) viral vector core. The final AAV, referred below as AAV2/1-EF1α-DIO-JEDI-2P-Kv, had a final concentration of around 7.5×10^{12} GC/mL. In the corresponding main text section and figures, to avoid using an additional abbreviated construct name (JEDI-2P-Kv), we simply state that we used the soma-localized version of JEDI-2P.

Viral injections

Functional imaging was performed in B6;129S-Slc17a7<tm1.1(cre)Hze>/J mice (RRID: IMSR_JAX:023527) injected with AAV2/1-EF1α-DIO-JEDI-2P-Kv resulting in JEDI-2P expression in pyramidal cells. Injections were performed through a burr hole targeted stereotactically to visual cortex (2.8 mm lateral of the midline, and 1.5 mm anterior to the lambdoid suture). In each mouse, 500-1000 nL of virus was injected approximately 350 μm deep via a nano-injection pump (WPI). After at least 2 weeks to allow for expression, mice craniotomies were performed above the injection site, and mice were prepared each with a cranial window as described below. Mice were housed in standard conditions (12-h light/dark cycles, light on at 6 a.m., with water and food *ad libitum*).

Cranial window

Anesthesia was induced with 3% isoflurane and maintained with 1.5% to 2% isoflurane during the surgical procedure. Mice were injected with 5-10 mg/kg ketoprofen subcutaneously at the start of the surgery for analgesia. Anesthetized mice were placed in a stereotaxic head holder (Kopf Instruments) and their body temperature was maintained at 37°C throughout the surgery using a homeothermic blanket system (Harvard Instruments). After shaving the scalp, bupivacaine (0.05 cc, 0.5%, Marcaine) was applied subcutaneously, and after 10-20 min an approximately 1-cm^2 area of skin was removed above the skull and the underlying fascia was scraped and removed. The wound margins were sealed with a thin layer of surgical glue (VetBond, 3M), and a 13-mm stainless-steel washer clamped in the headbar was attached with dental cement (Dentsply Grip Cement). At this point, the mouse was removed from the stereotaxic frame and the skull was held stationary on a small platform by means of the newly attached headbar. Using a surgical drill and long straight shank (HP) 1/2 burr, a 4-mm craniotomy was made centered on the viral injection burr hole, and the exposed cortex was washed with artificial cerebrospinal fluid (ACSF) (125 mM NaCl, 5 mM KCl, 10 mM Glucose, 10 mM HEPES, 2 mM $CaCl_2$, 2 mM $MgSO_4$). The cortical window was then sealed with a 4-mm diameter coverslip (Warner Instruments), using cyanoacrylate glue (VetBond).

Resonant scan 2P voltage imaging

Two-photon (2P) imaging was performed on a Thorlabs Bergamo resonant scanning microscope with 920 nm excitation via a titanium:sapphire femtosecond laser (Chameleon Vision II, Coherent). A 1.1-NA 25× objective lens was used (CFI75 Apochromat 25XC W, Nikon Instruments) except for patching, where a 0.8-NA long-working distance 16× lens (CFI75 LWD 16X W, Nikon Instruments) was used to allow space for the patch pipette to approach the tissue under the microscope. The emission was split by a

dichroic mirror into two channels: the green channel used a 525/50 nm filter, and the red channel used a 625/90 nm filter, before being collected by two photomultiplier tubes. ScanImage software (Vidrio) was used to control the microscope and acquire imaging data. Imaging power was kept between 20-70 mW depending on depth and field of view.

In-vivo *patching*

To perform simultaneous 2P imaging and patching, the coverslip was removed and replaced with a new coverslip that had been pre-drilled with a small (~500 μm diameter) hole using a diamond-tipped burr (Choltene/Whaledent). The opening in the coverslip was positioned so that a patch pipette approaching at an angle through the hole could target nearby JEDI-2P-expressing cells. Mice were kept under 1-2% isoflurane anesthesia throughout the experiment and their temperature was maintained with a homeothermic blanket.

Patch pipettes were pulled from borosilicate glass (1.5 mm outer diameter × 0.86 mm inner diameter, Sutter Instruments) to an impedance of 6-12 MΩ. Pipettes were filled with standard external solution (ACSF) and Alexa Fluor 594 dye was added (50 μM) to allow visualization of the pipette and extracellular space (Häusser and Margrie, 2014). A manometer (Fisher Scientific 06-664-19) and custom-built pressure manifold allowed fast switching between high pressures while entering the bath and penetrating the dura (~150 mbar), and low pressures (~20-50 mbar) while advancing the pipette through the cortex under 2P guidance, which helped to reduce the overall volume of intracellular solution ejected from the pipette. Bias currents were zeroed once the pipette was placed in the bath.

JEDI-2P-expressing cells were targeted for recording by approaching the cell under 2P guidance and establishing a juxtacellular seal that enabled visualization of neuronal spiking. After each recording, positive pressure was applied, which often broke open the cell membrane and enabled intracellular injection of the Alexa Fluor 594 dye that enabled us to confirm that we were recording from the cell that we had been imaging.

Voltage imaging without in-vivo *patching*

Voltage imaging experiments without *in vivo* patching were done in awake behaving head-fixed mice on a linear non-motorized treadmill under the two-photon microscope (Figure 5A). Data were collected while mouse was presented with visual stimuli consisting of Gaussian noise with coherent orientation and motion. After imaging, the washer was released from the headbar and the mouse was returned to the home cage.

Experimental design

Our experiments were replicated across multiple cells and mice. Replicate numbers and definitions are listed in the Figure legends. No statistical comparisons were made, so blinding does not apply. Cells monitored under simultaneous electrophysiological and optical recordings were included for analysis if (1) we achieved a successful juxtacellular patch with adequate (electrical) signal to noise to enable unambiguous identification of (electrical) spikes, and (2) we confirmed that the imaged cell was the patched cell via optical response to current injection and/or filling of the soma with Alex Fluor dextran after the recording. Cells that passed the inclusion criteria were from 4 animals (3 males, 1 female) age 2-6 months at the time of imaging.

Data analysis (general procedures)

In all cases, neurons in the fluorescence traces were manually segmented from the mean image of the optical recordings. We performed basic motion correction using image registration against a template. Raw fluorescence traces were computed as the average of pixels inside neurons. To correct for background fluorescence, we subtracted from the raw traces the running average (10 s window) of the darkest pixels within the FOV. Changes in baseline fluorescence due to focus drift or photobleaching were corrected by using a Butterworth filter of order 3 and cutoff frequency at 0.005 Hz. $\Delta F/F_0$ was computed using the baseline corrected traces.

Spike inference

Patch recordings and imaging data were synchronized by copying the frame pulse signal generated at the start of each imaging frame to the patch clamp acquisition software. The patch clamp recordings were acquired at 10 kHz and filtered using a Butterworth filter of order 3 and cutoff at 0.1Hz. The filtered signal was convolved with a Gaussian filter with standard deviation equal to 3 to remove small peaks. Ground truth spikes were determined by a manual threshold and imposing a minimal inter-spike interval of 3 ms. While MLSpike (Deneux et al., 2016) distinguished apparent subthresholds and spikes in our ULoVE recordings, we obtained poor results with our resonant scan recordings, possibly due to their lower SNR. To extract optical spike times and maximize the SNR of traces, we instead used the VolPy algorithm (Cai et al., 2021). VolPy was initialized with binary masks obtained from the manually segmented neurons, conducted rigid motion correction with NormCorre (Pnevmatikakis and Giovannucci, 2017) and simultaneously inferred optimal pixel weights, spike timings, and subthreshold signals. To evaluate the correlation (Pearson's r^2), the synchronized electrical and optical spikes were split into bins of 40 ms (Berens et al., 2018). Electrical and optical spikes were counted in each bin, and the Pearson's correlation (r^2) between these two vectors was computed. The F_1 score was computed using the procedure described in (Cai et al., 2021), but using the timespans indicated in the main text and Figure S6D rather than the ±10 ms (i.e., an interval of 20 ms) used in Cai et al., 2021.

Determining JEDI-2P's response amplitude to spikes

Patched cells were manually segmented. The amplitude of the optical response to each spike was computed as the difference between the $\Delta F/F_0$ value at the time of the peak of the corresponding electrical spike and the average of $\Delta F/F_0$ between 40 and 20 ms before the peak of the electrical spike.

To compute the spike-triggered average in Figures S6A–S6C, isolated spikes (only one spike within ±100 ms) were identified in the electrical trace. We extracted the datapoints within 100 ms of each isolated spike. These electrical traces were normalized to 1.0 at

the peak of the spike and 0 at the minimum value of the extracted datapoints. Because optical and electrical recordings are synchronized, the fluorescence traces corresponding to each electrical spike were extracted and aligned. The $\Delta F/F_0$ values were computed as described above.

High-resolution optical spike waveforms

To construct a fluorescence impulse response with a high temporal resolution, we performed a spike-triggered analysis at the level of pixels. Since the acquisition time of each pixel was recorded and the optical trace is synchronized with the electrical trace, we could determine the time at which each pixel was recorded relative to an action potential peak (Figures S6E and S6F). Specifically, we selected bright pixels from the neuron, and, for each spike, we determined their $\Delta F/F_0$ and relative timing compared with the spike peak. The $\Delta F/F_0$ values in bins of 0.227 ms were averaged to produce Figure 5E. The bin size was chosen to produce a 10-fold higher effective temporal resolution (4.4 kHz) than our standard imaging speed (0.44 kHz).

Directional tuning curves

To determine the directional tuning curves of individual neurons, we presented mice with Gaussian noise with coherent orientation and motion. 16 directions of motion were randomly interleaved and repeated 20 times. Each presentation period lasted 0.5 s. We rectified the $\Delta F/F_0$ values obtained, i.e., hyperpolarizations (positive $\Delta F/F_0$ values) were set to zero. To produce direction tuning graphs, we computed the mean $\Delta F/F_0$ for each direction of motion.

Voltage recording in the mouse cortex using ULoVE

All protocols adhered to the guidelines of the French National Ethic Committee for Sciences and Health report on Ethical Principles for Animal Experimentation in agreement with the European Community Directive 86/609/EEC under agreement #12007.

Viral vector construction and packaging

We created the AAV sequence the same way we reported in the section above (resonant scanning). The double-floxed inversed sequence under the control of EF-1α promoter was then packaged into AAV2/1 at BCM Neuroconnectivity Core. The final AAV, referred below as AAV2/1-EF1α-DIO-JEDI-2P-Kv, had a final concentration of around 3.1×10^{12} GC/mL. In the corresponding main text section and figures, to avoid using an additional abbreviated construct name (JEDI-2P-Kv), we simply state that we used the soma-targeted version of JEDI-2P. Viral vector construction, AAV packaging, and viral injections of the soma-targeted version of ASAP3 (ASAP3-Kv) were described previously (Villette et al., 2019).

Animal handling, viral injections, and surgeries

5 male wild-type C57BL/6J mice were housed in standard conditions (12-hour light/dark cycles, light on at 7 a.m., with water and food *ad libitum*). Viral constructs AAV1.hSyn.Cre (final titer: 2×10^{9} GC/mL, University of Pennsylvania Vector Core) and AAV2/1-EF1α-DIO-JEDI-2P-Kv (3×10^{12} GC/mL) were combined in PBS, 300 nL of which was injected at a flow rate of 75 nL/min into the visual cortex (V1 coordinates from bregma: anteroposterior –3/–3.5 mm, mediolateral –2.5/–3 mm, and dorsoventral –0.3 mm from brain surface), of adult male wild-type C57BL/6J mice (body weight 25–30 g). A preoperative analgesic was used (buprenorphine, 0.1 mg/kg), and Zolethil-Xylazine were used as anesthetic (Centravet). A 5-mm diameter #1 coverslip was placed on top of the targeted cortical area immediately after the viral injection and secured with dental cement. A custom-designed aluminum head-plate was fixed on the skull with layers of dental cement after the coverslip implantation. Mice were allowed to recover for at least 15 days before recording sessions and housed one per cage. Behavioral habituation was adopted, involving progressive handling by the experimenter with gradual increases in head fixation duration (Villette et al., 2017). Mice were handled before recording sessions to limit restraint-associated stress, and experiments were performed during the light cycle.

ULoVE voltage optical recording

3-hour recording sessions were performed while mice behaved spontaneously on top of an unconstrained running wheel in the dark. Recordings were performed using a custom designed acousto-optic deflector (AOD) -based random-access multiphoton system (Karthala System) based on a previously described design (Villette et al., 2019). The excitation was provided by a titanium:sapphire femtosecond laser (InSight X3, Spectra Physics) mode-locked at 920 nm with a repetition rate of 80 MHz. A 25× water-immersion objective (0.95-NA, 2.5-mm working distance, Leica) was used for excitation and epifluorescence light collection. Laser power was set to deliver 15 mW post-objective and pre-sample then adjusted for mono-exponential loss through tissue with a length constant of 170 μm. We further doubled the power to account for the greater excitation volume compared with that used in standard 2P laser scanning microscopy. The signal was passed through a 720-nm shortpass filter, split into two channels using a 580-nm dichroic mirror (Semrock), and passed to two H10769/40 cooled photomultiplier tubes (Hamamatsu) in photon counting mode, with the green channel used for JEDI-2P and the other channel not used. ULoVE excitation patterns were either two or three 9× multiplexed patterns (Villette et al., 2019) per cell, yielding a temporal resolution of 2525 Hz, or 3333 Hz (for the recording in layer 5). Paired recordings were stopped at 10 to 15 min, depending on the stability, while longer continuous recordings, up to 42 min, were performed for single cells.

Experimental design

Our experiments were replicated across multiple cells and mice. Replicate numbers and definitions are listed in the Figure legends. The study was not done blinded, but all the critical comparisons are based on data analyzed by automated methods. We did not conduct a pre-hoc power analysis. For recording, we selected neurons that were sufficiently bright to obtain significant signal-to-noise. Selection of cell pairs required cells in the same focal plane. No other selection criteria were used, and all cells chosen for recording were included in our analysis. Statistical tests are described in the figure legends.

Morphometry analysis

The depth of the neurons was obtained by measuring the distance between the bottom of the dura and the center of the cell in the axial axis (Figure S9B). Cell diameters (Figure S9A) were obtained after two steps: first, motion correction was performed from a high-resolution temporal stack of 50 frames acquired prior to the ULoVE recording at a high spatial resolution at 4 pixels per micron; secondly, we obtained the diameter by averaging the width and the height of the outer border of the soma. Distance between cells was calculated between cell centroids.

Spikes and UP-DOWN states

We used the same three-step analytic procedure as described (Villette et al., 2019). The outcome of the first two steps was used to feed MLspike (Deneux et al., 2016) with the following final parameter settings (mean ± SD, [range]): amplitude (in $-\Delta F/F$) 0.19033 ± 0.043145 [0.1 - 0.276], tau decay (in seconds) 0.0012494 ± 0.00036347 [0.0006522 - 0.002231], tau rise (in seconds) 0.00079444 ± 0.000114725 [0.0005 - 0.001], sigma 0.0415 ± 0.0058236 [0.03 - 0.056], drift 0.20722 ± 0.038218 [0.1 - 0.25], Fmin 0.8313 ± 0.036821 [0.8 - 0.90264], Fmax 1.1283 ± 0.030845 [1.04 - 1.2], Discretization baseline 40 ± 0 [40 - 40], Discretization decay 10 ± 0 [10 - 10] and Discretization rise 5 ± 0 [5 - 5]. The amplitude of the individual detected spikes was obtained by taking the peak value of the fluorescence signal smoothed with a Gaussian kernel (0.2 ms) subtracted relative to the local baseline fluorescence (drift output from MLspike). The evolution of spike amplitude was calculated by performing a linear regression of spike amplitudes across time and the slope. Decay time constant was extracted from a mono-exponential fit on the average spike. The spike width was quantified from the spike trigger average waveform as the full width half maximum (FWHM). UP state magnitude was obtained by fitting a double Gaussian fit on the low pass filtered trace (cutoff at 30 Hz) and calculating the peak of the Gaussian distribution corresponding to more depolarized states (Figures S8F–S8H). For figures, traces were smoothed using a Gaussian kernel of 0.2 ms. A bi-exponential model was used to correct traces for photobleaching over long timescales.

Pairwise analyses

To quantify correlations of the low fluctuating membrane potential dynamics (Gaussian filter of 15 ms), we performed cross-correlation using the built-in MATLAB function (xcorr) where the first input was the trace of the cell #1, the second input was the trace of the cell #2 and the maximal lag set at 500 ms. We then normalized the resulting vector to values from –1 to +1 by dividing it by (1) the product of the standard deviations of the two traces and (2) the number of time points. To evaluate the significance of this correlation, we performed a bootstrap procedure whereby the trace of cell #2 was shifted by a random lag. 1000 randomly shifted traces were obtained in this way and their cross-correlation analyzed as above. The significance of the results was expressed using Z-scores, i.e., the number of standard deviations from the mean. To obtain the Z-score, we first subtracted the mean cross-correlation of the 1,000 randomly shifted traces from the cross-correlation obtained with the original data. We then divided this adjusted mean by the standard deviation of the cross-correlation values of the 1,000 randomly shifted traces. A similar process is performed for spike trains where spikes are represented by a vector where we quantified the number of spikes per time bin. 1-ms and 15-ms time bins were both quantified. Spike quantification was performed by rolling the time bins across the duration of the recordings in steps of 1 time point (0.4 ms since these recordings were performed at 2.5 kHz). The 1-ms time bin was chosen to evaluate precise spike synchrony, while the 15-ms time bin was chosen to evaluate looser correlations. Of note, the 15-ms bin width is similar to the bin width (20 ms) used by a previous study that reported spike-train correlations from dual intracellular recording data (Poulet and Petersen, 2008). Locomotion speed was extracted as previously described (Villette et al., 2017, 2019). To obtain the degree of spike-rate modulation of a pair, we extracted the cell-specific speed to firing rate correlation as previously described (Villette et al., 2019). Briefly, a slope expressed in Hz/(cm/s) was obtained from the average firing rate of the cell as a function of the speed of the animal. To express the degree of spiking rate modulation per cell pair, we simply averaged the values of each cell within the pair.

To evaluate whether the behavior changed the strength of the trace cross-correlation (Figure 7G), we first isolated the rest epochs from the locomotion epochs (longer than 1 s accounting for two lags) and kept pairs that accumulate locomotion epochs for at least 5% of their full duration (mean ± SD: fraction 15.75 ± 7.38%, duration 3.2 ± 2.3 s, 50.2 ± 33.7 locomotion epochs/pair, n = 12 pairs, 4 mice). The behavior-specific cross-correlation was performed by concatenating the rest or the locomotor epochs to get a rest and a locomotion cross-correlation respectively. The bootstrap procedure was performed, but, this time, we permuted the epochs within the behavioral group and obtained 500 bootstrap cross-correlations for rest and the same amount for locomotion. We assessed the significance by calculating Z-score as described above but taking the difference between the rest to the locomotor specific cross-correlation and took Z = 2 as the threshold of significance.

QUANTIFICATION AND STATISTICAL ANALYSIS

For every comparison in the manuscript, we describe (1) the statistical test used, (2) the exact value of *n*, (3) what *n* represents, (4) the measure of the center (e.g., mean or median), and (5) the definition of the error bars. For all comparisons related to a figure, the statistical details are included in the corresponding Figure legend. For all other comparisons, they are listed in the results section. A statistical comparison was defined to be significant if the p-value was less than 0.05, unless stated otherwise. The correspondence between asterisks and p-values are listed in the Figure legends. Exclusion criteria are listed in the corresponding method details section, when appropriate.

When comparing two groups, we performed the two-sided t tests, except for data related to the ULoVE section in which nonparametric tests (Mann-Whitney or Kolmogorov-Smirnov) were used. For experiments that compared the means of more than two

groups, we used the ANOVA. Prior to the t test, one-way and two-way ANOVA, we conducted the F test, Brown–Forsythe test, and Spearman's test, respectively, to compare the variances of the groups. When the variances were statistically different, the Welch's correction was applied when appropriate. Because normality tests have low power when the sample size (n) is small (Ghasemi and Zahediasl, 2012), we did not conduct normality tests and assumed normality. For one-way and two-way ANOVAs, we conducted post hoc multiple comparison tests (Bonferroni, Tukey, Sidak, or Dunnett).

The fact that different baseline-correction methods were used in different sections of the paper reflects the preference or established procedures of the specific lab that analyzed the corresponding data. It does not indicate differences in the indicator properties between the different preparations.

CellPress
OPEN ACCESS

Supplemental figures

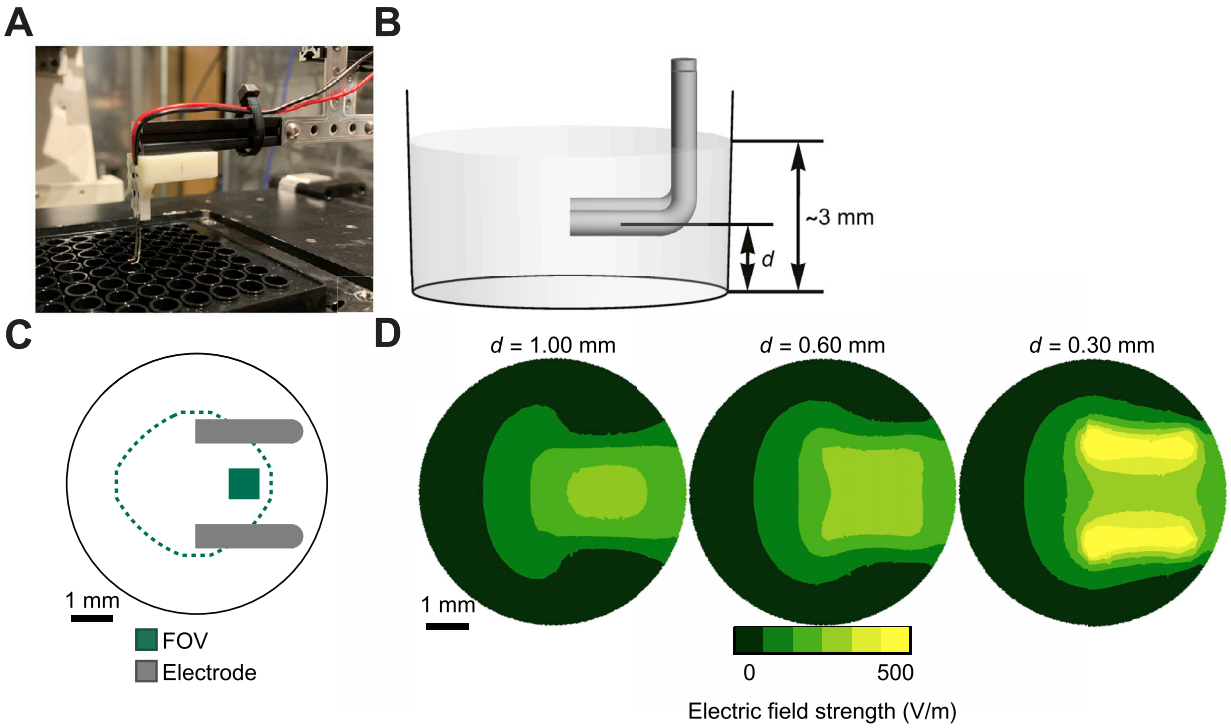

(legend on next page)

Figure S1. Design and benchmarking of the automated screening platform, related to Figure 1

(A–D) Position of the field electrodes within a well of a 96-well plate. (A) A photo of the motorized platinum electrode system positioned on top of a 96-well plate. (B and C) Schematics of the pair of field electrodes positioned in a well, viewed from the side (B) and top (C). (B) Wells are filled with 100 μL of external solution, producing a liquid height of ~3 mm. *d* is the distance from the surface of the glass at the bottom of the well and the center of the horizontal section of the field electrodes. The optimal value for *d* is explored in (D). (C) Top-view schematic showing the location of a representative field of view (FOV) compared with the electrodes. FOVs were always imaged at the same location with respect to the electrodes. We typically imaged 4 FOVs per well. All FOVs were within the area bounded by the dashed green line to avoid collisions between the electrodes and the well perimeter. (D) For screening GEVIs, we positioned the electrodes at a height (D) of 0.6 mm to optimize the uniformity of the electric field between the electrodes. Electric field strength, shown here as a contour plot, was computed by 3D finite element modeling assuming a voltage of 1 V between the two electrodes.

(E and F) 1-ms electric field stimulations of GEVI-expressing HEK293-Kir2.1 cells produce rapid and repeatable fluorescence responses. (E) Representative responses of ASAP2s-expressing cells to 1-ms electric field stimulation pulses. (F) Mean GEVI responses to 1-ms field stimulation pulse had a full width at half maximum between 13.5 to 19.8 ms. Traces correspond to averages from 6 wells with 4 fields of view per well and 20 stimulations per field of view. Traces were normalized to their respective peaks. Data are the same as in Figure 1G.

(G–I) To ensure that our fully automated methods for quantifying GEVI performance did not produce large systematic or random errors, we measured the same parameters using individual cells that were manually selected. Automated and manual measurements of response amplitude (G), brightness (H), and photostability (I) were highly correlated ($r^2 > 0.94$). n = 6 independently transfected wells for both manual and automated analyses. For the automated analyses, we followed the standard protocol of analyzing 4 FOVs per well. For manual analyses, we measured 2–42 cells per well and >160 cells per GEVI. The values here are different from those in Figure 1 as they were acquired using slightly different experimental settings.

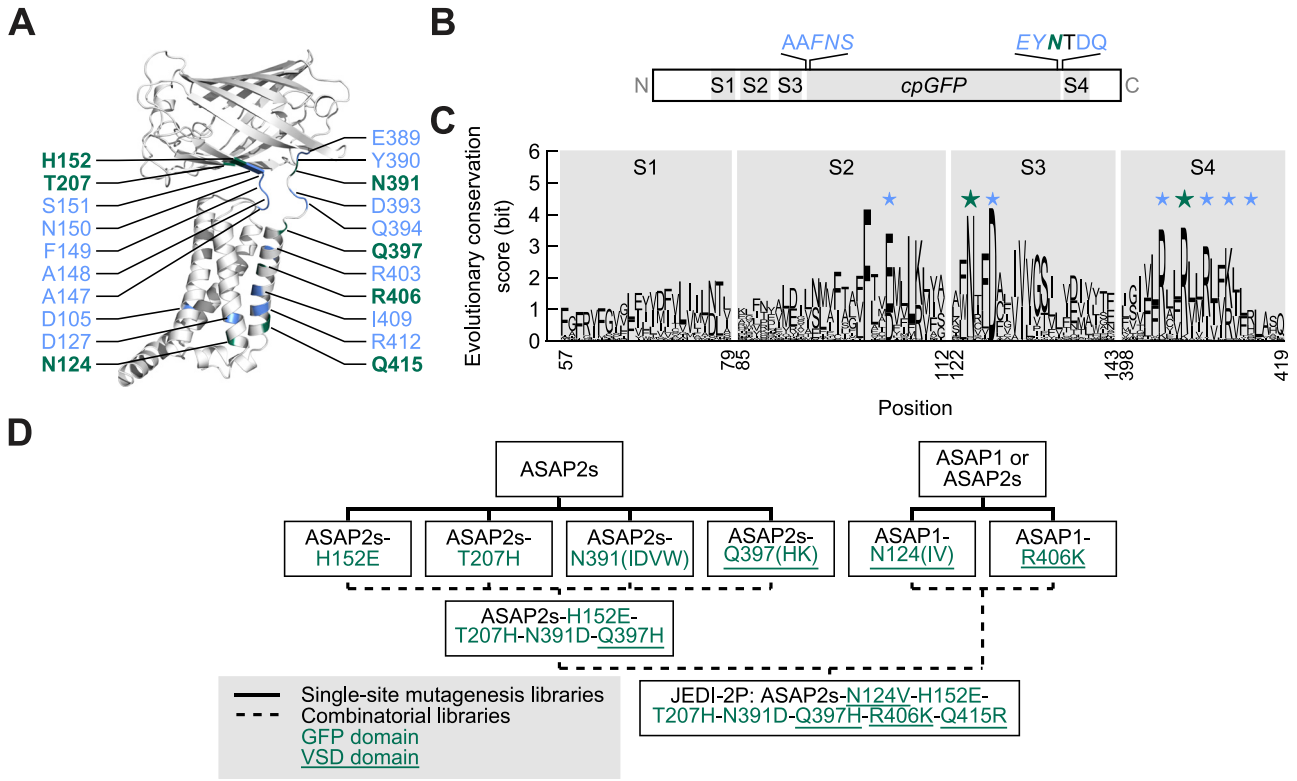

Figure S2. GEVI screening strategy and performance of screening intermediates, related to Figure 1

(A) Screened residues (blue and green) overlaid on an *in silico* 3D model of ASAP2s. Residues that are mutated in JEDI-2P are in bold green.

(B) Several screened residues were located near the junction between the sequences of the voltage-sensing domain and the fluorescent protein (cpGFP). Residues correspond to the parental sensor ASAP2s. cpGFP residues are in italic; residues mutated in JEDI-2P are bold green; and screened positions that are not mutated in JEDI-2P are in blue. One residue that was not screened is shown in black.

(C) Several screened residues in the voltage-sensing domains were highly conserved residues. The figure shows a sequence logo constructed using 2,522 homologs of the voltage-sensing domain used in the ASAP family of indicators. Homologs were identified by BLASTing the NCBI non-redundant protein sequences database (nr) with the sequence of the voltage-sensing domain from ASAP2s. Homologs were aligned using the BLOSUM62 scoring matrix. The shaded areas correspond to the four transmembrane helixes (S1–S4). Many residues with high evolutionary conservation scores were targeted for mutation (small blue stars). JEDI-2P incorporates mutations at the two positions labeled with large green stars.

(D) Directed evolution path leading to JEDI-2P.

(E) Candidates were evaluated based on single characteristics (first three columns) and compound measures (last two columns). The detectability index is defined as response amplitude times the square root of the relative brightness. The detectability budget is defined as the detectability index times the square root of the photostability. More information on individual metrics is provided in the main text. Relative values are compared with ASAP2s. Bars show the mean, and error bars are the 95% CI. n = 6 independent transfections.

```
          1                                                   50
ASAP2s    METTVRYEQG SELTKTSSSP TADEPTIKID DGRDEGNEQD SCSNTIRRKI
ASAP3     METTVRYEQG SELTKTSSSP TADEPTIKID DGRDEGNEQD SCSNTIRRKI
JEDI-2P   METTVRYEQG SELTKTSSSP TADEPTIKID DGRDEGNEQD SCSNTIRRKI

          51                                                  100
ASAP2s    SPFVMSFGFR VFGVVLIIVD IIVVIVDLAI SEKKRGIREI LEGVSLAIAL
ASAP3     SPFVMSFGFR VFGVVLIIVD IIVVIVDLAI SEKKRGIREI LEGVSLAIAL
JEDI-2P   SPFVMSFGFR VFGVVLIIVD IIVVIVDLAI SEKKRGIREI LEGVSLAIAL

          101                                                 150
ASAP2s    FFLVDVLMRV FVEGFKNYFR SKLNTLDAVI VVGTLLINMT YSFSDLAAFN
ASAP3     FFLVDVLMRV FVEGFKNYFR SKLNTLDAVI VVGTLLINMT YSFSDG.TFR
JEDI-2P   FFLVDVLMRV FVEGFKNYFR SKLVTLDAVI VVGTLLINMT YSFSDLAAFN

          151                                                 200
ASAP2s    SHNVYITADK QKNGIKANFT VRHNVEDGSV QLADHYQQNT PIGDGPVLLP
ASAP3     GDNVYITADK QKNGIKANFT VRHNVEDGSV QLADHYQQNT PIGDGPVLLP
JEDI-2P   SENVYITADK QKNGIKANFT VRHNVEDGSV QLADHYQQNT PIGDGPVLLP

          201                                                 250
ASAP2s    DNHYLSTQTV LSKDPNEKRD HMVLLEFVTA AGITHGMDEL YGGTGGSASQ
ASAP3     DNHYLSTQTV LSKDPNEKRD HMVLLEFVTA AGITHGMDEL YGGTGGSASQ
JEDI-2P   DNHYLSHQTV LSKDPNEKRD HMVLLEFVTA AGITHGMDEL YGGTGGSASQ

          251                                                 300
ASAP2s    GEELFTGVVP ILVELDGDVN GHKFSVRGEG EGDATIGKLT LKFICTTGKL
ASAP3     GEELFTGVVP ILVELDGDVN GHKFSVRGEG EGDATIGKLT LKFICTTGKL
JEDI-2P   GEELFTGVVP ILVELDGDVN GHKFSVRGEG EGDATIGKLT LKFICTTGKL

          301                                                 350
ASAP2s    PVPWPTLVTT LTYGVQCFSR YPDHMKRHDF FKSAMPEGYV QERTISFKDD
ASAP3     PVPWPTLVTT LTYGVQCFSR YPDHMKRHDF FKSAMPEGYV QERTISFKDD
JEDI-2P   PVPWPTLVTT LTYGVQCFSR YPDHMKRHDF FKSAMPEGYV QERTISFKDD

          351                                                 400
ASAP2s    GKYKTRAVVK FEGDTLVNRI ELKGTDFKED GNILGHKLEY NTDQMPQMVT
ASAP3     GKYKTRAVVK FEGDTLVNRI ELKGTDFKED GNILGHKLEY NTDQMPQMVT
JEDI-2P   GKYKTRAVVK FEGDTLVNRI ELKGTDFKED GNILGHKLEY DTDQMPHMVT

          401                     427
ASAP2s    LLRVLRIVIL IRIFQLASQK KQLEVVT
ASAP3     LLRVLRIVIL IRIFQLASQK KQLEVVT
JEDI-2P   LLRVLKIVIL IRIFRLASQK KQLEVVT
```

Figure S3. Sequence alignment of ASAP2s, ASAP3, and JEDI-2P, related to Figure 1

Protein sequences of ASAP2s (Chamberland et al., 2017), ASAP3 (Villette et al., 2019), and JEDI-2P were aligned with Clustal Omega 1.2.4 (Madeira et al., 2019) using default parameters: no gap removing, enable mbed-like clustering guide-tree, enable mbed-like clustering iteration, number of iterations = 0, max guide-tree iterations = −1, max hidden Markov model iterations = −1. Sequence differences are highlighted in yellow.

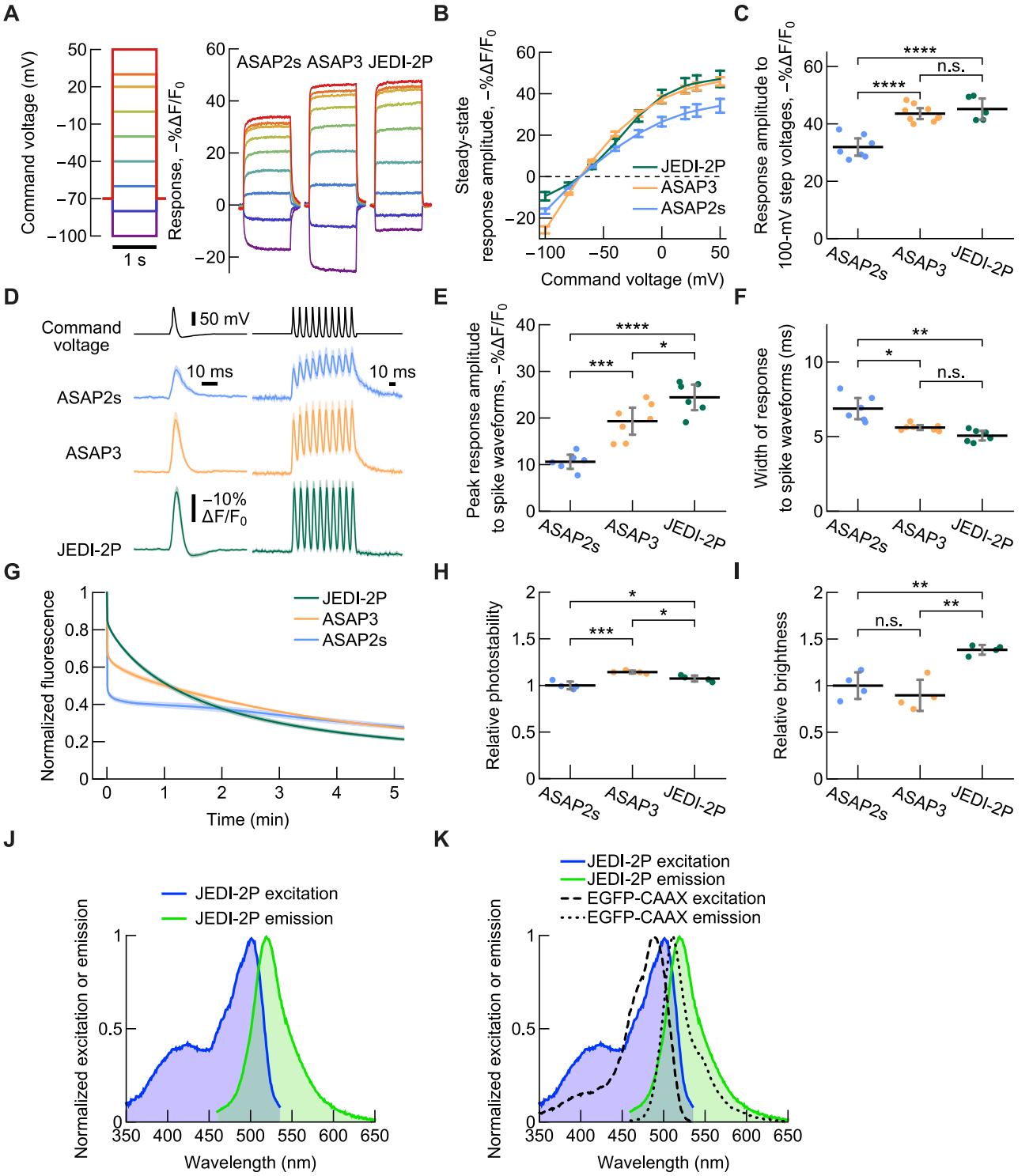

Figure S4. ***In vitro*** **characterization of JEDI-2P under one-photon microscopy, related to Figure 2**

(A–C) JEDI-2P and ASAP3 produce similar steady-state responses to step depolarizations under 1PM. Voltage was modulated by whole-cell voltage clamp. n = 7 (ASAP2s), 8 (ASAP3), and 9 (JEDI-2P) HEK293A cells. (A) Mean fluorescence responses to voltage steps. Traces were smoothed by a 10-ms moving average. (B) Quantification of (A). (C) Peak response amplitude to a 100-mV voltage step from a resting potential of −70 mV. $p < 0.001$, ANOVA.

(D–F) Under 1PM, JEDI-2P produces larger responses to spike waveforms and tracks voltage more faithfully than ASAP3 and ASAP2s. Voltage was modulated by whole-cell voltage clamp. The spike waveforms had a 2-ms full width at half maximum. n = 6 (ASAP2s & JEDI-2P) and 7 (ASAP3) HEK293A cells. (D) Mean responses to a single spike waveform (averaged from 20 trial per cell, *left*) and a 100-Hz spike train (*right*). The fluorescence of JEDI-2P returns to the baseline

(legend continued on next page)

between spikes, unlike that of ASAP2s and ASAP3. This is likely because JEDI-2P's repolarization kinetics are described by a single fast exponential of 2.54 ± 0.30 ms (mean ± 95% CI). In contrast, ASAP2s' and ASAP3's repolarization kinetics are bi-exponential, with a fast repolarization component of ∼13 and ∼16 ms, respectively (Table S2). Both indicators have additional slow repolarization time constants. (E) Quantification of the peak response amplitude to a single spike waveform. Black lines indicate means. $p < 0.0001$, ANOVA. (F) Full width at half maximum of the fluorescence response to single action potential waveforms. $p < 0.01$, Welch ANOVA with Dunnett T3 post hoc tests.

(G and H) Comparison of the photostability of JEDI-2P, ASAP3, and ASAP2s. The irradiance was 15 mW/mm^2 at the sample plane. Assays were conducted at a polarized potential (∼ −77 mV) by expressing GEVIs in HEK293-Kir2.1 cells. (G) Normalized mean fluorescence as a function of time. JEDI-2P shows a smaller fast-photobleaching component than ASAP3 and ASAP2s. (H) Relative photostability, defined as the area under the normalized fluorescence in (A). Note that because of the difference in the shapes of the photobleaching curves of the three GEVIs, indicator rankings will vary based on the duration of the photobleaching time course. Black bars denote the mean of n = 4 independent transfections per GEVI. $p < 0.001$, ANOVA.

(I) JEDI-2P is brighter than ASAP3 and ASAP2s under 1PM. Assays were conducted at a polarized potential (∼ −77 mV) by expressing GEVIs in HEK293-Kir2.1 cells. Black bars denote the means of n = 4 independent transfections per GEVI. $p < 0.01$, ANOVA.

(J and K) JEDI-2P excitation and emission spectra under 1PM. For comparison, we used a variant of EGFP that is localized at the plasma membrane due to the C-terminal addition of a prenylation sequence (CAAX). JEDI-2P has slightly red-shifted excitation and emission peaks than EGFP-CAAX. JEDI-2P and EGFP-CAAX were expressed in HEK293-Kir2.1 cells which hold a polarized membrane potential of ∼ −77 mV. Spectra shown in the figure are averaged from n = 5 (JEDI-2P) or n = 4 (EGFP-CAAX) replicates, each of which was scanned with the same wavelength range and intervals. Spectra were normalized to their respective peaks before averaging replicates. The excitation and emission peaks of JEDI-2P were 501.4 ± 2.2 nm (95% CI) and 519.4 ± 2.0 nm (95% CI), respectively. The excitation and emission peaks of EGFP-CAAX were 488.5 ± 1.1 nm (95% CI) and 511 ± 0 nm (95% CI), respectively. (J) 1PM spectra of JEDI-2P. (K) 1PM spectra of JEDI-2P overlaid to those of EGFP-CAAX. All panels **** $p < 0.0001$; *** $p < 0.001$; ** $p < 0.01$; * $p < 0.05$; n.s. $p > 0.05$ for Tukey's HSD multiple comparison test. Error bars and shaded areas denote the 95% CI. All measurements were conducted at room temperature.

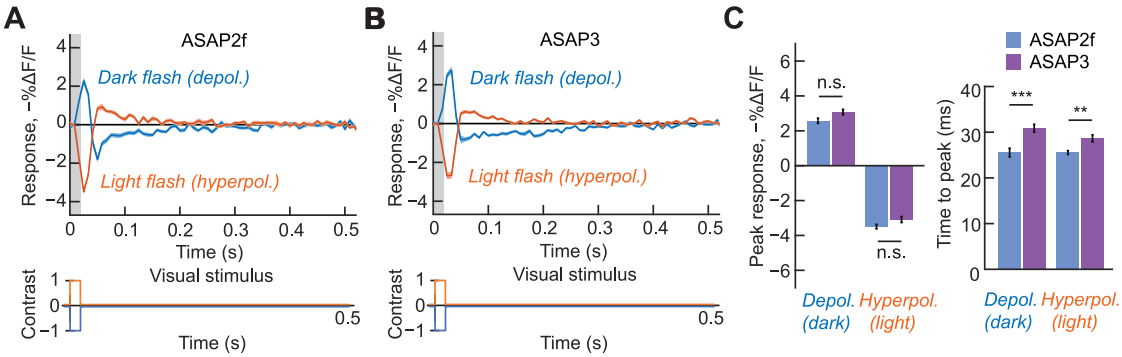

Figure S5. Comparison of ASAP2f and ASAP3 performance in *Drosophila*, related to Figure 4

(A and B) Mean stimulus-evoked L2 axonal voltage responses to 20-ms light or dark flashes from a mean gray interleave. Flashes are indicated with light gray shading near time = 0 and in the schematics below. Colored lines are the mean of each cell's average response. SEM were very small and displayed as shaded areas. Flies in this experiment also expressed the red calcium indicator jRGECO1b (Dana et al., 2016) in L2, in case we needed a secondary indicator to locate responding cells while imaging. n = 28 cells from 3 flies (ASAP2f) and 45 cells from 3 flies (ASAP3).

(C) Quantification of the responses shown in (A) and (B). ASAP2f and ASAP3 report impulse responses with similar response amplitudes (*left*), with ASAP3 displaying slower rise kinetics (*right*). Mean values are shown. Error bars are the SEM. *** p = 2.9E−4; ** p = 7.4E−3; n.s. p > 0.05 (t test with Bonferroni correction).

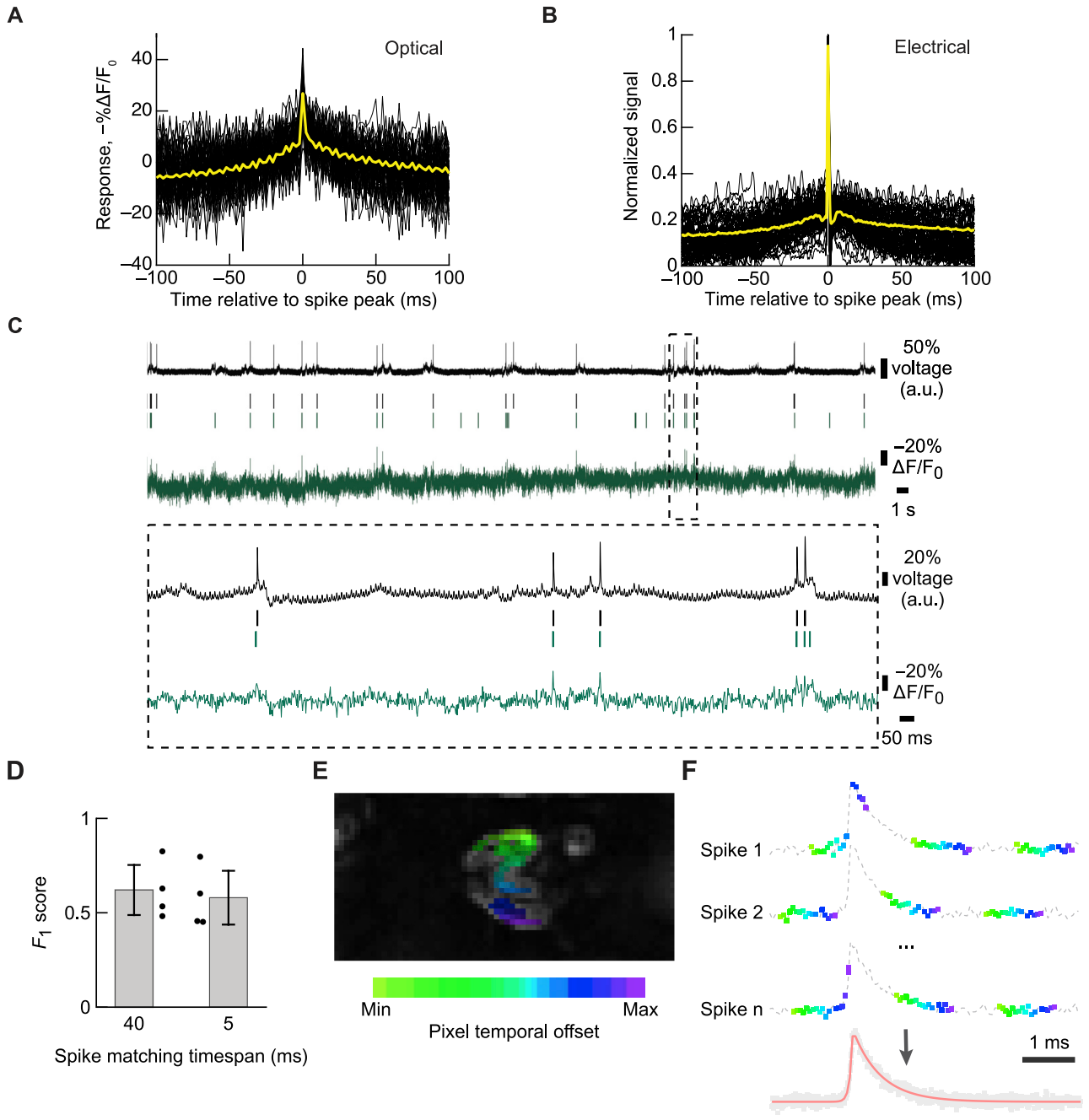

Figure S6. Evaluation of 2P resonant-scan voltage imaging with JEDI-2P, related to Figure 5

(A and B) Optical (A) and electrical (B) responses to spikes from the same representative neuron. Individual optical and electrical responses were aligned (black traces). Yellow lines indicate the mean. Optical imaging was conducted at 440 Hz.

(C) Simultaneous optical and loose-patch juxtacellular recordings in anesthetized animals. Vertical lines indicate spikes identified in the electrophysiological recording (black) or predicted from the optical trace using *VolPy* (green). The dashed box shows a zoomed-in section. The data were recorded from different cell than shown in Figure 5C.

(D) F_1 score quantifying the accuracy of spike inference between optical spikes identified with *VolPy* and electrical spikes. The time span (x axis) corresponds to the interval used for matching optical and electrical spikes (see method details). The F_1 sores for the 40- and 5-ms timespans were not significantly different; p value = 0.06, paired t test.

(E) Mean fluorescence signal from a cell imaged with resonant-scanning two-photon microscopy. Pixels with intensity higher than the 75th percentile were included in the analysis. The pixel temporal offset depicts the relative timing at which pixels are acquired in a single scan of the field of view.

(F) Schematic illustrating our strategy for generating an average optical waveform with high temporal resolution. The dashed lines depict the mean fluorescence response to an action potential by a fictitious cell. For each spike, we show a possible timing at which specific cell pixels were recorded. Each spike thus led to the sampling of a fraction of the full fluorescence signal to a spike. After acquiring the data for many spikes, intensity values in different time bins can be averaged, enabling the mean response to spikes to be estimated with high temporal precision.

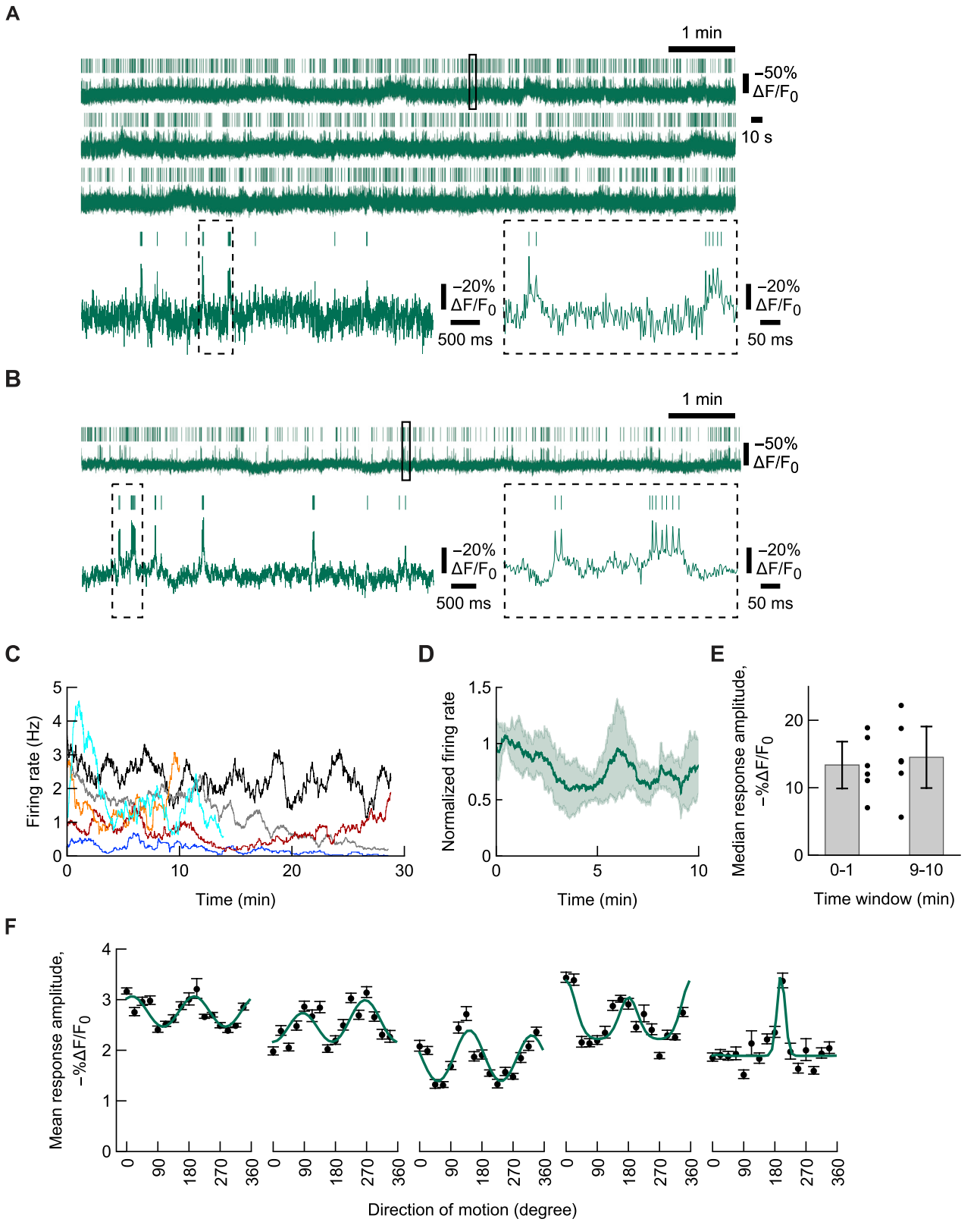

(legend on next page)

Figure S7. Imaging voltage dynamics in cortical layer 2/3 using JEDI-2P and resonant-scanning microscopy in awake behaving mice, related to Figure 5

(A and B) Additional examples of optical recordings in awake behaving mice. Vertical lines are *VolPy*-predicted spikes. The data were recorded from different cells than shown in Figure 5H. The durations of the recordings were 30 min (A), and 10 min (B). Cells were at a depth of 225 μm (A) and 170 μm (B) and are from the same animal.

(C) Detected firing rate. Each trace is from a different cell. n = 6 cells from 2 animals. The firing rate was computed by counting the rate of inferred spikes per second in a rolling window of 1 min and steps of 250 ms.

(D) Mean change in firing rate during optical recording. The traces from the n = 6 cells in (C) were normalized to their firing rate in the first minute of the recording. Shaded areas are the 95% CI. Recordings were from 10 to 30 min. The time range was set to the shortest recording.

(E) Median response amplitudes to *VolPy*-predicted spikes do not change over ~10 min of continuous recording. We compared responses over a 10-min window as the shortest recording was 10 min. Bars represent the means of medians. Error bars are the 95% CI. No significant difference was found between the two groups. p = 0.576 (paired t test). n = 6 cells from 2 animals.

(F) Direction tuning curves obtained from voltage imaging data for five additional layer 2/3 cells. The average response (black dots) is plotted as a function of the stimulus' direction of motion. For each direction of motion, fluorescence responses were averaged over the entire trace and thus include spikes, subthreshold potentials, and periods with no voltage changes. A von Mises function (Reimer et al., 2014) was fit and plotted (green line) together with the data. The error bars represent the 95% CI from n = 20 trials per cell. Plots are from 5 cells from the same animal.

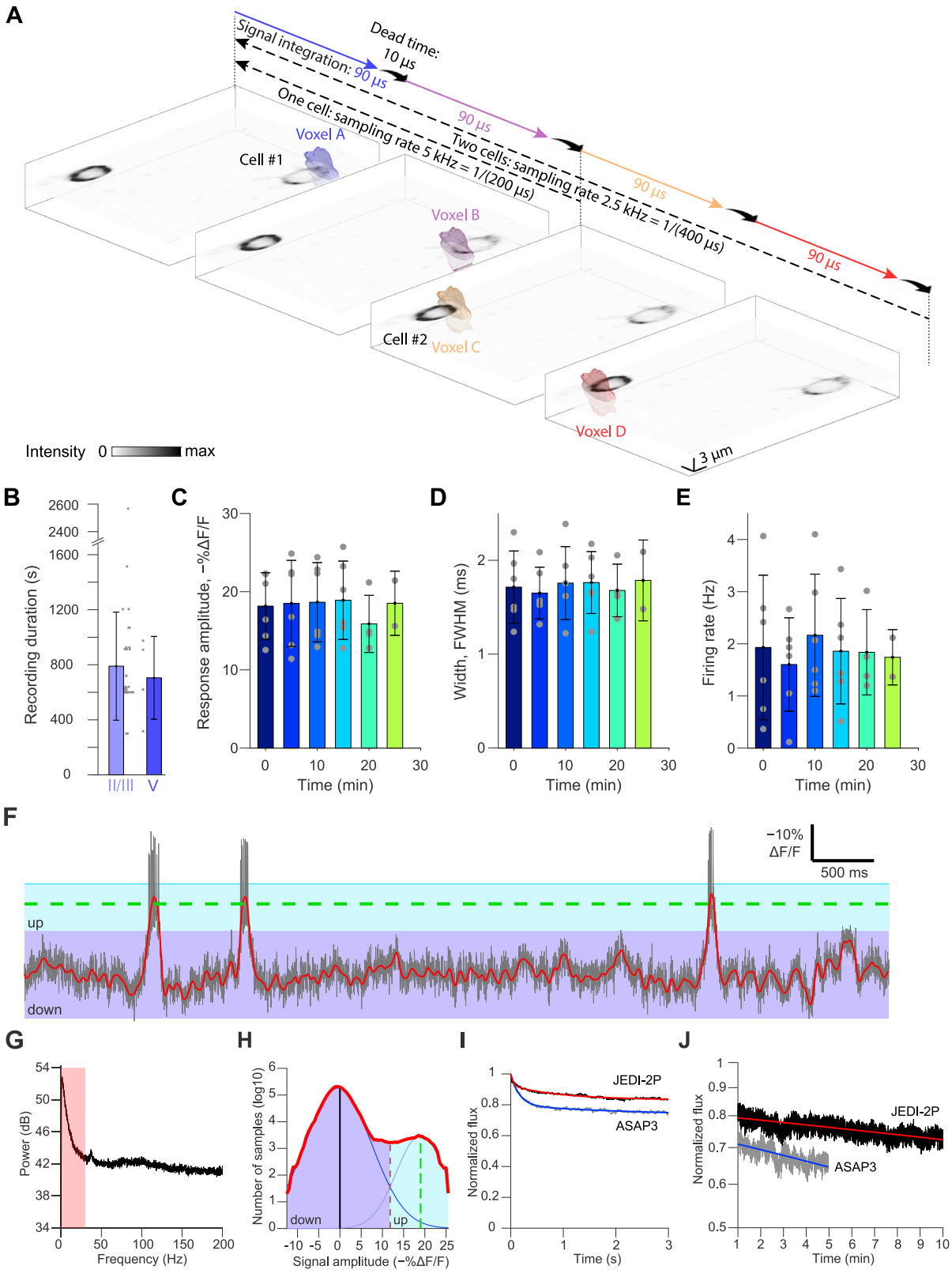

(legend on next page)

Figure S8. Acquisition and analysis of ULoVE optical recordings, related to Figures 6 and 7

(A) Temporal scheme of ULoVE recording. During single-cell ULoVE recording, the volumetric excitation pattern was applied to two locations of the cell, denoted as voxels A and B in schematic. Signal integration at each voxel was conducted for 90 μs, followed by 10 μs of dead time for moving the excitation pattern to the next voxel. The total dwell time per cell was 200 μs (5-kHz acquisition rate). For paired recordings, a similar excitation scheme was used, except a total of 4 voxels were used (2 per cell), resulting in a sampling rate of 2.5 kHz, half of that of single-cell recordings.

(B–E) Quantification of optical responses in ULoVE-based recordings of JEDI-2P-expressing neurons. (B) Durations of the optical recordings in layers 2/3 and 5. (C–E) Quantification of the spike response amplitude (C), spike width (full width at half maximum, FWHM) (D), and detected firing rate (E) over the time course of the recordings in layer 2/3. Data were pooled in 5-min bins (means ± SD). Gray circles are individual cells. None of the characteristics showed a significant correlation with time. p (linear regression t test) = 0.45 (C), 0.27 (D), and 0.13 (E). n = 6 cells at t = 0 min. Some recordings were shorter than 25 min, so the sample size decreases from the t = 0 to the t = 25-min bins. See method details for an explanation of the power levels used for ULoVE experiments.

(F–H) JEDI-2P reports UP- and DOWN-state modulations in awake mice. (F) Representative raw (gray) and filtered (red) traces illustrating membrane potential UP states (cyan area) and DOWN states (violet area) optically reported by JEDI-2P. (G) Power spectrum of the raw trace. The raw traces were low-pass filtered with a cutoff of 30 Hz (red area). The spectrum shown here used data from (F). (H) Distribution of the filtered trace values (red) from a representative layer 2/3 cell. The thick red line shows the double Gaussian fit used to delineate between the UP and DOWN states. As in (F), the data range corresponding to UP states is colored in cyan, while DOWN states are colored in violet. The solid black line corresponds to the peak of the DOWN-state distribution. The dashed green line corresponds to the peak of the UP-state distribution. The amplitude of the optical responses to UP states was quantified as the difference between the peak values of the UP and DOWN states.

(I and J) JEDI-2P is more photostable than ASAP3 during ULoVE recordings in layer 2/3 neurons. (I) Mean photobleaching traces for the initial 3 s of illumination. Bi-exponential fits are overlaid. Photon flux was normalized to 1 at t = 0. n = 34 (JEDI-2P) or 13 (ASAP3) neurons. The difference in the integral of the normalized flux is significant, with $p < 0.0001$ (bootstrap with 10,000 draws). (J) Mean photobleaching traces from t = 1 min are shown using a semi-logarithmic y axis. Linear regression lines are exponential fits. Normalization and samples sizes are as in (I). Recordings were stopped at 5 min for ASAP3, as spike detection was no longer reliable around this time point. The integral of normalized flux over time between t = 1 min and t = 5 min of JEDI-2P was increased by 14.6% compared with ASAP3. p = 0.0002 (bootstrap 10,000 draws). See method details and Table S1 for an explanation of the power levels used for ULoVE experiments.

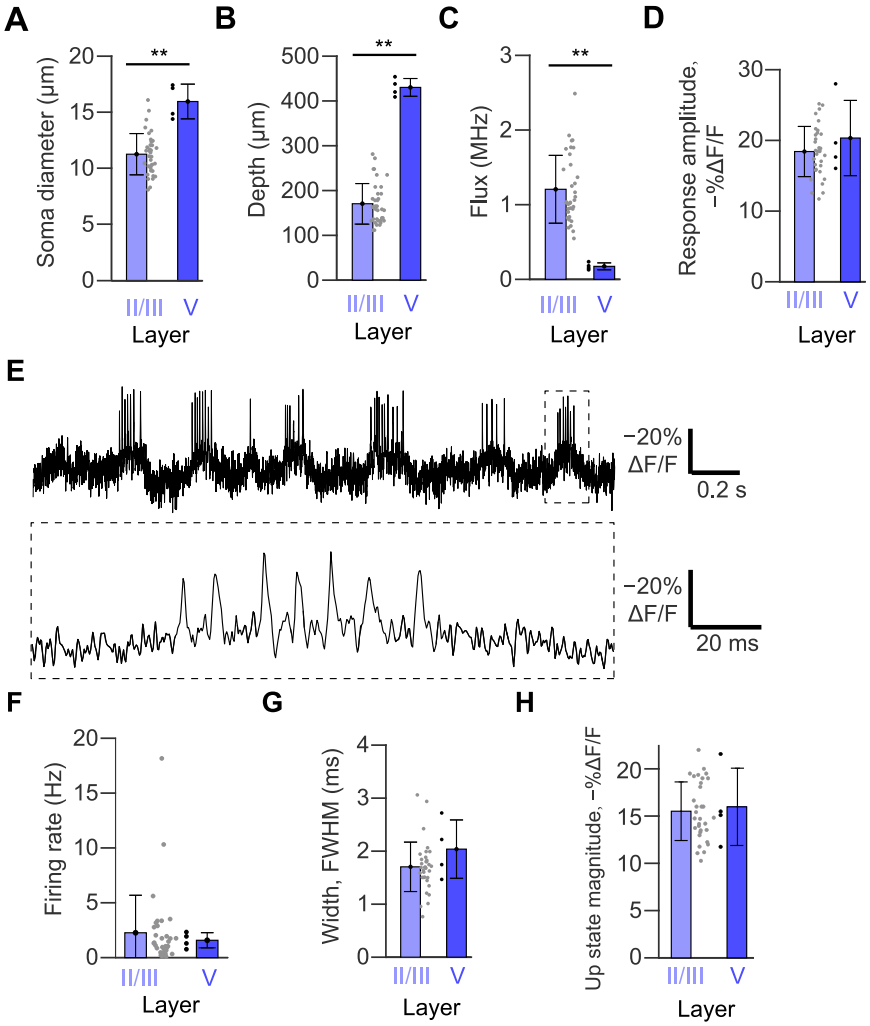

Figure S9. Comparison of cell size, recording conditions, and optical responses between ULoVE-based recordings of JEDI-2P-expressing neurons in layers 2/3 and 5, related to Figure 6

Layer 2/3: n = 36 neurons from 5 mice. Layer 5: n = 4 neurons from 2 mice. Error bars represent the SD. (A) Layer 5 cells had larger soma (16.2 ± 1.6 µm) compared with layer 2/3 cells (11.4 ± 1.9 µm). ** p = 0.0023, Mann-Whitney test. (B) Recording depth. ** p = 0.0013, Mann-Whitney test. (C) Photon flux of layer 5 neurons was 0.17 ± 0.04 MHz, compared with 1.2 ± 0.46 MHz for layer 2/3 cells. ** p = 0.0013, Mann-Whitney test. (D) Amplitude of the optical spikes. No significant differences were found. p = 0.60, Mann-Whitney test. (E) Traces from Figures 6H and 6I, but without the MLspike coloring. (F) Firing rate, calculated from optical spikes. No significant difference was found. p = 0.84, Mann-Whitney test. (G) Full width at half maximum (FWHM) of the optical spikes. No significant differences were found. p = 0.31, Mann-Whitney test. (H) The magnitude of UP states does not differ significantly between layer 2/3 and layer 5 cells (layer 2/3: mean ± SD: 15.5 ± 3.1 %$\Delta F/F_0$, n = 32 cells from 5 mice; layer 5: 16 ± 4.09 −%$\Delta F/F_0$, n = 4 cells from 2 mice). p = 0.82 (Mann-Whitney test).

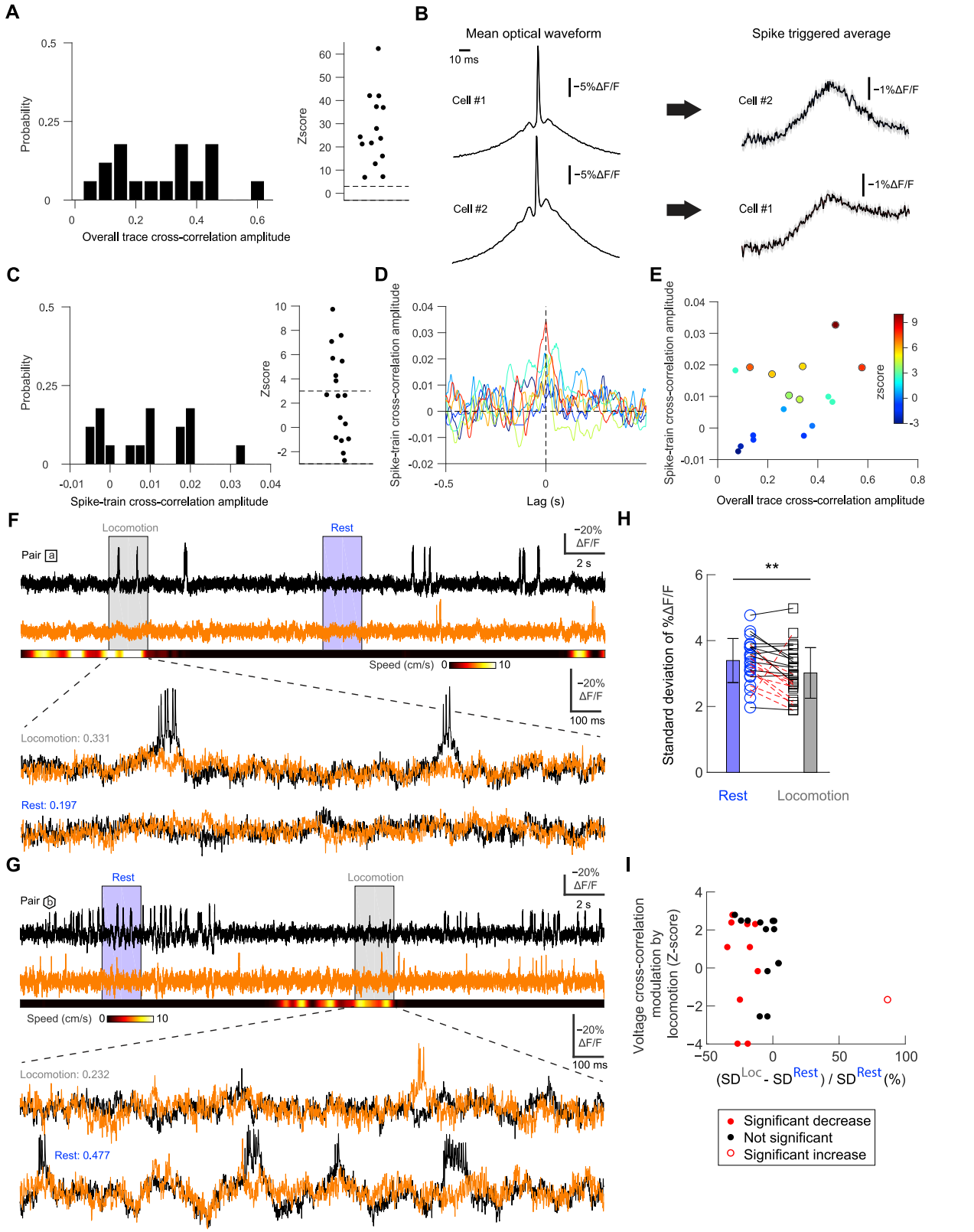

(legend on next page)

Figure S10. Subthreshold and spike correlations between neurons using ULoVE optical recording of JEDI-2P-expressing cells, related to Figure 7

(A) *Left*, Histogram of the peak cross-correlation values of the overall fluorescence trace. *Right*, significance (*Z* score) of the peak cross-correlation values of the n = 17 neuron pairs. The dashed line is the threshold value used for statistical significance ($Z = 3$ i.e., $\alpha = 0.01$).

(B) Mean spike-triggered average for a representative neuron pair. Shaded areas denote the SEM. The wide positive deflections of the spike-triggered voltage waveforms indicate voltage co-modulation of the two cells.

(C) Histogram of spike trains' peak cross-correlation values, using a spike bin width of 15 ms. *Right*, distribution of the significance (*Z* scores) of the cross-correlation values of the n = 17 neuron pairs. The dashed line is the threshold value used for statistical significance ($Z = 3$ i.e., $\alpha = 0.01$).

(D) Spike-train cross-correlation traces of the n = 7 pairs with significant cross-correlation values. Spike-train cross-correlations were smoothed with a 1-ms Gaussian kernel. The mean cross-correlation significance (*Z* score) was 6.2 ± 2.1 (range: 3.84–9.73). Cross-correlation amplitudes peaked at a mean lag of 8.2 ± 11.7 ms (range: −21.2–28.0 ms).

(E) We did not observe a significant correlation between the overall trace and spike-train cross-correlation amplitudes. Slope = 0.0031, Pearson coefficient (R) = 0.43, p = 0.084 (linear regression t test). The seven neuron pairs with significant spike-train cross-correlations are shown with a marker containing a black outline.

(F) Traces illustrating the ULoVE optical recordings for the two cells of the pair (A) illustrated in Figures 7A–7C and the top plot of Figure 7E. Zoomed traces are superimposed traces of the two cells during locomotion (*top*) and rest (*bottom*) epochs. Values on the left are the peak cross-correlation values, as also shown in Figure 7F.

(G) Same display as (F) but for the pair (B) shown in the bottom plot of Figure 7E.

(H) Distribution of the standard deviation of low-pass filtered traces during rest and locomotion periods. Bars show the mean and error bars are the SD. Locomotion decreased baseline variation, consistent with previous results (Reimer et al., 2014). ** p = 0.0014, Wilcoxon matched-pairs signed rank test. Measurements of individual cells are linked by a dashed red line to denote a significant change. Change is significant when the standard deviation computed during the locomotion periods (i.e., the trace excluding the rest epochs) falls into the 5% extrema of the distribution obtained from 10,000 standard deviations computed during rest periods of similar duration as the total locomotion period during the recording. n = 24 cells.

(I) Pairwise voltage cross-correlation modulation by locomotion as a function of the percentage of variation of baseline standard deviation during locomotion. The latter is obtained from the data in (H). Solid red dots indicate a significant decrease of variance from locomotion to rest periods; open red dots identify significant increases in the SD from locomotion to rest periods; black dots indicate cells where the variation in SD between locomotion and rest was not significant. We did not observe a significant correlation between the values plotted on the two axes (Pearson correlation coefficient, r = −0.190; p = 0.374 [linear regression t test]), consistent with independence between (i) the change in the voltage spread from rest to locomotion and (ii) cross-correlation modulation by locomotion. n = 24 cells.